Università di Napoli "Federico II"

Dipartimento di Chimica

Tesi di Dottorato in Scienze Chimiche

XIX Ciclo

Theoretical models of the interaction between organic molecules and semiconductor surfaces

Candidata

Maria Francesca Iozzi

Relatore:

    Prof. Guido Barone

Tutore:

    Prof. Maurizio Cossi

Acknowledgments

I wish to thank Prof. Maurizio Cossi for his supervision rich of ideas.

I thank Prof. Vincenzo Barone for his relevant contribution in the development of non-homogeneous PCM and its possible applications in the field of the structural biochemistry; Prof. David Cahen for the useful discussion about the organic/GaAs interface problem; Prof. Franco Deker and Prof. Roberto Zanoni for being the experimental counterpart in the exciting theoretical/experimental investigation of the ferrocenes on silicon.

I wish to thank Sindre and Svein for having been with me when I started; Atte for having me driven into the "awk" addiction.

I thank Andrea, Ercole e Ombretta for their unfailing support.

Contents

CHAPTER 1

Introduction

1.1 The Organic/Semiconductor Interfaces

Bulk and single-crystal semiconductors provide an appealing coupling of chemical, electrical and optical properties that can be exploited in the design of novel materials, electron devices and molecular sensors. Their surfaces are indeed characterized by a wealth of binding sites and platforms available for organic molecule adsorption from solutions: in most cases, the obtained organic/semiconductor interfaces are quite stable and characterized by a certain degree of order.

Over the past twenty years, many studies have focused on the ability of organic adsorbates in modifying the electrooptical properties of the substrate.
In many cases it has been found that the molecular layer affects the solid-state electronic behavior without the need of an actual charge transport across the organic moiety. Rather, the effect is often due to the static interactions between the molecule and the solid nuclear and electronic densities.
The coordinative unsaturation of the semiconductor surface atoms leads to electronic states, energetically located within the band gap. These states localized at the semiconductor surface produce a near-surface electric field in the solid, rep-

resented by the band bending and the surface potential. The adsorbates might alter the surface state distribution by shifting or introducing new states, causing the electric field perturbation and eventually measurable changes in the electrical and optical properties.

These is a considerable promise for the use of modified semiconductor substrates in many technological applications.

The diversity in the chemical, structural, electronic surface composition of the commercial semiconductors provides many opportunities for creating surfaces with tailored physicochemical properties and for tuning the electronic properties of the underlying bulk semiconductor material. Moreover the surface states pose a barrier to surface migration of the adsorbate species, leading to site specific adsorption process which are the basement for the *sensoring devices.*

Poly-functional molecules are commonly employed, with some groups designed to ensure a strong binding to the surface and other groups designed for the specific chemical and physical functions required. Due to the extremely rich choice of functional groups that can be combined on the molecular side, the contact potential difference of diodes assembled with modified materials can be finely tuned, allowing the engineering of *electronic devices* specifically tailored for their use.

In the *dye-sensitized solar cells*, an highly efficient light-to-current conversion is achieved by combining the sensitizer photoactivity and the high surface-to-bulk ratio of the nanostructured semiconductor substrate. In this case an actual charge transfer occurs at the organic/semiconductor interface whose mechanism is still unknown. Nevertheless strong evidences suggest that the transfer rate depends strongly on the adsorbate/substrate surface coupling, which is in turn influenced by the molecular moieties.

Finally, *ad hoc* modified surfaces are extensively used for surface degradation of specific pollutants and selective catalytic chemistry.

An efficient design of such devices requires a clear understanding of the microscopic structure and interactions between the molecules and the solid substrate. A prerequisite for an advance in the modified surface engineering has been the development of highly sophisticated and powerful experimental techniques, in particular spectroscopic methods for investigation of the adsorbate/substrate interface at molecular scale. Examples are high-resolution solid state magic-angle NMR spectroscopy, UPS, XPS and scanning tunneling microscopy (STM). Often, however, a clear picture of the interface at atomic level is hardly obtained, due to the roughness of the modifies surfaces. A full interpretation of the STM evidences requires us to be able to generate a plausible model for the modified surface, and

solve its electronic structure in order to obtain a picture to be compared with the experimental one.

In the interface investigations, many challenging questions need to be solved: which atomic structure produces a given effect? what is the geometry of the site of interest and what properties does it have? what is the nature of the substrate/adsorbate bonding? The theoretical modeling can provide useful insights in clarifying these aspects: this contribution is even more crucial if interfaced with the experimental investigation.

In the last decades, the quantum chemical methods have been successfully applied in the field of molecular chemistry and solid state physics. Thanks to the steep increase of the computational resources and efficient implementations, reliable energies were computed on systems of increasing dimension and complexity. Computational techniques developed for describing molecules and solid materials are conceptually similar but substantially different in the adopted formalism: the solid state physics approaches make use of plane wave functions to describe delocalized band structures and periodic properties in crystals. Methods aiming to describe discrete energies and localized bonding systems in molecular structures are based instead on the use of Gaussian functions. Neither the molecular approach nor the physics approach can be applied straightforward for describing the energetic coupling between molecular states and surface states accomplished at the adsorbate/solid-substrate interface: from this point of view the interface modeling represents a computational challenge.

One way to overcome these intrinsic difficulties is to adopt finite models, such as real or hypothetical molecules adsorbed on clusters of atoms, to be treated by the same ab initio methods applied for molecules. This means to confine the quantum description to those atoms and interactions significative for the property under study, treating the environment by suitably chosen boundary conditions. Hence this cluster approach is suited for local phenomena description, even though it can also reproduces structure and bonding in crystals. The goal of the present work is to explore the potentiality of the cluster approaches and molecular methods in reliably reproducing the local interface effects and their influence in the bulk properties.

1.2 Organization of this work

We start with a short survey of standard molecular methods (Section 2.1): strength and weakness of ab-initio and semi-empirical methods are considered, along with the possibility of integrate such approaches into the well known ONIOM procedure. Section 2.2 reports a survey of the most used strategies for selecting a good cluster model and minimizing boundary effects: besides the standard embedding strategies, we propose a new Polarizable Continuum Model formalism, referred to as Mixed-ϵ PCM and a novel mixed DFT/semiempirical approach.

The presented methods, cluster strategies and embedding techniques are tested in Chapter 3. In particular, we focus on the ability of the selected method/model in providing (*i*) reliable binding energies of TiO_2 nanoclusters with increasing size (Section 3.1); (*ii*) reliable reconstruction patterns of the GaAs(001) surface (Section 3.2).

The following three Chapters report the results of the adsorption studies of organic molecules on three different semiconductor substrates: Gallium Arsenide, Titanium Oxide and protonated Silicon.
Chapter 4 concerns adsorptions on Gallium Arsenide surface. The GaAs is one of the most used semiconductor compound in technological applications: high-efficiency solar cells are obtained by using GaAs, thanks to its band gap (1.43 eV) nearly ideal for single junction solar cells. GaAs solar cells have become integral component of light-emitting diodes, lasers, and other optoelectronic devices. One of the greatest advantages of gallium arsenide is the wide range of design options possible: a cell with a GaAs base can have several layers of slightly different compositions that allow a precise control of the cell performances, pushing the efficency closer and closer to theoretical levels.
In recent years, the ability of a class of organic oxygen-donor ligands to modify the electronic properties of the GaAs has been proved, opening the promising field of tailored surface engineering in nanoelectronic. In Section 4.1, the adsorption mode of benzoic acid on GaAs(001) is investigated; furthermore (Section 4.2) the influence of a class of Tartaric acid derivatives on the GaAs electronic properties is studied, correlating the macroscopic observables with microscopic interface properties.

In Chapter 5 organic molecules were adsorbed onto TiO_2. Titanium dioxide is

a widely used material thanks to its proved photocatalytic activity, i.e. its ability to create an electron hole pair upon exposure to ultraviolet radiation. The resulting free radicals are very efficient oxidizers of organic matter. The titania is used as a photocatalyst in a large area of activity: water and air purification, anti-bacterial and anti-soiling. In this context, the investigation of the adsorption binding structure is the very first step towards the understanding of those peculiar interface phenomena leading to the final organic compounds decomposition. In Section 5.1 the adsorption mode of acetic acid is investigated by comparing the measured IR spectra with the computed vibrational frequencies of a number of postulated adduct structures. The adsorption mode of a large Ruthenium-based dye on nanostructured TiO_2 is also investigated in Section 5.2: here a mechanism of charge injection process, the fundamental photophysical process in the dye-sensitized TiO_2 solar cell, is postulated on the basis of the computed interface electronic properties.

The organic derivatization of the silicon surface has gained attention for the potential application in nanoelectronics. Basic issues regarding the functionalized silicon surfaces are still under debated, notably the role played by the presence of covalent bonds established between organic adsorbate and substrate, in determining the hybrid chemical behavior. Even the hybrid structures and the adsorption mechanisms are in most cases unknown.
The adsorption of a number of Ferrocene derivatives on H_x-Si(100) ($x = 1, 2$) is systematically studied, in Chapter 6: by comparing the measured redox potentials with those computed on some postulated hybrid structures we are able to identify the most likely adducts and hypothesize the adsorption mechanism leading to them.

For each subject, a short survey of the state of art is provided, drawing the attention on the properties under study and referring for more details to the suggested literature, reported at the end of this work.

CHAPTER 2

Methods

2.1 Quantum Chemical Methods

In the past fifty years, many methods have been developed and successfully applied to solve at the quantum level the electronic and structural properties of molecular systems and periodic crystals.

In the solid state physics, a better description of the crystal structure, and a sensible reduction of the computational costs, can be achieved by exploiting the periodicity of the crystal lattice. Differently, methods suitable for molecular systems are based on the use of electronic functions localized at the atomic positions. Difficulties arise in dealing with molecules adsorbed on solid matter, i.e. adsorbate/substrate interfaces. In this case the use of periodic techniques will provide a good representation of the solid properties at the expense of the molecular description. The opposite occurs when one uses a local approach.

Since the present work is devoted on the study of the microscopic properties of the organic/semiconductor interfaces, the use of quantum molecular-based techniques will be extended to the interface models.

Ab initio methods[1] Almost all the computational procedures to solve the many-electrons equation rely on the *Hartree-Fock approximation* (HF), which assumes that the motion of an electron within the molecular system depends only on the average potential of all the electrons: for this reason, it is known as independent particle model. Since the motion of the electrons is indeed "correlated", the difference between the real energy and the one obtained within the Hartree-Fock approximation is known as *correlation energy*. Even if this energy contribution is a small term in the total energy, it might be relevant in processes involving relatively small energy changes, i.e. surface reconstruction or Fermi surface modification.

For this reason, the use of HF methods in adsorption studies is not recommended.

More recently, the *Density Functional Theory* (DFT) has become a standard tool for solving quantum chemical problems in terms of electron density functions rather than single-electron functions. Unlike the Hartree-Fock approximation, the DFT energy is in principle exact, provided that the density functional describing the electron-correlation energy (along with the electron-electron exchange energy) is known: since this is not the case, one has to seek for an approximate form of the exchange-correlation functional.

A wealth of different functionals has been designed, each differing from the others by some empirical terms used to correct their common original form (known as "local density approximation"). In some case, functionals are written as the sum of an exchange functional and a correlation functional: the first one can be corrected by the *Hartree-Fock exchange contribution* leading to the so called *hybrid functional*. Among the standard hybrid functionals, it worths to mention the B3LYP[2] and the PBE1PBE[3] functionals: in the former the HF-exchange contributes by a 0.2 factor to the total exchange energy, while an higher HF contribution (0.5) is present in the latter.

DFT methods have proved to be surprisingly accurate for the structural properties of strongly bonded systems; moreover weakly bonded systems, transition states and energy changes in process involving open structures have been satisfactory reproduced with the aid of hybrid-DFT approaches.

Many phenomena in the solid state physics are time-dependent: in a dye sensitized solar cell, the dye excitation and eventually the charge injection into the semiconductor band structure are processes defined on the time scale. The introduction of the time effect is therefore mandatory.

Due to the large dimension of the computational problem, the solution of the time-dependent Schrodinger equation is hardly performed, and one has to seek for approximated methods.

Among the methods based on the perturbation theory, we will use the *time-dependent*-DFT[4,5], in which the excitations are computed as poles of a *hole-particle/particle-hole* Density Matrix built on the Kahn-Sham orbitals space. This procedure provides reliable results with reasonably low computational costs. Furthermore the computational burden can be reduced by a selection of an active sub-space of molecular orbitals[6].

In this work, all the DFT and TD-DFT calculations were performed with the Gaussian03 package[7].

Basis Set   The choice of suitable basis set is a crucial step in the computational treatment of complex systems. Aiming to describe local phenomena occurring at the adsorbate/substrate interface, we will mostly use ab initio non-periodic methods with atomic centered Gaussian Basis functions. A survey of basis set available and specific comments on their selection can be found on reviews of Dunning and Hay[8], Ahlrichs and Taylor[9], Huzinaga[10] and Davidson and Feller [11].

In the computational study of surfaces and interfaces, great advantage can be obtained by using the *effective core potential*(ECP), often refer to as "pseudopotential" or "model potential". These techniques are indeed successfully applied for element of higher periods, and consist in replacing the core electron, assumed as inert, with suitable potential[11,12]. Some ECP's also include to a certain extent the effect of the relativistic distortions for the very fast inner electrons, resulting even more accurate than the non-relativistic all electron basis sets. As long as such ECP potentials do not contain adjustable parameters and are derived in a non empirical way, the methods are still "ab initio".

Semi-empirical   The ab initio treatment of large systems is not always feasible. In the *semi-empirical methods*, the computational costs are drastically reduced by using a minimal set of basis orbitals: the validity of the obtained methods relies on the fitting of some experimental data to compensate the errors which are thereby introduced. This guarantees reliable results on molecular compounds containing those elements for which the method has been parameterized, but caution must be used when using it outside this domain. In particular, surface problems can involve unusual coordination or bonds between atoms which normally do not react. This is not to say that semi-empirical methods should not be used for surface problems, but a careful checking with reliable ab initio calculations and

experimental results is needed in this case.

There are many different semi-empirical methods, namely CNDO[13], INDO[14], MINDO[15], SINDO1[16]. In the present work, semiempirical calculations have been performed with the MSINDO method (MSINDO package, Version 2.6.3 by K. Jug, T. Bredow and G. Geudtner),[17,18] based on the previous SINDO1 approach with significant improvements in the basis sets and parameterization. MSINDO has been recently extended to third row elements with an efficient parameterization[19,20] that has provided very satisfying results for structures, relative energies and dipole moments, and it is probably the best compromise presently available for the study of very large semiconductor clusters.

The Integrated Approach In order to reduce the computational burden without renouncing to the accurate results, the so called hybrid methods have been developed, the most common being normally refers to as ONIOM scheme [21−27]. The basic idea is the partitioning of the system into two or more parts or layers, where the interesting or "difficult" part is treated at high level of theory (the *inner layer* in Figure 2.1) and the rest (the *outer layer*) is described by a computationally less demanding method.

Parting the systems into two regions inevitably creates unphysical boundaries. Expecially in the case of covalent bonding systems, the dangling bonds must be saturated in order to avoid spurious effect. The most common choice is to saturate the boundary atoms (**A** in Figure 2.1) of the high level part with the so called *link atoms* (**H**). These atoms mimic the presence of the close neighboring (**B**) atoms in the outer region. In terms of internal coordinates, the angle and dihedral angles referred to the link atom are the same as those referring to the close neighboring atom in the whole system. The link atom is settled at a suitable distance, which might differ from the original bond distance between the border atom and its neighbor. Even thought the link atoms are normally hydrogen, they can be chosen in order to reproduce better the bonding feature between the high level atom and its neighbor[28−30].

Let consider a molecular system ("real" system) and suppose to be interested in one part, which will be referred to as "model" system. Once the type and position of link atoms have been defined, the energy of the system treated at ONIOM level (E_{ONIOM}), is calculated according to the following:

$$E_{ONIOM} = E_{model}^{high} + E_{real}^{low} - E_{model}^{low} \qquad (2.1)$$

This scheme can be easily extended to more complex partitioning. Moreover, its validity holds also for computing properties depending on first and second energy derivatives, such as gradient and Hessian matrix, respectively. Therefore, if O is an observable (energy, gradient for optimizations, harmonic frequencies), its

value calculated within the ONIOM scheme is:

$$O_{ONIOM} = O_{model}^{high} + O_{real}^{low} - O_{model}^{low}. \tag{2.2}$$

Figure 2.1: Definition of inner region, outer region and link atoms in the ONIOM scheme. (Rearrangement of Fig. 2 in Ref. [26]).
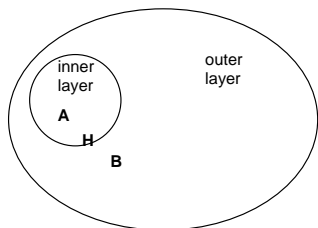
Model System = inner layer + link atoms
Real System = inner layer + outer layer

In the present work we have implemented an integrated approach which allows to treat the interesting part of the interface at DFT level, and the rest at MSINDO level. This hybrid method will be referred to as DFT:MSINDO.

2.2   Modeling Strategies

The question of what model to use for a surface calculation is not a straight-forward one. This is because many aspects must be considered, related to the intrinsic complexity of the systems themselves. Moreover, quite often the computational expense limits the modeling, and one has to seek for the best compromise between accuracy and computational demands.

Different approaches have to be adopted in dealing with either metals, ionic crystals or covalent materials: Sauer[31] gave a comprehensive account of methods and materials, discriminating between physical and chemical methods. An interesting overview was given by Jug *et al.*[32], focusing on the suitable approaches for surface and adsorption modeling. More recently Deak[33] discussed the choice of models for solids in a qualitative way.

In the following Sections we provide a short qualitative overview of the methods, mainly focusing on the chemical approaches applied on ionic crystals and covalent materials. The aim is to prepare the description of the approaches designed specifically for the adsorption studies presented in the following Chapters.
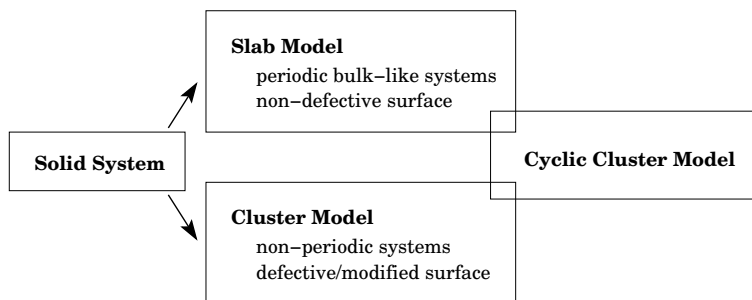
Figure 2.2: The slab and cluster approaches and their range of applicability.

2.2.1 Slab vs. Cluster

Historically, the two most popular choices to model a surface have been the *slab* and the *cluster* models (see Figures 2.2 and 2.4).

In slab calculations the model system, which is a stoichiometric portion of the solid cut out along the mainly exposed lattice planes, is extended with a two-dimensional periodicity, parallel to the surface. These models, mostly used in the solid state physics, are normally treated with periodic quantum chemical approaches[34−36]. The periodicity of the crystal is therefore fully described with the aid of plane-wave functions, which are delocalized and do not refer to a particular site in the lattice. Actually, a number of implementations based on this approach are standardly used for surface studies.
The formalism combining the more local atomic functions with the periodic slab approach was developed by Pisani and coworkers[37] and implemented in a corresponding program.

The cluster models can be seen as the early stage products of crystal growth process from atoms. These are physical entities in their own right, but can also be models for solids, provided that a certain size has been reached. The cluster geometries are mostly treated with the aid of quantum molecular methods and atomic orbitals centered on atoms. The potential pitfall in the use of the cluster model is in the treatment of the cluster boundaries and non-surface edges.
It is worth to mention the more recent *cyclic cluster* model[38−42]. This cluster can be regarded as a supercell, obtained by a finite number of translations of the chosen unit cell. The calculation exploits the translational symmetry by

applying a suitable supercell translational vector. Conceptually, this corresponds to replace a "planar cluster" with a "spheric arrangement", as shown in Figure 2.3.
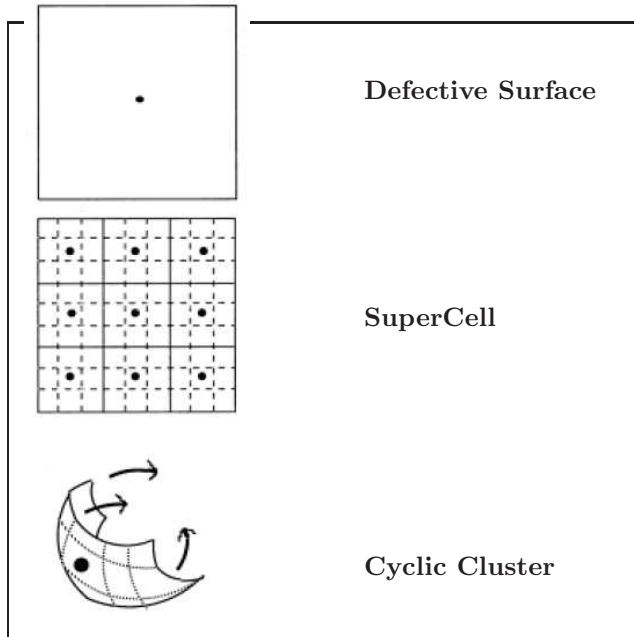
Figure 2.3: The cyclic cluster strategy. Rearrangement of Figure 1 in Ref. [33]

Periodic models are preferable over finite clusters for the description of perfect crystals, since they explicitly take into account the translational periodicity. Moreover there are no spurious electronic states due to the presence of boundary atoms. On the other hand, defects on the surface will be better described in terms of atomic orbitals and cluster models; moreover the local character of this approach allows the best description of the chemical bonding.

Broadly speaking, the cluster approximation is more suitable for a *ionic insulator*, where there is no breaking of bonds at the cluster geometry, whereas the slab approach is more suitable for *metals*, in which the geometrical and electronic influence of the surface decays very rapidly into the bulk. In a *covalent semiconductor* there are both strong bonds to be broken at the cluster boundaries, and relatively long range relaxations and electronic effects arising from the surface, so there are potential pitfalls with either approach.
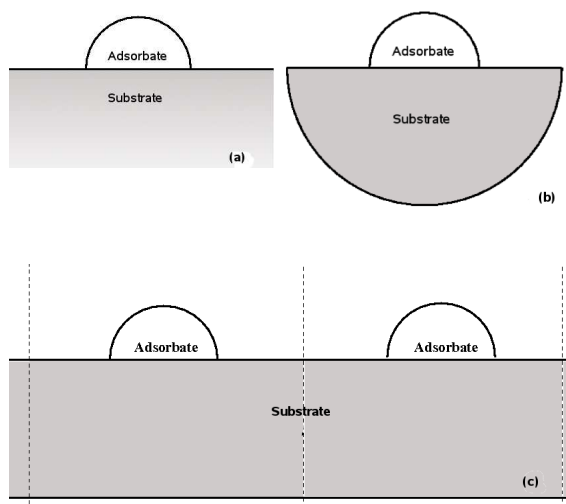
Figure 2.4: Possible adduct approaches for modeling modified surfaces: (a) sketch of the modified surface, (b) adduct cluster model, (c) two-dimensional adduct slab model.

More complex systems, such as modified surfaces and adsorbate/substrate interfaces can be treated both with cluster and slab approaches, by choosing the suitable *adduct structures* (see Figure 2.4). It is worth noticing however that the treatment of such systems will profit from the use of local rather than periodic methods, the latter being affected by fictitious, often unphysical, interactions between slab adducts.

In the present work, the ability of the cluster approach to describe organic/semiconductor bonding is exploited, being our interest focused on the local structure and the electronic properties of the interface itself.

2.2.2 Free Cluster

A cluster geometry is easily obtained by cutting out a small portion of crystal bulk-like structure. The cutting out procedure unavoidable generates spurious

effects related to the limited size of the cluster and the presence of boundary. To avoid these effects one can saturate the dangling bonds, using either hydrogen atoms or pseudo-atoms (*Saturated Cluster* in Figure 2.5). Otherwise the cluster can be set in an external field simulating the presence of the bulk (*Embedded Cluster* in Figure 2.5). These two strategies are discussed in more details in the next Sections.

In the *Free Cluster* approach (see Figure 2.5) neither the saturators nor the embedding field are used. In this case, the electronic structure and properties of the cluster critically depend on its shape, size and stoichiometric. Nevertheless if the cluster is properly chosen and its size-dependent properties have been investigated, it can be a good model for surface simulation.

Of course the reliability of a certain sized/shaped cluster as a surface model depends on the chemical nature of the solid to be modeled. Therefore there is not an unique modeling strategy for designing a cluster. In particular, three aspects need to be considered to minimized the artefacts of the model: the stoichiometry, the net charge and the average coordination number. According to the coordination principle, the coordination number of each atom in the cluster should be as high as to support its formal oxidation state in the real crystal. As an example, in the case of TiO_2 cluster, each Ti and O atoms should be at least four and two-folded, respectively. For some substrates, the three principles can not be simultaneously satisfied: in these cases the priority assigned to each request depends on the specific property one aims to study.

In Figure 2.6 we propose an hierarchical strategy for cluster modeling. The cluster geometry is initially cut out from the crystal structure in order to fulfill the coordination principle; afterward, the requests of neutrality and of the stoichiometry are satisfied.

In most cases, the cluster obtained by applying the coordination principle is charged: such models are not adequate for chemisorption studies, since the unphysical charge artificially shifts the frontier orbital energies of the cluster and creates fictitious static interactions with the adsorbate. In this case, to satisfy simultaneously the coordination principle and the electroneutrality, suitable saturators or a point charge embedding pattern must be used: in the former case the stoichiometric request automatically fails.

Whenever the obtained geometry satisfies both the coordination principle and the electroneutrality, the application of the stoichiometric principle is strongly recommended. The increase of average number of dangling bonds per atom and the introduction of a fictitious net dipole are the typical drawbacks of the stoi-
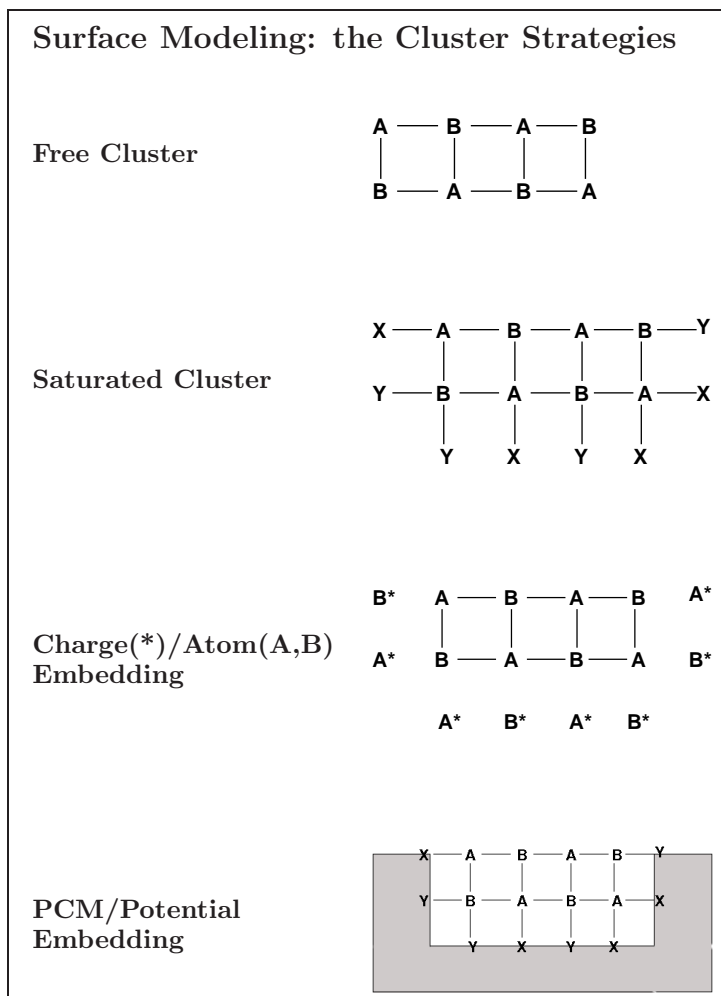
Figure 2.5: The different cluster strategies for surface modeling.
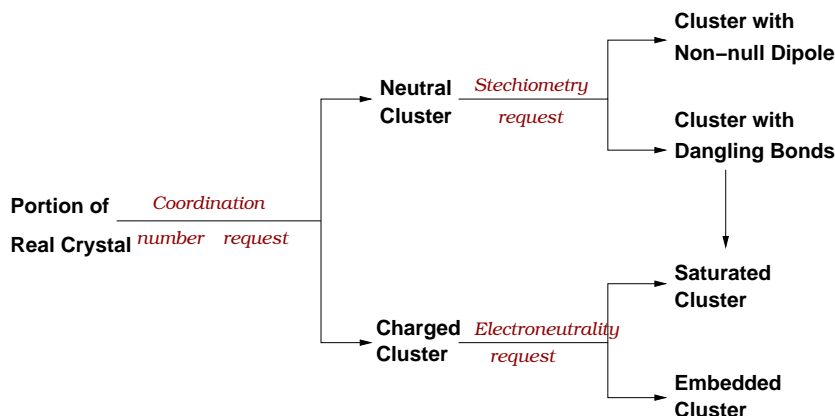
Figure 2.6: Proposed strategy for cluster modeling

chiometric request, whose effect should be at least minimized.

2.2.3   Saturated Cluster

The free cluster has borders (surfaces, edges and corners) that might not be present in the ideal crystal: the increased surface-to-bulk ratio corresponds to an extra amount of dangling bonds which produces fictitious effects in the model. The most used strategy to reduce the surface and eventually the average number of dangling bonds is to introduce saturators. This approach works best in systems characterized by localized bonding, i.e. covalent materials.
A commonly used saturator is the hydrogen atom, which was found to be good for capping atoms with similar electronegativity (i.e. hydrogen atoms saturating carbon atoms[43]). For those atoms displaying a significant shift in the electronegativity with respect to hydrogen atom, the use of a "modified core potential" centered on the hydrogen position is recommended. Such modified saturators are referred to as pseudo-hydrogens[44]. In the case of charged clusters (see Figure 2.5 and Figure 2.6) the pseudo-atoms might support an extra charge in order to satisfy the electron-counting rule and make the saturated cluster electroneutral.

2.2.4   Embedding Strategies

Point Charges, Potentials and Integrated Approachs.   In recent years, a wealth of embedding techniques has been developed in order to improve the performance of the free cluster in modeling surface properties. These techniques were mostly applied with metal and ionic crystals, for which the saturating strategies do not work well.

 The basic idea in the embedding strategies consists in dividing the system under
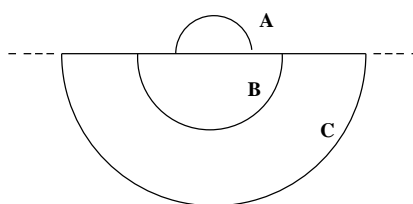
Figure 2.7: System consisting of Adsorbate (**A**), a surface cluster (**B**) and an embedding cluster (**C**).

study into regions to be treated with decreasing accuracy. For modified surface study, highly accurate description of the adsorbate and a surface cluster is required (i.e. [**A** + **B**] in Figure 2.7), while shells of embedding solid ([**C** + **D** + ...] in Figure 2.7) are treated with a hierarchical sequel of less accurate approaches. In the most simplified approach, normally used for ionic clusters, the embedding solid is modeled by a series of *point charges* [45,46] (see "Charge embedding" in Figure 2.5). These charges were taken as integer or fractional charges, reflecting the net charges of the atoms of the cluster obtained from a quantum chemical calculation. The point charges can be settle in order to reproduce the Madelung potential at the chemisorption site. [47] A more realistic embedding procedure makes use of *pseudoatoms* [48]. Here, the point charges surrounding the free cluster were replaced by atoms with the same basis set and approximation as the corresponding cluster atoms. The only difference is that the basis functions of the pseudoatoms do not enter the Fock matrix explicitly; hence they do not extend the matrix dimension.

Otherwise, one can use a *model potential* [49,50] for embedding purpose (see "Potential embedding" in Figure 2.5). In this case both the embedded ([**A** + **B**]) and embedding regions ([**C**]) are modeled with a cluster geometry. In the calculation only the electrons from the central cluster were explicitly treated, whereas the embedding surround enters the Hamiltonian of the central cluster by a local Coulomb potentials and a non-local exchange potentials.

A widely used class of techniques is based on treating the central and the embedding clusters with differently accurate atomistic approaches, being the different methods integrated with the ONIOM scheme (see Section 2.1). In the most common scheme the central part is treated by quantum chemical methods and the embedding region is at classical level. This mixed method is commonly referred to as QM/MM approach. To improve the description, the whole cluster (i.e. $[\mathbf{A} + \mathbf{B} + \mathbf{C}]$) might be in turn embedded into a region of atomic point charges [51].

In the present work we use of the DFT:MSINDO approach, which represents a further improvement of the description, since it consists of a combination of two quantum methodologies. Moreover the MSINDO semiempirical method was parameterized for a number of solid materials.

When one uses a mixed method as embedding, a special attention should be taken in choosing the type and the number of linking atoms, since they play in the present context a double role: in primis, they ensure the proper treatment of the boundary between the central cluster and the embedding cluster; secondly they can be adjusted in order to further correct the limited size effect, in the QM solution of the central cluster electronic structure.

Mixed-ϵ PCM In the present work we have developed and implemented a novel embedding strategy, based on the use of the well known Polarizable Continuum Model formalism [52,53]. The starting idea consists again in excising the region of interest (namely the cluster adduct $[\mathbf{A} + \mathbf{B}]$) out from the real modified surface and introducing the environment effect as a perturbation to the Hamiltonian of the adduct cluster. The perturbing potential is due to the presence of the environmental media which is fully described by its macroscopic dielectric constant, ϵ. The present method differs from the other PCM methods since it allows the use of a non-constant macroscopic dielectric function to account for large discontinuities in the environment of the cluster model.

In all the PCM variants the solute or the region of interest is represented in atomic details and embedded in a cavity formed by the envelope of spheres centered on the solute atoms. The United-Atom Topological Model(UA0)[54] can be used to assign the atomic radii; the procedures to form the cavity are described in detail elsewhere.[55,56] Here we only recall that the cavity surface is finely subdivided in small tiles (*tesserae*), and that the solvent reaction field is described in terms of apparent point charges appearing in tesserae and self-consistently adjusted with the solute electron density (ρ).[57]

The solute-solvent interaction energy is

$$E_{int} = \mathbf{V}^\dagger \mathbf{q} = \sum_i^{tesserae} V_i q_i \qquad (2.3)$$

where the column vectors $\mathbf{V}$ and $\mathbf{q}$ collect the solute (nuclear+electronic) electrostatic potential and the solvation charges in the surface tesserae, respectively. If $E^0 = E[\rho^0] + V_{NN}$ is the solute energy in vacuo, the quantity that is variationally minimized in the presence of the solvent is the free energy[57]

$$G = E[\rho] + V_{NN} + \frac{1}{2} E_{int} = E[\rho] + V_{NN} + \frac{1}{2} \mathbf{V}^\dagger \mathbf{q} \qquad (2.4)$$

where V_{NN} is the solute nuclear repulsion energy, ρ^0 is the solute electron density for the isolated molecule, and ρ is the corresponding density perturbed by the solvent.

The solvation charges are computed as $\mathbf{q} = \mathbf{Q}\mathbf{V}$, where $\mathbf{Q}$ is a geometric matrix, depending on the position and size of the surface tesserae. The PCM operator, defined by differentiating the quantity $\frac{1}{2}\mathbf{V}^\dagger \mathbf{Q}\mathbf{V}$ with respect to the electronic density is used to correct the Fock or Kohn-Sham operator in the SCF procedure, as well as in the calculation of electronic properties. It is worth noting that since the solvation charges depend on the solute potential, and hence on its electronic density, the PCM term in the Hamiltonian is analogous to the Coulomb operator (i.e. a two-electron term, bilinear in the electronic density, that can be put in a pseudo-one-electron form during the SCF procedure).

The core of the model is the definition of the $\mathbf{Q}$ matrix. For isotropic solvents it is defined as[57]

$$\mathbf{Q} = \mathbf{T}^{-1}\mathbf{R}$$

$$\mathbf{T} = \frac{\epsilon+1}{\epsilon-1}\mathbf{S} - \frac{1}{2\pi}\mathbf{D}\mathbf{A}\mathbf{S} \qquad (2.5)$$

$$\mathbf{R} = -\mathbf{I} + \frac{1}{2\pi}\mathbf{D}\mathbf{A} \qquad (2.6)$$

where ϵ is the dielectric constant, $\mathbf{I}$ is the unit matrix, $\mathbf{A}$ is a diagonal matrix collecting the area of tesserae, and the matrices $\mathbf{S}$ and $\mathbf{D}$ are related to the

electrostatic potential and to the electric field generated by the solvation charges, respectively.

The treatment can be extended to heterogeneous environments by means of a position-dependent dielectric permittivity, i.e. substituting the dielectric constant by a function $\epsilon(\mathbf{r})$.[58,59] Such an approach requires the knowledge of the electrostatic Green function associated to the particular environment under study: in general this function is not easily defined for non homogeneous systems, and must be computed numerically with suitable molecular dynamics. The complexity of the Green function procedure practically prevents its extensive application to large systems like proteins and membranes: the present approach, on the contrary, is based on the parametric definition of the dielectric function in the different phases, leading to a simple extension of the homogeneous PCM formalism.

To do that, the above equations can be conveniently adapted by replacing the dielectric constant ϵ with a function $f_\epsilon(\mathbf{s})$ defined at any point $\mathbf{s}$ of the cavity surface. In the computational practice a vector $\mathbf{f}_\epsilon$ is defined on surface tesserae, and Eq. 2.5 is modified accordingly:

$$\mathbf{T} = \frac{\mathbf{f}_\epsilon + \mathbf{1}}{\mathbf{f}_\epsilon - \mathbf{1}}\mathbf{S} - \frac{1}{2\pi}\mathbf{DAS}$$

Since $\mathbf{S}$ and $\mathbf{D}$ matrices do not explicitly depend on the dielectric permittivity, the changes with respect to the usual, isotropic PCM are quite limited, and the same computational strategy and algorithms for the resolution of the electrostatic problem can be used. It is worth noting that this approach is not intended to describe real liquid/liquid (or liquid/solid) interfaces, because in this case a more complex solvation charge pattern would be required: rather, it belongs to the family of electrostatic embedded QM/continuum mixed methods.

The $\mathbf{f}_\epsilon$ vector contains the local ϵ values to be assigned to each tessera: it depends on the dielectric environment shape and on the position of the solute with respect to the discontinuities. In other words, it is possible to define *sub-regions* on the cavity surface corresponding to portions of the system exposed to different dielectric media.

To give an idea of how this mixed-ϵ embedding strategy works, we report the computed change of the Fermi Coupling Constant (hfs) of the Tempo interacting with a lipid bilayer[60]. The spin-probe was settled in well shaped cavity. The membrane was modeled as a multiple layer of infinite dielectric continua so that

the dielectric constant ϵ only varies along the direction perpendicular to the membrane surface (namely the z-direction). In particular, we have adopted a three-dielectric model (see top inset of Figure 2.9), designed on the basis of the dielectric profile of the lipid bilayer: $\epsilon = 2$ inside the membrane (alkyl chains); $\epsilon = 7$ corresponding to the polar lipid heads; $\epsilon = 80$ for the aqueous environment outside the membrane. The mixed-ϵ approach allows to calculate the hfs changes (see Figure 2.9) of the Tempo as it moves from the outside (left hand side) to the inner region of the lipid bilayer (right hand side).
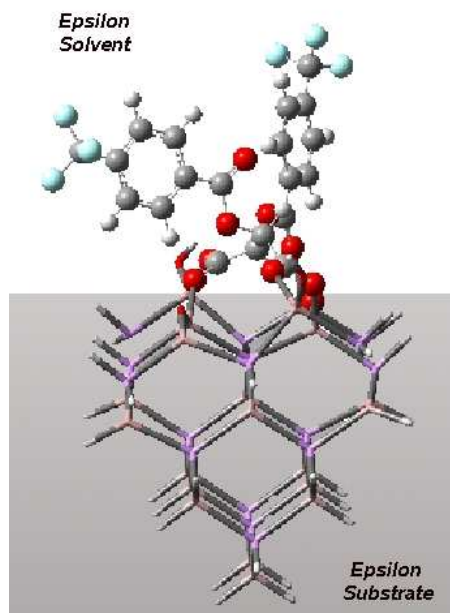
Figure 2.8: Suggestion for the use of the mixed-ϵ embedding in the interface modeling.

The same embedding strategy can be adopted to correct the finite size effect of an adduct cluster, as suggested in Figure 2.8: in this case, the surface can be regarded as a planar discontinuity between two dielectric media.
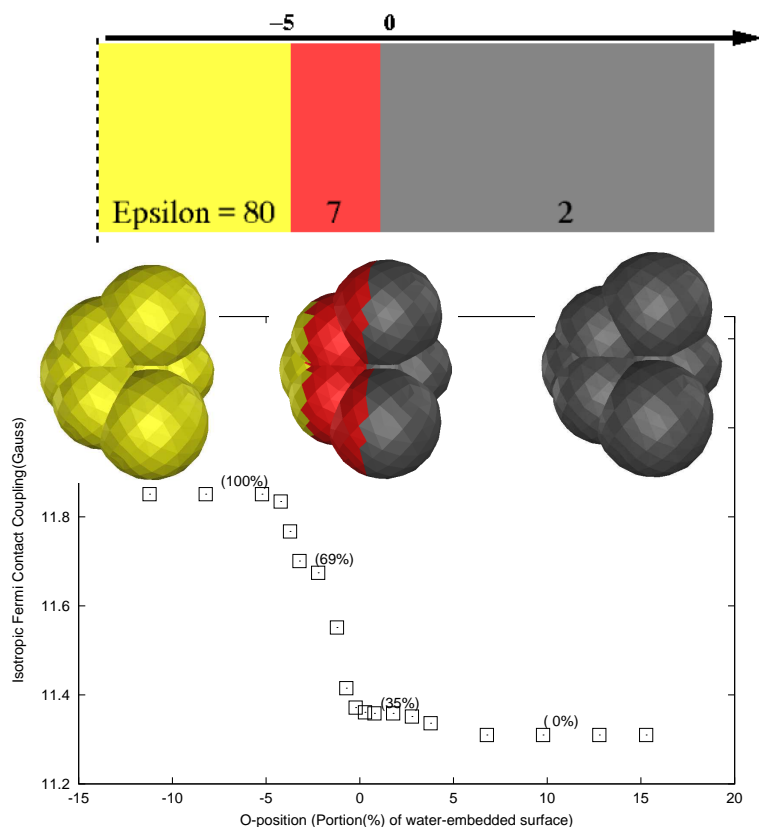
Figure 2.9: The Isotropic Fermi Contact Coupling(Gauss) of Tempo across the membrane. Values refers to the isolated Tempo molecule entering the membrane via the Oxygen atom, with the N-O bond along the z-direction. Significant points are highlighted together with the portion of water-embedded surface. All the values were calculated at PBE1PBE/EPR-II [61] level. The cluster geometry was optimized in vacuum at PBE1PBE/6-31g(d). The three dielectric model used to describe the lipid bilayer in water (see Ref. [60] for more details) is shown in the top-most inset.

CHAPTER 3

Modeling the Surface

So far a general overview of the methods used for surface modeling has been provided. Nevertheless, there is not an unique recipe for treating surface chemistry problems, the choice of the modeling strategy depending on the chemical nature of the system and the type of property under study.

Here, two modeling strategies, i.e. the saturated cluster and the unsaturated nanocluster approaches, have been applied to two different solid systems: a semi-ionic material, i.e. the anatase modification, and a covalent semiconductor, i.e. GaAs(001) surface. The following discussion aims at testing the methods (included the newly defined embedding strategies), that will be adopted in the adsorption studies presented in the next Chapters.

In the case of TiO_2 the chosen models are evaluated in terms of their energetic properties and electronic structure, whereas in the case of GaAs we focus on the ability of the selected methods to reproduce the structural properties of the real surface.

3.1   Modeling the Anatase(101)

The nanostructured anatase consists of titanium oxide clusters with diameters in the nanometer range[62]. It is important in a number of technologically applications: thanks to its enhanced surface area, it is widely used as substrate in dye-sensitized solar cell and catalytic surface chemistry[63]. Because of their finite size, the metal oxide nanocrystals have chemical-physical properties significantly different from both the bulk and the edged surface. Moreover, it has been observed that some fundamental properties change with the dimension of the crystal[64].

Theoretical investigations of nanostructured titanium oxide suffer several complications[65,66]. Because of the high computational costs, the use of standard ab-initio methods is often restricted to small molecular clusters, which are not realistic models in the nanometer range. The design of the cluster model requires particular attention, since the fictitious effects associated with the high surface-to-bulk ratio might be relatively too high. Moreover dangling bonds and strong electrostatic imbalances might cause severe problems in the convergence of widely tested computational procedures. The use of saturators often improves the convergence, but they do not correspond to the physics of real nanoclustered material: therefore their effect in the computational description should be accurately analyzed.

Here, a series of unrelaxed nanoclusters (average size 1 nm), have been studied at MSINDO and B3LYP level and the relative stability of each structure have been evaluated in term of its cohesive energy. In this context reliable results are obtained with both approaches. Furthermore the two methods have been integrated into the ONIOM fashion and applied to a larger (3 nm) cluster: the reduced computational costs allow the use of this cluster for adsorption study of large Ru-based dyes.

3.1.1   The Nanocluster Models

The anatase structure[67] belongs to the space group $I4/amd$ and has a tetragonal unit cell (Figure 3.1) where the Ti and O atoms have a distorted octahedral and trigonal planar coordination, respectively.

The surface structure of anatase nanoparticles strongly depends on the preparation and the experimental conditions: commonly used nanoparticles predominantly consist of the (101), (100) and (001) lattice planes, with an observed excess of the (101) surface.
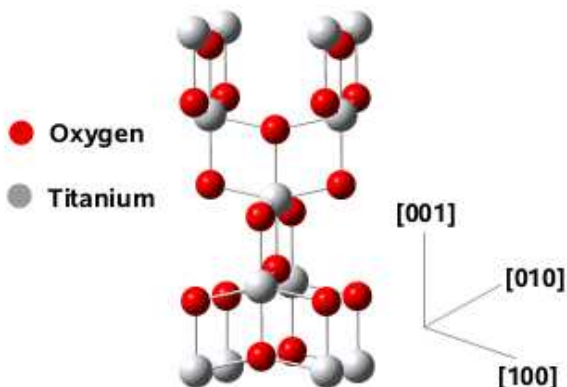
Figure 3.1: The anatase structure.

Free clusters are most suitable for simulation of ionic solids, because the structures cut out from the bulk and their fully optimized structures are very similar. Figure 3.2 shows a set of stoichiometric $(TiO_2)_x$ clusters ($x = 16, 22, 38, 54$), which adopt the geometry of the bulk anatase. Each cluster was modeled in order to expose mainly (101) surfaces. The cutting out strategy adopted in the present work follows the same criteria used by Persson *et al.*[66−70] that is, only *pure* crystals were considered, and thus no dangling bond saturators were introduced. To avoid problem of charging, stoichiometric (i.e. neutral) clusters were considered. Moreover each atom has sufficient coordination number to support its formal oxidation state in the $(TiO_2)_x$ unit. On the top layer of each cluster there is a row of di-coordinated oxygen atoms (namely O_{2c}) bound to a line of penta-coordinated Titanium atoms (Ti_{5c}) in the second layer (tetra-coordinated on the edges of the cluster). The inner layers consist of Ti_{6c} and O_{3c} atoms, with the coordination numbers reduced by one unit on the boundaries.

In adsorption studies, the use of a cluster with a net dipole should be avoided: to satisfy this criterion and preserve the stoichiometry, two *Ti vacancies* are symmetrically created on the cluster surfaces.

If N_d is the total amount of dangling bonds of a cluster, $\beta = N_d/3x$ is the average number of dangling bonds per atom. Obviously, the lower the β value, the less the *edge effect*, being predominant the bulk character in the limiting case of $\beta = 0$. For increasing x (i.e. with more and more inner atoms), the corresponding β decreases and the cluster features get closer to the solid properties.
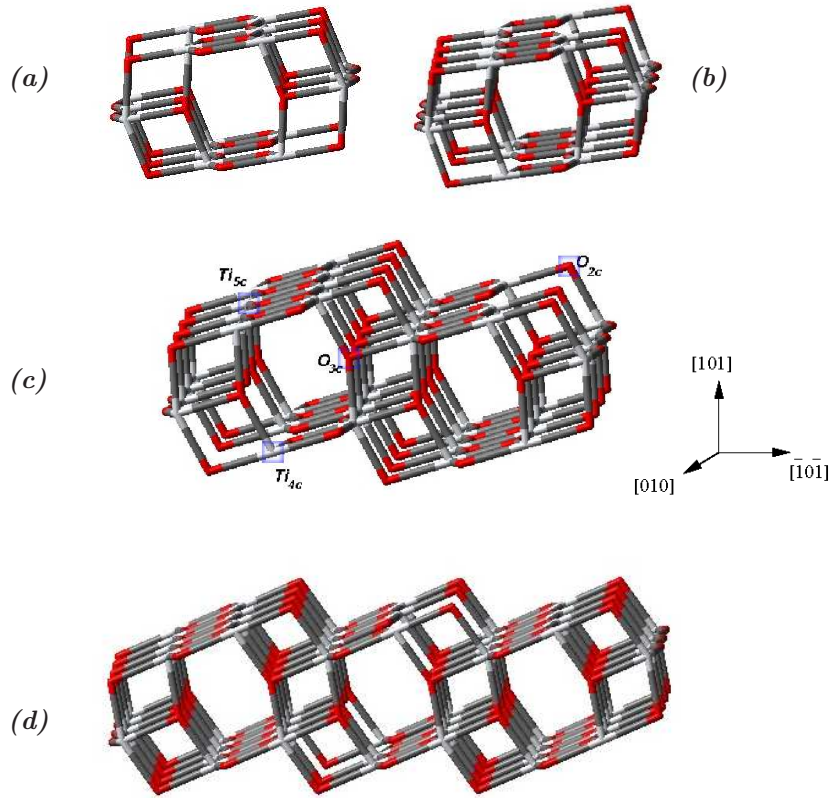
Figure 3.2: The $(TiO_2)_x$ cluster series: *(a)*: $(TiO_2)_{16}$; *(b)*: $(TiO_2)_{22}$; *(c)*: $(TiO_2)_{38}$; *(d)*: $(TiO_2)_{54}$.

First the energy and electronic structure of the unrelaxed clusters have been evaluated using the B3LYP/3-21g[2,71] methodology: according to the literature, the hybrid DFT functionals are more reliable than GGA functionals in computing ground state properties, atomization enthalpies, and band gaps of semi-ionic materials[72]. Table 3.1 reports the calculated energy per single-TiO_2 unit (Eng/x) for the four clusters, together with the corresponding HOMO and LUMO levels and the β-values. As expected, the structures with less dangling bonds (smaller β-values) are more stable.

The LUMO levels are stabilized as the cluster dimension increases, with a maximum shift of -1.23 eV; the opposite trend is observed for the HOMO levels, which are shifted at higher energies with a maximum shift of +0.23 eV for the

x	Eng/x(au)	HOMO(eV)	LUMO(eV)	β
16	-995.227725	-5.37	-3.63	1.15
22	-995.244026	-5.31	-4.28	0.97
38	-995.267458	-4.69	-4.36	0.77
54	-995.278519	-5.14	-4.89	0.69
Bulk		-7.5	-4.5	0

Table 3.1: B3LYP/3-21g calculations of the $(TiO_2)_x$ clusters series (see Figure 3.2), in vacuum.

$Ti_{54}O_{108}$ cluster. As a result the $|HOMO - LUMO|$ energy gap decreases along the cluster series. The experimental valence and conduction band edges of the TiO_2 bulk are also reported in Table 3.1. Clearly the calculated energy gaps are found to be smaller than the experimental value: in particular the HOMO values are significantly higher than -7.5 eV, indicating the lower stability of the nanoparticles with respect to the bulk, mostly due to surface-to-bulk ratio.
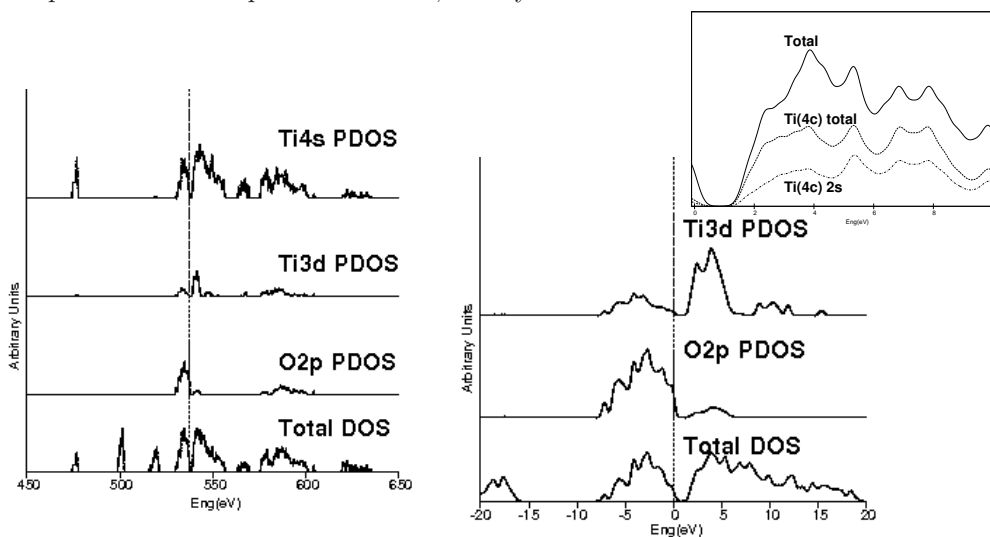
Figure 3.3: Total (DOS) and Projected (PDOS) Density of States of the $Ti_{16}O_{32}$ cluster, calculated at B3LYP/3-21g level. The top of the valence band (the vertical dashed line) is taken as the zero level.

Figure 3.4: DOS and PDOS of the $Ti_{16}O_{32}$ cluster. Focus on the highest occupied and lowest un-occupied bands. In the top right inset: the DOS and PDOS at the conduction band edge.

To analyze the electronic structure of the nanoclusters, we have constructed an

effective Density of State (DOS) through a Gaussian broadening of the individual orbital contributions (the half height weight was set arbitrarily to 0.3 eV). Furthermore, the computed DOSs are decomposed into Ti_{4s}, Ti_{3d} and O_{2p} contributions (PDOS). The DOS and PDOS of the smallest cluster (x=16) calculated at B3LYP/3-21g level is reported in Figure 3.3. Figure 3.4 shows a focus of the highest occupied and lowest unoccupied bands.

The top of the valence band is taken as the zero energy. The lower valence bands, i.e. below -17 eV (see Figure 3.4) are mainly composed of O_{2s} character. The upper valence band, i.e. above -7.5 eV, shows a strong hybridization between O_{2p} and Ti_{3d} electrons, and yields a band width of 7.5 eV, to be compared with the experimental XPS result of 4.75 eV[73,74]. The conduction bands below 13 eV consist predominantly of Ti_{3d} states, which show two distinct structures below and above 8 eV. These bands are however partially covered by a fine structure mainly due to 4s orbitals belonging to tetra-coordinated Titanium atoms (Ti_{4c}), whose presence is due by the finite size of the cluster (see top right inset in Figure 3.4).

In conclusion, despite of their high surface-to-bulk ratio, the nanoclusters display the same bonding features of the real solid, being the computed DOSs in agreement with the bulk XPS results: the upper occupied and lower unoccupied bands are mostly due to a strong hybridization between the O_{2p} and Ti_{3d} electrons.

3.1.2 Methods

The *cohesive energy* (E_c) is the energy difference between the crystal and its constituent gas-phase atoms. Here, the cohesive energy may be defined simply as the energy per TiO_2 unit, E/x, taking the summation of the B3LYP energies of the atomic $Ti(^3F)$ and $O(^3P)$ (E_{atoms}) as the reference state:

$$E_c = \frac{E}{x} - E_{atoms} \qquad (3.1)$$

i.e. the higher the E_c, the more stable the nanocluster. The calculated MSINDO and B3LYP/3-21g cohesive energies of the $(TiO_2)_x$ are reported in Figure 3.5 as a function of the β-values. The experimental bulk energy of atomization, $\Delta_a H$, is also reported for comparison.

A quasi-linear increase of the B3LYP/3-21g cohesive energies of cluster with decreasing β values is found, consistently with the size effect. This is a well known

characteristic of the semi-ionic real crystals[75−77]. One can therefore study the anatase single crystal energetic properties in terms of extrapolated cluster energy, in the limiting case of $\beta = 0$.

The extrapolated $\beta = 0$ value is found to be around 200kJ/mol above the experimental value. However experimental $\Delta_a H$ includes contribution from the zero-point energy and thermal corrections, whereas the computed energies do not. Moreover, the calculated values refer to un-relaxed clusters, rather than stable ones. Therefore the computed values have to be analyzed as relative terms among the trend, eventually considering the energy shift from the $\Delta_a H$.

Interestingly, the same linear trend is obtained at MSINDO level. For a given cluster, the MSINDO energies are below the B3LYP/3-21g values, the difference being constant among the cluster series: the energy shift is not size dependent. This is quite remarkable: the semiempirical MSINDO method, which is computationally less accurate and demanding than DFT, provides reliable relative binding energies, if compared with the B3LYP values.

It is worth noticing that the B3LYP/3-21g energy for the $x = 54$ cluster is very close to the experimental bulk value. Although the calculated B3LYP energies depend on the used basis sets, a detailed analysis of the basis set effect in reproducing the semi-ionic nature of the $Ti \cdots O$ bond is not necessary in the present work, since relative rather than absolute energies are considered.

Since the ab-initio treatment of the largest cluster ($x = 54$) is computationally expensive, a systematic investigation of the dye adsorption modes on anatase is hardly performed. Nevertheless the use of smaller clusters restricts the study to the cases of small dyes or unlikely anchoring modes.

The use of the $Ti_{54}O_{108}$ cluster is possible by using the integrate B3LYP:MSINDO approach. The selection of the high level system requires a special attention since the same criteria used for designing the whole cluster can not be valid simultaneously for the high level portion. The model system has to be computationally reliable and large enough to eventually support the adsorbed molecule. Often the geometries best satisfying these criteria have a non-null dipole moment and are not stoichiometric. If the stoichiometric request decades, it is then mandatory not to introduce spurious effects due to unphysical charges. These effects can be avoided by choosing "saturators" as link atoms.

Our model system consists of two separate portions (see Figure 3.6): each portion is made by two adjacent Ti_2O units, so that before the saturation, the model keeps the correct stoichiometry. The Ti atoms having a coordination number lower than four (the minimum required to support the formal oxidation state) are saturated with -OH groups; similarly, mono-coordinated Oxygen atoms are saturated with -H atoms. The obtained model system (namely $[Ti_2O_4{:}3H_2O]_2$)
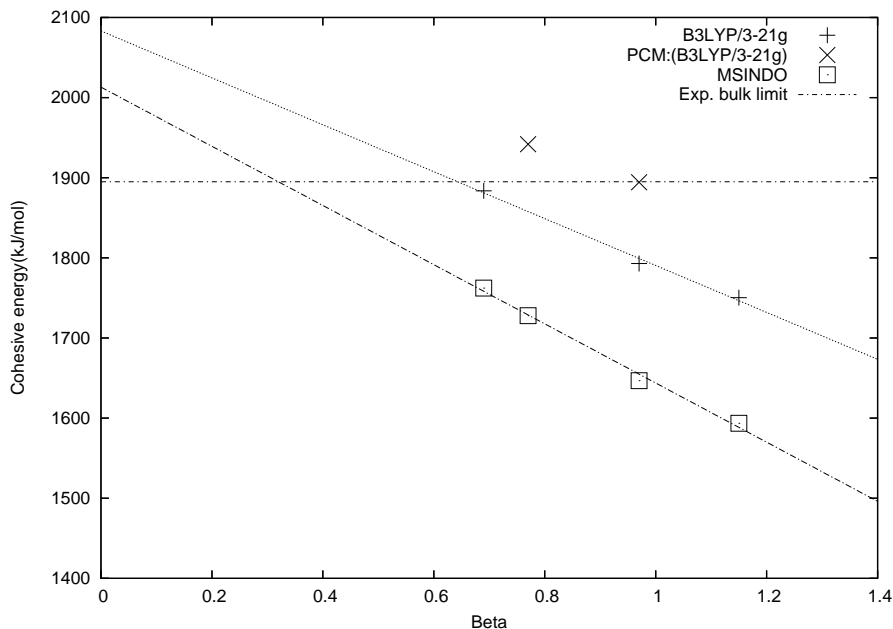
Figure 3.5: The Cohesive Energies (kJ/mol) as a function of β. Values are calculated at B3LYP/3-21g and MSINDO level. The experimental bulk value is also reported.

is shown in the bottom-left inset of Figure 3.6. The cluster is then treated at ONIOM(B3LYP:MSINDO) level and will be referred to as ONIOM-Ti$_{54}$ approach.

Table 3.7 reports the binding energies of the Ti$_{54}$O$_{108}$ cluster computed at B3LYP, MSINDO and B3LYP:MSINDO level. Considering the size-extensive nature of the calculated cohesive energy and the almost constant (i.e. size-independent) energy shift between the MSINDO and B3LYP values, the found ONIOM-Ti$_{54}$ value is well in agreement with the expectation, being close to the MSINDO value, well below the B3LYP value. Finally the HOMO and LUMO levels and the $|HOMO - LUMO|$ gap (ΔG) of the Ti$_{54}$ clusters, calculated with the B3LYP/3-21g, MSINDO and ONIOM approaches are reported in Table 3.7, together with the bulk value. The ONIOM ΔG is found to be close to the experimental band gap. Interestingly, even the absolute energies of the ONIOM HOMO and LUMO levels are close to the optical experimental value.
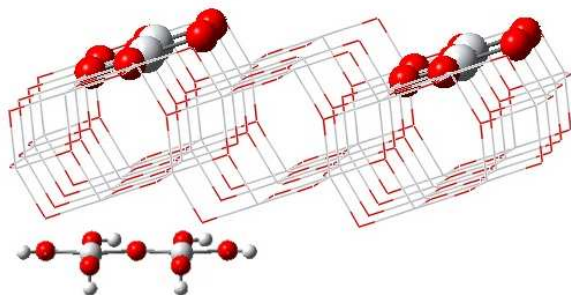
Figure 3.6: The ONIOM-Ti_{54} approach: the $Ti_{54}O_{108}$ is taken as real system; the model system consists of two regions opportunely saturated (Ti_2O_4:$3H_2O$, bottom-left inset).

Method	HOMO(eV)	LUMO(eV)	ΔG	Binding Eng. (kJ/mol)
B3LYP	-5.14	-4.89	0.26	1884
ONIOM	-6.84	-4.27	2.58	1763
MSINDO	-6.22	-0.97	5.24	1762
Bulk	-7.5	-4.5	3.0/3.2	1895

Figure 3.7: The HOMO and LUMO levels(eV), the $\Delta G = |HOMO - LUMO|$ gap and the binding energy (kJ/mol) for the $x = 54$ cluster. Comparison between the B3LYP, the MSINDO and the ONIOM(B3LYP:MSINDO) results. The bulk value are also reported.

In conclusion, the ONIOM-Ti_{54} approach is computationally feasible and at the same time provides a reliable description of the ground state optoelectronic properties, if compared with both the B3LYP/3-21g and the experimental results. Therefore it is suitable for adsorption study of large dyes.

3.2 Modeling the Reconstructed GaAs(001) Surface

In the following Sections, the GaAs(001) surface will be studied with the aid of a saturated cluster geometry, the attention being focused on the reliability of the chosen approaches in modeling the structural feature of the real reconstructed

surface. Such a modeling is a much needed preliminary step to describe addition reactions of organic molecules on this surface. We will consider both clean and oxidized surfaces, since most applications are realized in the presence of a top oxide layer: different oxidation patterns will be analyzed and compared to recent spectroscopic and microscopic evidences.

3.2.1   Clean Surface

The GaAs(001) surface can reconstruct in several different arrangements, whose relative energies have been long debated[78−88]: As-rich surfaces are usually grown under conditions leading to a (2×4) reconstruction[82−86] (i. e. with a two dimensional periodic structure whose unit cell is 2 times the bulk lattice distance in one direction and 4 times in the other). Among the possible (2×4) structures, recent calculations and accurate scanning tunneling microscopy (STM) experiments indicate the so-called $\beta_2(2 \times 4)$ as the most likely in usual conditions[83,84]: this structure is sketched in Figure 3.8. In the present work, we will always refer to this surface: as can be seen in the schematic picture, the uppermost layer is formed by Arsenic dimer pairs, arranged in parallel rows, which are separated by quite deep trenches. Below each Arsenic dimer pair, six Gallium atoms form the base of these protruding "platforms": four of the Gallium atoms have unsaturated valences (dangling bonds); other Arsenic dimers are formed on the bottom of the trenches.

The smallest model used for the GaAs surface is the $Ga_{20}As_{20}H_{32}$ cluster shown
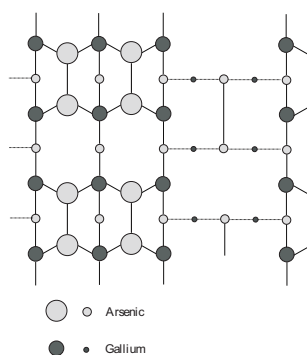
Figure 3.8: Schematic picture of the GaAs(001)-$\beta_2(2 \times 4)$ surface.
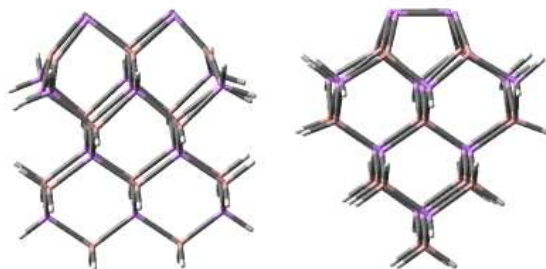
Figure 3.9: Side views of the $Ga_{20}As_{20}H_{32}$ cluster.

in Figure 3.9: it is a 8-layer cluster, cut out from the bulk crystal structure, where all the edge atoms are terminated with hydrogens, except those of the two first layers from top (the "surface atoms"). This cluster, modeling the protruding platforms observed on the GaAs surface, was studied at DFT level by Sexton and co.[84] and the obtained results were compared with the ones from a DFT periodic-slab approach: the termination effects were found to be substantial for the cluster treated with an hybrid non-periodic DFT methodology and terminated with hydrogen atoms. In particular it was found that hydrogens introduce significant perturbation in the electronic structure of the cluster-edge atoms. Focusing on the structural features, the distortion effects due to the presence of the hydrogens are expected to be centrosymmetric with respect to the central As-dimers. For this reasons we have not investigated the use of differently charged saturators.

The structure of the cluster was optimized with DFT, MSINDO and mixed
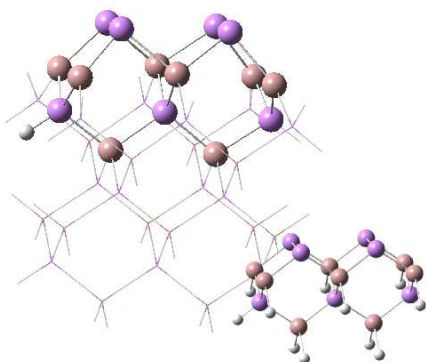
Figure 3.10: $Ga_{20}As_{20}H_{32}$ cluster in the ONIOM calculations: the small portion treated at the DFT level is highlighted. Bottom right inset: the high level region with the link atoms.

DFT:MSINDO methods, to compare the performances of the three approaches on this cluster. The DFT calculations has been performed using the PBE1PBE density functional, i.e. a GGA functional, based on the Perdew, Burke and Ernzerhof functional[89](PBE), and modified as reported in Ref. [3]. It is a hybrid functional, being the amount of the HF contribution derived from fundamental physical constraints[3]. The Pople 6-31G[90] basis set has been employed on second row elements, supplemented in some cases by extra polarization functions on hydrogen and heavy atoms,[91] and by diffuse functions on heavy atoms[92] (the resulting set being indicated as usual as 6-31+G(d,p)). On Gallium and Arsenic atoms the LANL2DZ set of pseudopotentials and basis[93−95] has been used; in some calculations, the Ga atoms close to the surface have been assigned an enlarged set, referred to as LANL2DZ(d), including d polarization functions with exponent 0.451.

The cluster treated at PBE1PBE:MSINDO level is shown in Figure 3.10. The chosen links atoms were again hydrogens. Note that in order to have an even number of electrons, one As valence was not saturated (see the bottom right inset in Figure 3.10). Nevertheless the resulting distortion effects were acceptably small.

In all the optimizations, the positions of all the atoms in the first 5 layers from
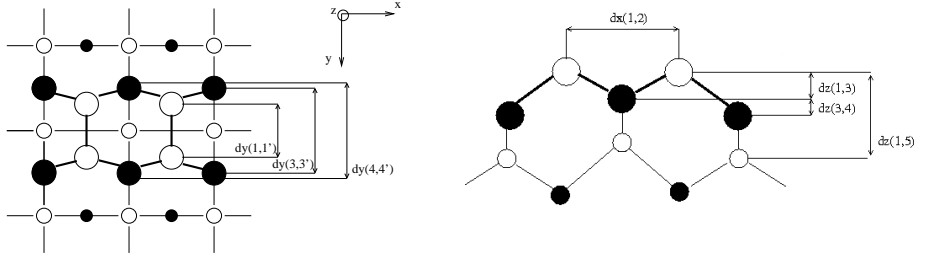
Method	$dy_{1,1'}$	$dy_{3,3'}$	$dy_{4,4'}$	$dx_{1,2}$	$dz_{1,3}$	$dz_{3,4}$	$dz_{1,5}$
MSINDO	2.47	3.71	3.59	3.90	1.57	0.15	3.00
ONIOM[a]	$\frac{2.66}{2.64}$	$\frac{3.95}{3.85}$	3.81	4.15	$\frac{1.48}{1.61}$	$\frac{0.27}{0.25}$	$\frac{3.06}{3.12}$
PBE1PBE	2.63	3.72	3.62	3.98	1.62	0.18	3.08
PW-LDA Ref. [84]	2.50	3.65	3.52	3.82	$\frac{1.41}{1.44}$	0.28	
Exp. Ref. [96]	2.2						
Exp. Ref. [97]	2.4						
Exp. Ref. [86]	2.73						

(a) The upper (lower) value is referred to the small system side where the As-H bond was kept (discarded).

Figure 3.11: Most relevant geometrical parameters (Å) for the $Ga_{20}As_{20}H_{32}$: calculated and experimental values.

the bottom were frozen in their bulk values (Ga-As bond distances are 2.46 Å). The most relevant geometrical parameters, labeled according to the formalism shown on the top of Figure 3.11, are reported (bottom of Figure 3.11), together with the experimental values. The same parameters, computed[84] at periodic-LDA level with a slab model, are also reported for comparison.
There is a lack of consensus regarding the experimental dimer length in the lit-

erature[86,][96−98], the reported values ranging between 2.2 Å from XPD study [96], and 2.73 Å from secondary-ion mass spectroscopy investigations[97]. Other structural parameters as interplanar distances and relaxations in inner layers are even less known than the As-dimer length. For all the reported approach the As-dimer length are fairly in the range of reported experimental values. Moreover the computed values are in good agreement with the bond distance of 2.51 Å found for the bulk As, i.e. where the Arsenic atoms are threefold coordinated [99].

The two DFT calculations have many structural features in common, such as the dimer reconstruction and the corresponding upward displacements. Besides, by comparing the computed lengths, the non-periodic cluster structure is found to be more relaxed, expecially along the x and y-axis. Clearly this is due to the lack of a periodic environment in the cluster model. The dimer length in the periodic calculation is found to be shorter than the one in the cluster model, being 2.50 Å in the former case and 2.63 Å in the latter. Other periodic LDA calculations [85,100] in literature state values of 2.39 and 2.60 Å, respectively.

In the framework of the cluster approach, the PBE1PBE:MSINDO procedure proves to be a reliable computational strategy: the As dimer geometry is very similar to that of the full quantum calculation, and also the distance between the dimers and the underlying Ga atoms is fairly well reproduced. The main difference is that the Ga layer is wider when optimized by ONIOM (see $dy_{3,3'}$ and $dy_{4,4'}$ in Figure 3.11). The asymmetry due to the unequal treatment of the As-H bonds in the third layer is limited: the largest difference is in the distance between the first and the second layers ($dz_{1,3}$), which is lower than 9%; on the other hand the As dimers ($dy_{1,1'}$) are practically equivalent.

A larger model is depicted in Figures 3.12: this $As_{73}Ga_{77}H_{100}$ cluster comprises a row of three As dimer pairs (three "platforms") bordered by two trenches: two other As dimers are present on the bottom of each trench. To lower the computational burden, this cluster is thinner, including only 6 layers, and it is no longer stoichiometric: the structure of the surface, however, is still correct. The cluster was optimized at the PBE1PBE:MSINDO level: as before, the atoms of the innermost layers (three from the bottom in this case) are frozen in their bulk position. In the first optimization, the atoms of the central platform were treated at DFT level (see Figure 3.12), the low level being MSINDO as before: the main geometrical parameters are listed in Figure 3.13. As one can see, the As dimer structure is very similar to that optimized with ONIOM in the $Ga_{20}As_{20}H_{32}$ cluster (Figure 3.11), confirming the reliability of the smaller model and the local character of this feature of the reconstructed surface.
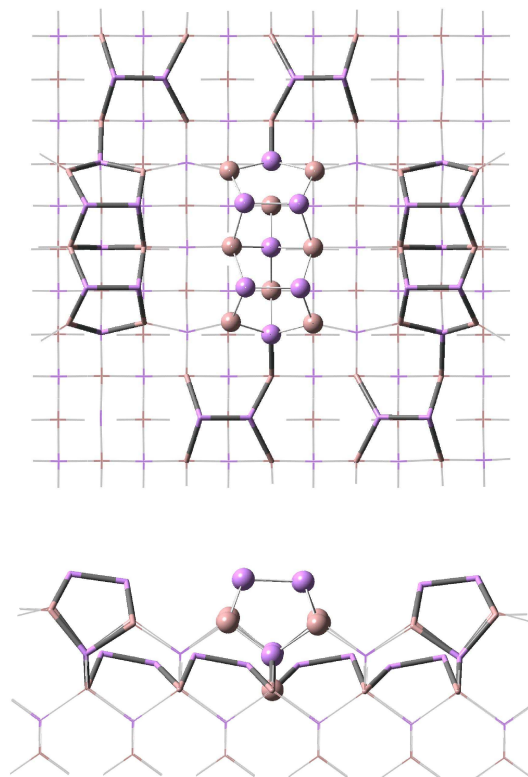
Figure 3.12: $As_{73}Ga_{77}H_{100}$ cluster: high level on the top dimers.

3.2.2   Oxidized Surface

Some experimental (STM) results [101,102] indicate that in the oxidized surface the top oxide layer is formed by Ga_2O_3, resulting from the displacement of metallic Arsenic: [103] it has been found that the most likely oxidized structure is obtained by displacing adjacent pair of As-dimers. The displayed As atoms can collect into metallic grains settled either in the bottom of the trenches or on the non-oxidized platforms, binding in any case to other As dimers. The observations seem to indicate that the preferred antisite for Arsenic grains growth is on the top of the platforms, but this is still debated.

$dy_{1,1'}$	2.58 / 2.60$^{(a)}$	$dz_{1,3}$	1.68
$dy_{3,3'}$	4.04 / 3.89$^{(a)}$	$dz_{1,5}$	3.08
$dy_{4,4'}$	3.85	trench dimer length	2.37
$dx_{1,2}$	3.99	trench dimer buckling angle	10.4

(a) See Figure 3.11, note (a).

Figure 3.13: Most relevant geometrical parameters (Å, degrees) of the optimized $As_{73}Ga_{77}H_{100}$ cluster (see top of Figure 3.11 for parameter definition).

First, we consider an oxidation process leading to the formation of a *supra dimers* metallic cluster. We have taken the $Ga_{20}As_{16}O_4H_{32}$ and $Ga_{20}As_{22}H_{32}$ (see left and right hand side of Figure 3.14, respectively) clusters to model the oxidized portion and the supra-dimers As cluster formed upon oxidation of the ideal surface. These clusters were optimized at PBE1PBE and PBE1PBE:MSINDO levels. The high level portions, for the ONIOM calculations on the oxidized and supra-dimer clusters, were selected using the same strategy adopted for the bare cluster (see previous paragraph, Figure 3.10).

The main geometrical features of the stable $Ga_{20}As_{16}O_4H_{32}$ structures were compared in Table 3.2, still referred to the parameters illustrated in Figure 3.11.

G$a_{20}As_{16}O_4H_{32}$ **G**$a_{20}As_{22}O_{32}$
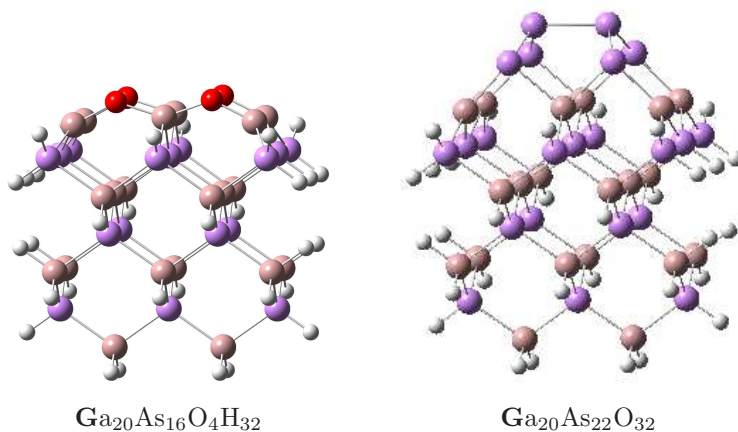
Figure 3.14: Oxidized (left) and supra-dimer(right) cluster models.

The oxygen atoms are much more "buried" in the underlying Ga layer than the Arsenic was ($dz_{1,3}$ and $dz_{1,5}$ markedly smaller), with the result that the oxidized platform is almost flat, and leaves the Ga atoms more available for nucleophilic attacks, an effect which is enhanced by the oxygen greater electronegativity.

The HOMO/LUMO gaps (ΔE), together with the average Mulliken charges on the first two layers, computed for the bare, oxidized and supra-dimer clusters at PBE1PBE and ONIOM levels are reported in Table 3.3. The ΔEs calculated with the PBE1PBE:MSINDO approach are significantly smaller than those calculated at PBE1PBE level, mostly because of the presence of undersaturated As atoms in the high level region. Moreover, the ΔEs of the oxidized cluster are smaller than those of the bare cluster, i.e. the oxygen and displayed atoms induce states into the band gaps of the semiconductor, causing the Fermi level pinning observed experimentally.
With both the methods, the average charge on second layer Ga atoms in the $Ga_{20}As_{16}O_4H_{32}$ cluster is much high if compared with the one in the bare cluster, i.e. the charge separation occurring at the surface increases upon oxidation. The presence of positively charged Ga atoms on the surface explains the observed ability of the oxidized GaAs surface to adsorb electron-rich species. From this point of view, the cluster model is suitable for chemisorption studies.
The reaction mechanism of the oxide formation process is plotted on Figure 3.15.

Oxidation energies (ΔE_{oxo}, shown in Table 3.4) were computed from the formation enthalpies (H_f) according to "products minus reactants" scheme (see Figure 3.15):

$$[H_f(oxo) + 2 \times H_f(supra)] - [3 \times H_f(bare) + 4H_f(O)]$$

The H_f were approximated with the calculated total energies of the stable clus-

	DFT	ONIOM
$dy_{1,1'}$	4.52	4.08 / 4.11[a]
$dy_{3,3'}$	4.24	4.12 / 3.94[a]
$dy_{4,4'}$	4.29	3.91
$dx_{1,2}$	3.24	3.55
$dz_{1,3}$	0.78	0.82
$dz_{1,5}$	1.84	2.11

Table 3.2: Most relevant geometrical parameters (Å) for the $Ga_{20}As_{16}O_4H_{32}$ cluster optimized at various levels (see Figure 3.11 for parameter definition and for note (a)).

	PBE1PBE			ONIOM		
	ΔE(eV)	CHG_{Ga}	$CHG_{As/O}$	ΔE(eV)	CHG_{Ga}	$CHG_{As/O}$
Bare	1.77	0.35	-0.13	0.72	0.27	-0.18
Supr.	1.17	0.54	-0.18			
Oxid.	1.71	0.94	-0.88	0.65	0.58	-0.65

Table 3.3: The $\Delta E = HOMO - LUMO$(eV) energy gaps, the average Mulliken charges at the top two layers computed at PBE1PBE and ONIOM level on the bare, oxidized and supra-dimer clusters.
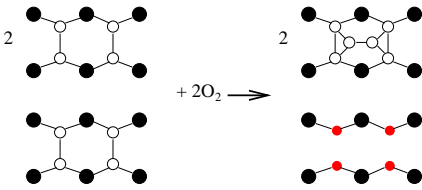
Figure 3.15: The "products minus reactants" schemes for the oxidation reaction. In this reaction mechanism the displayed As atoms form a supra As-metallic cluster, settled above a pairs of As-dimers.

	ΔE_{oxo}(eV) per O
PBE1PBE	-2.81
ONIOM	-2.66

Table 3.4: The oxidation energies (eV) of the reaction depicted in Figure 3.15

ters, while the $H_f(O)$ is the gas phase atomic energy of O(^{3}P). Again the ONIOM enthalpies are in good agreement with the PBE1PBE values. It is somehow interesting to note that the computed enthalpies are surprisingly in good agreement with the experimental enthalpy of the oxide formation process (2.69 eV), whose mechanism (in term of number of O atoms inserted and As atoms displaced) is not yet clear[104 − 107].

The most likely antisite for metallic Arsenic growth is still under discussion: STM observations indicate the top of dimers platform as the preferred antisite, but the bottom of the trench can also collect the displaced As atoms. To help clarifying this point, we optimized two different oxide structures, namely $As_{109}Ga_{108}O_2H_{109}$, resulting from the substitution of two As atoms on a row of dimer pair. In one case the two displaced As atoms are bound to two dimers in the trench bottom (Figure 3.16), in the other case they form the supra-dimer cluster (Figure 3.17).

The thermodynamic preference between the two antisite has been estimated by
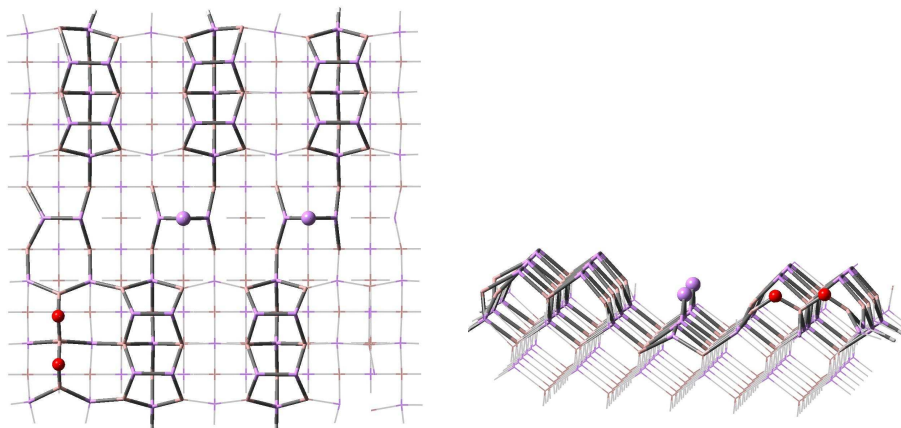
Figure 3.16: $As_{109}Ga_{108}O_2H_{109}$ cluster optimized at MSINDO level, with the displaced As atoms in the trench bottom.

computing at the ONIOM level the energy for the reaction

$$As_{109}Ga_{108}H_{109} + O_2 \longrightarrow As_{109}Ga_{108}O_2H_{109}$$
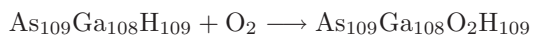
for the two product isomers (Figures 3.16 and 3.17). In both cases, the high level region comprised the O atoms, the displaced As, and the portions of the GaAs surface underlying the oxidation sites and the As antisites.

In conclusion, the two postulate structures resulting from the oxidative process are not thermodynamically equivalent, being the antisite on the platform top (the supra dimer cluster) preferred by 11 kcal/mol per displaced As atom.
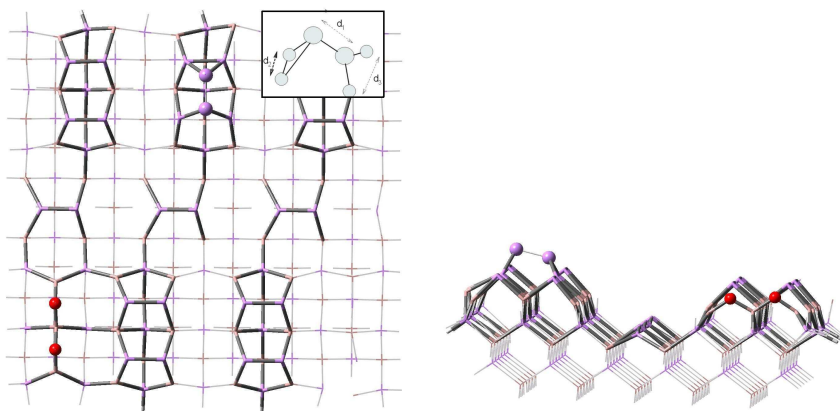
Figure 3.17: $As_{109}Ga_{108}O_2H_{109}$ cluster optimized at MSINDO level, with the displaced As atoms on a platform top.

CHAPTER 4

Organic Acids on the GaAs(001) surface

It is widely recognized that the physical and chemical activity of metals and semi-conductors can be greatly enhanced by the solid surface functionalization with suitable organic layers[108 − 110]: the performance of electronic and optoelectronic devices involving such modified surfaces can be opportunely adjusted by adapting the chemical nature of the adsorbed molecules[111 − 115]. The use of modified surfaces is very promising for nanoelectronic applications, thanks to the great variety of available molecules and the relative ease to design and synthesize new, specifically tailored species.

Poly-functional molecules are commonly employed, with some groups designed to ensure a strong binding to the surface[116 − 124], and other groups designed for the specific chemical and physical functions required.[125]

Among the numerous applications, one can cite molecular sensors for organic and biochemical species,[125] modified diodes[117 − 119], [126], transistors and other electronic devices,[127,128] and dye-sensitized photovoltaic cells[129]. In all these cases, the design and the interpretation of the modified surface properties require a reliable modeling of the organic layer structure and of the molecule-surface binding at the atomic scale.

In recent years, the GaAs(001) surface modified with an organic acid monolayers

has been encountered in many applications: benzoic and aliphatic carboxylic acid layers have been used to enhance the wettability of oxidized GaAs surfaces by liquid crystals in the preparation of 2-D photonic crystals[130]. Benzoic and hydroxamyc acid derivatives with varying dipole moments have been used to tune the surface work function and hence the performance of GaAs[121,[131−133]] photovoltaic cells.

In the following Section, the binding mode of the benzoic acid on oxidized GaAs surface will be investigated, focusing on the substrate/adsorbate interaction as well as long range adsorbate/adsorbate interaction. Finally, the influence of an homologue series of dicarboxylic acid derivatives on the surface electronic properties has been studied, seeking for a correlation between the observed work function changes and the microscopic properties of the substrate/adsorbate interface.

4.1 Benzoic Acid on the GaAs(001) Oxidized Surface.

Very few is known about the most likely binding modes and adsorption sites of the benzoic acid on the GaAs oxidized surface. From FTIR analysis it has been suggested that the anchoring mechanism on both CdTe and on GaAs is dissociative, leading to a bidentate bridging coordination to Cd[134,135] in the former case, to a bidentate bridging or monodentate coordination to Ga[136] in the latter case. Our aim is to investigate the binding preference with the aid of suitable computational approaches. First a set of possible single-molecule adsorption structures have been modeled, by comparing the benzoic acid stable geometry with the geometrical features of the oxidized GaAs(001) surface model. The obtained adduct models have been then optimized by using a hierarchy of computational approaches, discarding, at each optimization step, the thermodynamically less stable geometries. Furthermore the reliability of the obtained stable adducts was investigated by comparing the computed vibrational frequencies with the FTIR spectra. Once the local adsorbate/surface interaction has been studied, the cooperative effects associated to the adsorption of more than one molecule in neighboring sites were evaluated on a large cluster model of the oxidized surface.

4.1.1   Adsorption Sites

Our first goal was to determine the preferred adsorption sites for benzoic acid on an oxidized platform, using the $Ga_{20}As_{16}O_4H_{32}$ cluster (see Section 3.2.2, Figure 3.14). It is commonly assumed that the oxidized surface is more basic than the benzoic carboxylate, so that the first step is the protonation of one of the surface oxygens: actually, in all the adduct geometry optimizations described below, even when starting from undissociated acid, the carboxylic hydrogen left the organic molecule to protonate the surface.

The benzoate can bind to the Ga atoms through monodentate (M), bidentate chelating (BC) or bidentate bridging (BB) modes (Figure 4.1): considering that six Gallium atoms are available, and that one of the oxygens has been protonated, there are eight possible adduct arrangements, as depicted in Figure 4.2.

To avoid pentavalent Ga atoms, the carboxylate should bind to the "external"
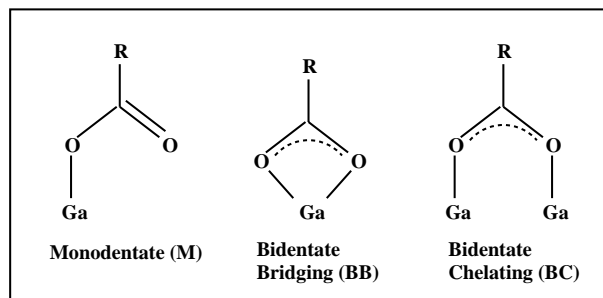
Figure 4.1: Binding modes for benzoate on Ga atoms.

atoms (1, 2 or 5, 6), which carry empty orbitals (dangling bonds) suitable for the nucleophilic attack: the 3,4-BB adduct was included since the protonated oxygen can easily leave the Ga(3) restoring a proper coordination, at least on this side of the bridge. For the same reason, the only BC mode involves the Ga(5); M modes on Ga(1) and (2) can be considered similar to that on Ga(6): moreover, we shall see in the following that the preferred binding sites concentrate around the protonated oxygen, which "activates" the neighboring Ga atoms by weakening the Ga-O bonds.

The first screening was performed by optimizing the geometry of the eight adducts at the PBE1PBE:MSINDO level, and then computing the adsorption energy, $E_{ads} = E_{adduct} - E_{cluster-H^+} - E_{benzoate}$, as single-point calculations at the PBE1PBE level. In all the DFT calculations the 6-31G basis set was used on first and second row atoms, while the LANL2DZ set of pseudopotentials and
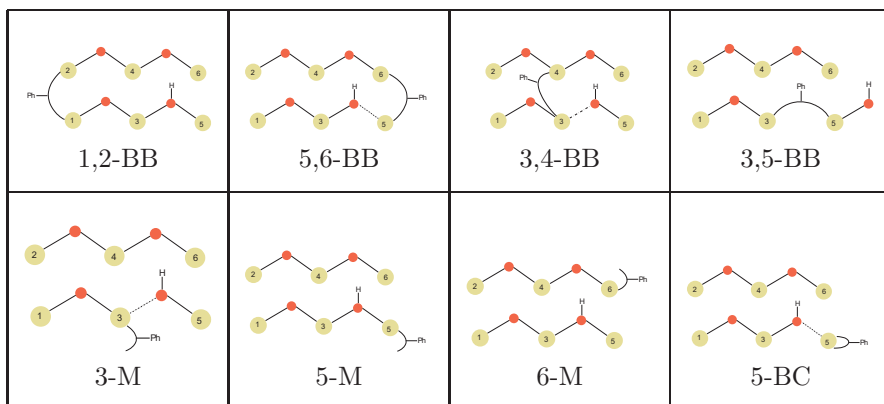
Figure 4.2: Possible arrangements for benzoate adsorbed on the protonated surface. Large and small circles refer to Ga and O atoms, respectively.

corresponding basis set were used on As and Ga. In the ONIOM procedure, the high level layer comprised the organic moiety, the four surface oxygens and the six underlying Gallium atoms.

Four structures (see Figure 4.2) resulted most stable, namely 5,6-BB, 3,4-BB, 3,5-BB and 5-BC, that was actually indistinguishable from 5-M: one can see that the nucleophilic attacks take place preferably around the protonated oxygen. Interestingly, we could not find a stable minimum for 1,2-BB, since the surface OH group attracted the benzoate towards the other side of the platform, ending up with the 5,6-BB structure.

In the second step the selected structures were re-optimized at the PBE1PBE level (then extending the high level calculation to the whole adduct), and E_{ads} was computed at the same level: this leads to exclude the 3,4-BB structure also. Finally, the last three adducts were optimized and E_{ads} was computed with a larger basis set, namely 6-31G(d,p), with the results reported in Table 4.1. Two adduct structures are clearly favored, namely 5,6-BB and 5-BC: they are on the same side as the protonated oxygen, as expected, and their relative energy is small enough to allow the presence of both, though the former is more likely; all the other structures have energies far too high to be plausible.

This result can be checked by computing the vibrational frequencies associated with the carboxylate group, which are expected to be quite sensitive to the binding mode: the most relevant parameter is the splitting between the symmetric and antisymmetric stretching modes, $\Delta\nu_{str}$, which is related to the amount of charge delocalization between the oxygens. In Table 4.1 we report the harmonic frequencies computed for the carboxylate stretching in the three adducts, along

Ads. mode	$E_{ads}^{\dagger}$	ν_{asymm}	ν_{symm}	$\Delta\nu$	Exp. $\Delta\nu$ [136]
5,6-BB	0.0	1593	1450	143	
5-BC	8.0	1638	1500	138	135
3,5-BB	38.0	1605	1491	114	

†: Adsorption energy with respect to the $E_{ads}^{5,6-BB}$.

Table 4.1: Relative adsorption energies (kcal/mol) and carboxylate stretching harmonic frequencies (cm^{-1}), computed at the PBE1PBE/6-31G(d,p) level for the three most stable adducts

with the experimental $\Delta\nu_{str}$ measured by Bastide *et al.*[136] for a monolayer of benzoic acid on GaAs. One can see that the experimental evidence agrees with 5,6-BB or 5-BC binding, confirming the E_{ads} trend. Note that the same authors report a $\Delta\nu_{str}$ of 144 cm^{-1} for the free carboxylate (i. e. when the two oxygens are perfectly equivalent): both the computed and the measured frequency splitting indicate that in the adduct this equivalence is preserved fairly well.

4.1.2 Cooperative Effects

Having determined the preferred adsorption sites for a single molecule, the structure of highly packed organic layers have been investigated. A preliminary information can be obtained by computing the interaction energy of two benzoic acid molecules in different orientations: the isolated molecule geometry was optimized at the PBE1PBE/6-31G level, then the dimer energy was scanned with respect to the intermolecular distance, without re-optimizing the two fragments, in the three arrangements shown in Figure 4.3. The resulting curves are reported in Figure 4.4: in the Side-to-Face orientation a minimum exists at 5.3 Å, with a small stabilizing energy of about -1 kcal/mol with respect to the two isolated fragments; on the other hand, the Side-to-Side and Face-to-Face arrangements produce repulsive curves at all distances.

To analyze the intermolecular interactions in the adsorbed layer, we used the larger model of the oxidized surface, namely the $Ga_{108}As_{85}O_{24}H_{109}$ cluster presented in Figure 4.5: it comprises two adjacent rows of fully oxidized "platforms" (containing Oxygen instead of As atoms on the platform top) separated by a trench with three As dimers on the bottom.
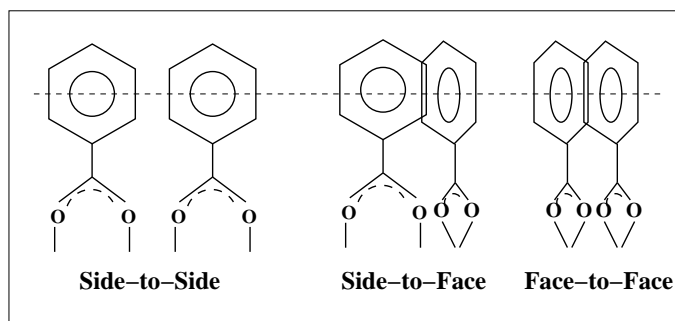
Figure 4.3: Different orientations for the benzoic acid dimer.

As shown in the previous Section, the first benzoic acid is likely to bind as in Figure 4.5 (i. e. in BB mode on two Ga's close to the protonated oxygen): this adduct was optimized at the PBE1PBE:MSINDO level, including in the DFT layer the organic molecule and the linked Ga atoms, with the 6-31G basis set.

The final geometry is close to that obtained for the small cluster in the previous Section, even if in this case the two CO-Ga bonds become quite asymmetric, though maintaining the bridging character. Interestingly, the ring plane is strongly bent towards the surface, indicating that the trench is wide and deep enough to accommodate the molecule with no or very small steric repulsion; on the other hand, a simple inspection of the adduct shows that it is not possible to bind two molecules on opposite platforms. We also optimized an adduct in the BC binding mode on one of the corner Ga atoms (see above): the adsorption energy resulted practically the same as for the BB mode (as already found for the small cluster, see Table 4.2).

Some possible arrangements for a second adsorbed molecule (in high coverage conditions) are schematically depicted in Figure 4.6. Structures (a) and (b) contain two molecules bound in BB mode, with Side-to-Side arrangements, while (c) and (d) are examples of Side-to-Face between molecules bound in BB and BC modes; due to the geometry of the adsorbed molecules, strongly bent towards the surface as said above, the Face-to-Face arrangement cannot be found. The adducts with two benzoic acids were optimized and the adsorption energy was computed at the ONIOM level, with the 6-31G basis set in the DFT layer; as above, the quantum chemical calculation was restricted to the organic moiety and to the Ga atoms involved in the bonds. The resulting energies per adsorbed molecule are reported in Table 4.2.

In agreement with the results of the dimer energy scan, only the Side-to-Face arrangement of two molecules on adjacent sites, as in Figure 4.6(c), shows a sta-
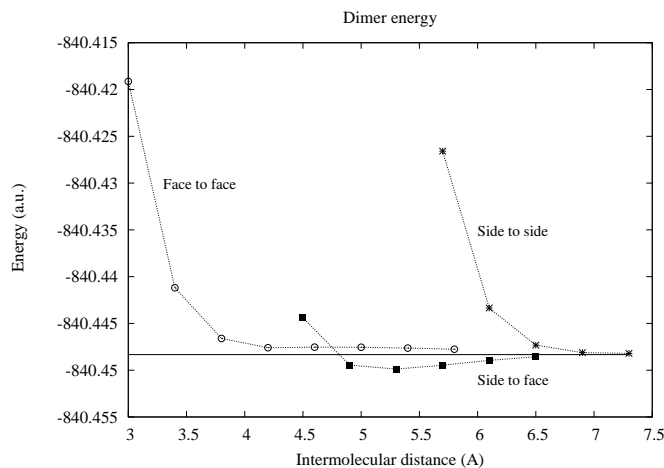
Figure 4.4: Benzoic acid dimer energy (a. u.) in different orientations.

bilizing interaction and yields an adsorption energy per molecule more negative than that of a single benzoic acid. In all the other arrangements the steric interactions prevail, resulting in less favorable adsorption energies. On the basis of these results, the most favored structure for a perfect monolayer of benzoic acid on oxidized GaAs is formed by lines of molecules alternately bound in BB and BC modes on adjacent platforms, as depicted in Figure 4.7; only one of such lines can be found in correspondence of each surface trench.

In conclusion, the $Ga_{20}As_{16}O_4H_{32}$ and $Ga_{108}As_{85}O_{24}H_{109}$ clusters have been used to investigate the preferred arrangements of adducts formed by one or more benzoic acid molecules adsorbed on the oxidized surface, providing very useful insights about the structure of "perfect" organic layers.

Eight possible arrangements of a single benzoic acid molecule on one of the "platforms" existing on the GaAs surface were examined, both computing their relative energy and comparing their vibrational frequencies to experimental spectra, to select the two most likely structures. Using these structures on a larger cluster (containing several platforms arranged in two parallel lines), we found the only relative orientation displaying a favorable intermolecular interaction, leading to the most likely arrangement for a perfect layer.

Figure 4.5: Benzoic acid adsorbed on the large model of the oxidized surface, namely the $Ga_{108}As_{85}O_{24}H_{109}$.

4.2 Dicarboxylic Acids on GaAs(001) Oxidized Surface.

We have modeled the GaAs(001) surface covered by a monolayer of substituted dicarboxylic acids (dC-X, with X = CF_3, CN, H, CH_3, OCH_3 indicating the varying substituent, see Figure 4.8). This system has been widely studied and its electrical behavior in SC/molecule/metal junctions is well characterized[118,131,133,137]: the current/potential curves for such devices are strongly dependent on the acid substituent,[138] the electron-withdrawing groups inducing higher currents at the same potential. Another measured quantity is the contact potential difference between the modified semiconductor surface and a metal surface[132] (in this measure the two parts are connected electrically, but not spatially): even in this case, the potential difference depends on the organic substituent markedly.

The molecular layer modifies the GaAs surface work function, which in turn affects the device properties.[139] In a n-type semiconductor, the work function is defined as $\phi = \chi + BB + \xi^n$, where χ is the electron affinity (EA), that is the difference between the energy of a free electron very close to the surface (the
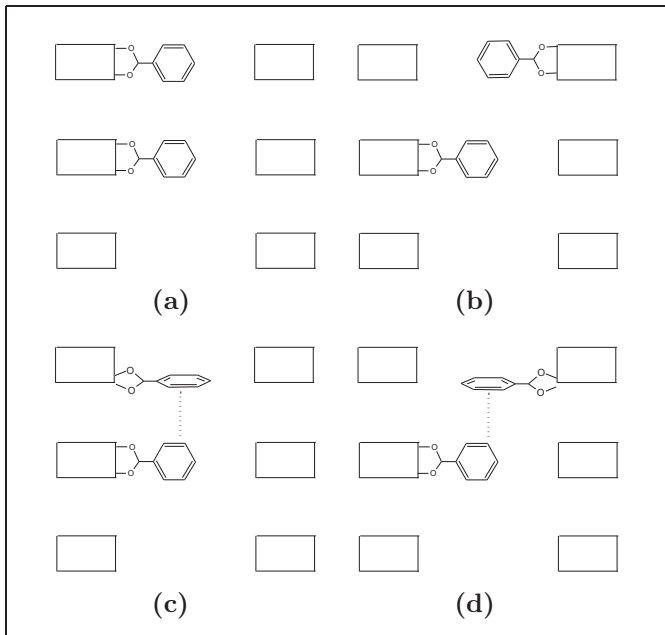
Figure 4.6: Schematic picture of two adsorbed molecules

"vacuum level") and the bottom of the SC conduction band, BB (band bending) is the difference between the band energy on the surface and in the bulk (due to localized electronic states on the surface), and ξ^n is the difference between the SC Fermi level and the bottom of the conduction band. These quantities are illustrated in Figure 4.10. Note that all the energies are taken in absolute values. When a molecular layer is adsorbed on the surface, both the EA and the band bending are modified: measuring the contact potential difference under strong illumination,[113] however, the BB effect can be eliminated, isolating the EA change ($\Delta\chi$).

The $\Delta\chi$ observed upon adsorption of dC-X monolayers on the GaAs surface are often interpreted with a simple model,[110,132] in which the molecules are assimilated to dipole moments (forming an average angle θ with the normal to the surface). A dipole layer is always present also in free surfaces: for instance, in n-type SC the electronic charge concentrates in the surface states, leaving the positive countercharge in the underlying solid (see Figure 4.11-a). The adsorbed molecular layer can be seen as an additional dipole layer (Figure 4.11-b): when the dipoles are oriented with the positive head towards the surface, the electron

Adduct structure	E_{ads} per adsorbed molecule
one molecule (BB mode)	0.0
one molecule (BC mode)	0.5
two molecules (a)	+7.5 (+2.0†)
two molecules (b)	+2.5
two molecules (c)	-4.5
two molecules (d)	+5.0

$\dagger$: as in (a) with an empty platform between the two adsorbed molecules.

Table 4.2: Relative adsorption energy (kcal/mol) for one and two benzoic acid molecules on the $Ga_{108}As_{85}O_{24}H_{109}$ cluster: see Figure 4.6 for the various arrangements.

transfer from the vacuum state to the SC conduction band is favored, that is $\Delta\chi > 0$.

If μ is the absolute value of the dipole associated to one dC-X molecule, the expected EA change is (in atomic units):[110]

$$\Delta\chi = \frac{N\mu\cos(\theta)}{\epsilon} \tag{4.1}$$

where N is the surface density of adsorbed molecules and ϵ is the dielectric constant of the layer. In this model, the relevant microscopic quantities are the molecular dipole and the average orientation on the surface (of course, as far as trends in homogeneous series are searched for, one can assume that the orientation is constant to a good extent). Indeed, previous theoretical studies concentrated on the calculation of dipole moments, mostly with semiempirical techniques,[132] even if some ab initio treatments[119] have appeared also: for the dC-X series, good correlations were found between the computed dipoles and the observed $\Delta\chi$ values.

In the following Sections the geometrical structure of the of the dC-X/GaAs interface will be modeled. The molecular orbitals before and after the adsorption process will be considered, focusing on the energy of the lowest unoccupied molecular orbital (LUMO), that is the quantity more directly related to the electron affinity from the chemical point of view.
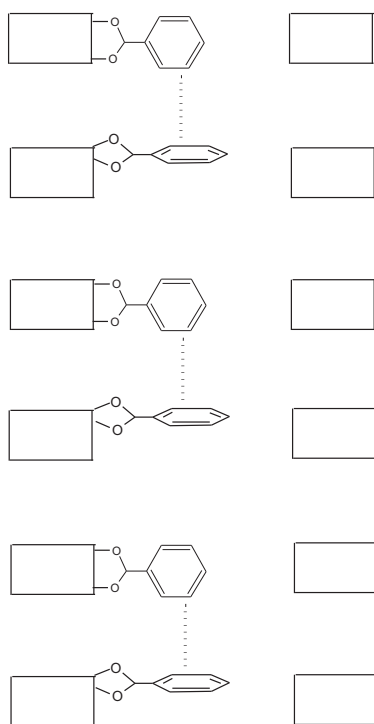
Figure 4.7: Minimum energy arrangement for a layer of benzoic acid on oxidized GaAs.

4.2.1 The Organic/GaAs Interface Model

First the geometry of the five substituted dicarboxylic acids (dC-X, with X = CF$_3$, CN, H, CH$_3$, OCH$_3$, see Figure 4.8) was optimized at the PBE1PBE/6-31+G(d,p) level. The five stable structures were then adsorbed on the Ga$_{20}$As$_{16}$O$_4$H$_{32}$ cluster (see Section 3.2.2).

The geometry of the adducts was optimized with PBE1PBE and the mixed basis set (LANL2DZ on Ga and As, 6-31G on all the other atoms). The structure of the dC-H adduct is shown in Figure 4.9; the other substituents have a little effect on the geometry: in particular, the position of the arms is similar in all the systems. We find that the oxide layer on top of the cluster is markedly more basic than the organic oxygens, confirming previous observations: all our optimizations started with the undissociated acids, but ended with the acidic hydrogens transferred to the oxide, forming two hydroxylic groups still bound to the surface. In all the adducts each carboxylate moiety anchors the cluster surface in a bidentate bridging coordination. The structure is further stabilized by an H-bond between one

X = CF₃,CN,H,CH₃,OCH₃
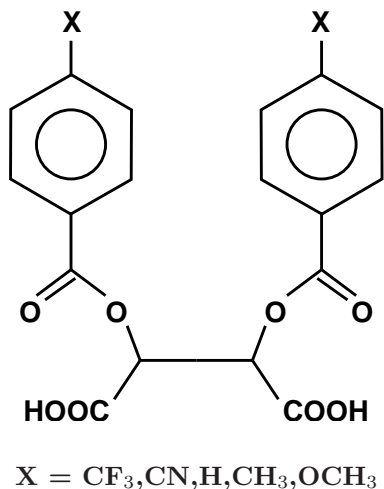
Figure 4.8: Lewis structure of the substi-
tuted dicarboxylic acid.
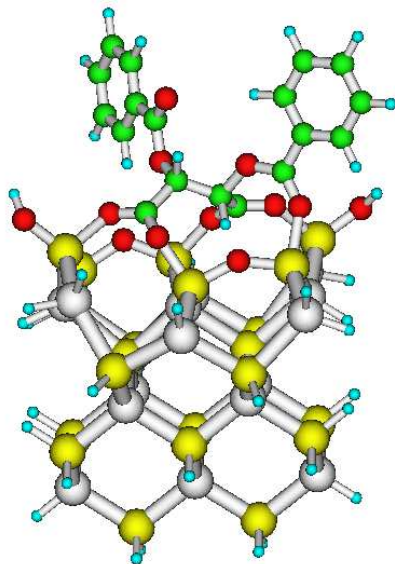
Figure 4.9: Optimized structure of the
dC-H adduct.

of the benzene hydrogens and the carbonylic oxygen not bound to the surface.
The adduct is very stable (for instance, the ΔH of formation with respect to
the separate partners for dC-CF₃/GaAs is -139 kcal/mol at this computational
level).
A two-sites adsorption mechanism had already been postulated for dC-X's on
GaAs,[120,140] with both the acid terminations involved in bridging coordination
bonds. In alternative to the present structure, the two acid moieties could bind
to different "islands" of oxidized Ga along the same line, or crossing the trench
between parallel lines. However, the adduct structure illustrated in Figure 4.9
is most likely (though there are no direct experimental evidences), since the dis-
tance between the dC-X acid groups in the free molecules is very close to the
distance between the two couples of Ga atoms actually involved in the bonding.
On the contrary, the distance between successive islands and the distance across
the trench are too large for such an effective multiple bond.

In conclusion, the structure of the dC-X/GaAs adducts was optimized for the first
time at the ab initio level: the acidic hydrogens are transferred to the inorganic
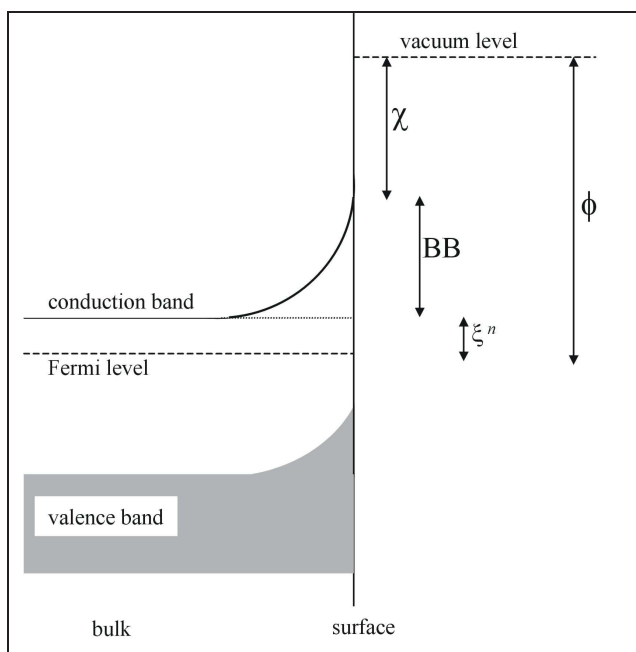
Figure 4.10: Contributions to the SC work function.

oxide layer, and a strong molecule/cluster binding is found, involving five organic oxygens and Ga atoms; the dC-X geometry is strongly distorted upon adsorption, and the molecule body forms an angle of $30 \div 50°$, according to the substituent, with the normal to the surface.

4.2.2 Interface Properties vs. the Observed Electrical Behavior

As previously said, in order to understand the changes in the semiconductor surface electron affinity, the organic monolayers are often depicted as a collection of electric dipoles adsorbed on the surface. The electric dipoles of the five free molecules were computed with PBE1PBE/6-31G+(d,p), with the results listed in Table 4.3; the correlation with $\Delta\chi$ is illustrated in Figure 4.12.

Electron-donating substituents, as $-H$, $-CH_3$ and $-OCH_3$, induce a molecular dipole with the negative head pointing towards the acid groups (i. e. the side of

(a)   **(b)**
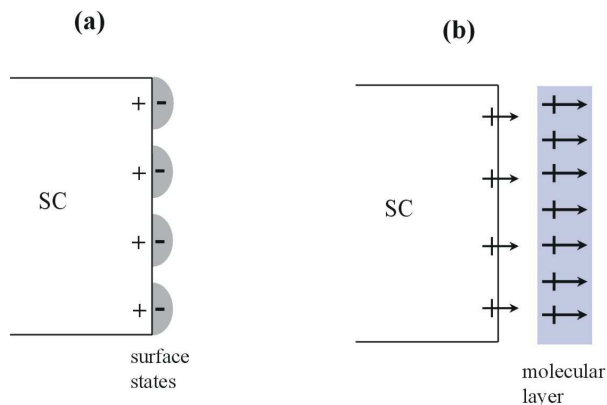
Figure 4.11: Dipole layer due to surface states (a), and to the adsorbed molecular layer (b).

the molecule which will be used to bind to the surface). As discussed above, this corresponds to a negative dipole layer, which is expected to decrease the surface electron affinity ($\Delta\chi < 0$). The opposite is true for the electron-withdrawing substituents, i. e. $-CN$ and $-CF_3$.

The geometry of the adsorbate is quite distorted in the adduct model, being the two arms closer than in the free molecules, and one of them rotated in order to form the intramolecular H-bond. Due to this geometry distortion and to the electronic interaction with the cluster atoms, it is questionable whether the dipole moments computed for the free molecules can be used to explain the adduct properties. The distortion effects can be evaluated by recomputing the dC-X dipoles at the same geometry as in the adducts (with the two acidic hydrogens bound to the corresponding carboxylic oxygens). The norms of the corresponding dipoles are collected in Table 4.3, and compared with those of the free molecules. The dipoles are quite affected by the molecular distortion but the signs and the trend agree: actually, the correlations (namely R^2) between the observed ΔEA and the molecular dipoles computed on the free molecular structure and on the adsorbed structure are very similar (0.97 and 0.96, respectively).

To include also the electronic effects, we have to compute the "molecular" dipole once the acid is adsorbed on the cluster: of course there is no unique definition for this quantity, nevertheless a reasonable approximation can be obtained by means of some localization techniques. We used localized atomic charges according to Hirshfeld's scheme[141], which is more reliable than the simple Mulliken approach, but still much faster than Bader[142] analysis.

Substituent	Dipole norm†(D)			$\Delta\chi$[132]
	Free structure	Adsorbed Structure	Adduct Structure	(eV)
CH_3	(-) 6.23	(-) 4.61	(-) 2.44	-0.25
OCH_3	(-) 6.11	(-) 4.90	(-) 2.41	-0.24
H	(-) 5.24	(-) 3.80	(-) 2.47	-0.23
CN	(+) 3.19	(+) 4.36	(+) 2.57	0.16
CF_3	(+) 1.52	(+) 2.95	(+) 2.58	0.14
R^2	0.96	0.97	0.93	

$\dagger$: Conventionally positive if the positive head points towards the acid group.

Table 4.3: Substituted dicarboxylic acid molecular dipoles (norm) along with the measured changes in electron affinity of covered GaAs surfaces. Reported values refer to the free molecular geometry (second column from the left), adsorbed geometry (third column) and adduct geometry (forth column).
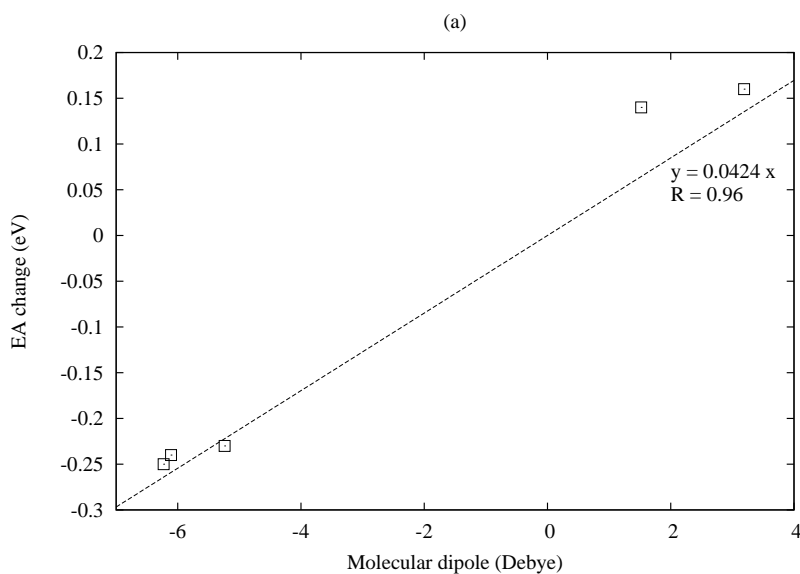
Figure 4.12: dC-X molecular dipoles vs. the observed changes in modified GaAs surface electron affinity.

Hirshfeld atomic charges were computed at the PBE1PBE/6-31G level (thus using the all-electron basis set for all the atoms), for the oxidized GaAs cluster and for the five adducts, at the geometries previously optimized. Different layers were defined: the "core", formed by the Ga and As atoms of the first five layers, counting from bottom, the "surface", formed by the two top layers of Ga and As, and the "top", containing the four oxygen atoms in the bare cluster and the oxygens plus the adsorbed molecule in each adduct. In all cases, the hydrogens were included in the same layer as the heavy atoms they are bonded to; in each layer the "center of charge" was defined as the average of the atomic positions in the layer weighted by the corresponding charges. The atomic charges summed up in each layer are listed in Table 4.4.

In all cases there is a clear charge separation: the surface layer provides elec-

System	Top layer charge[a]	Surface layer charge	Core layer charge
free cluster	-1.74	2.79	-1.04
dC-CH$_3$	-0.91 (0.14)	1.34	-0.43
dC-OCH$_3$	-0.90 (0.15)	1.34	-0.43
dC-H	-0.92 (0.12)	1.36	-0.44
dC-CN	-0.96 (0.07)	1.37	-0.40
dC-CF$_3$	-0.97 (0.07)	1.37	-0.40

(a) Oxide layer (4 O's) in the free cluster, oxide layer + molecule in the adducts: in parentheses the charge on the molecular arms.

Table 4.4: Layer charges (a. u.) computed at the PBE1PBE/6-31G.

tronic charge to the top and to the core, resulting positive. Interestingly, in the free cluster the surface is markedly more positive than in the presence of the adsorbed molecules: the dC-X's transfer an amount of electronic charge to the oxide layer, and the oxygens are in general less eager to draw charge from the underlying Ga atoms. As a consequence, the molecular arms become slightly positive, even if the effect is understandably smaller for electron-withdrawing X's: this is an indication that the use of the gas phase molecular dipoles could be misleading. As a matter of fact, if a "molecular" dipole could be exactly defined in the adducts, it would have a negative sign (i. e. with the positive head far from the binding site) in all the cases, though the measured $\Delta\chi$ has a different sign for some substituents (see Table 4.3).

On the other hand, the data collected in Table 4.4 seem to indicate that the charge double layer is smaller when the surface is covered by dC-X's molecules than in the simple oxidized surface. We can try to express this physical quantity in terms of surface dipoles by concentrating the oxygen and dC-X charge in

the top layer charge center, and placing the same charge with the opposite sign in the surface layer charge center (i. e. concentrating here all the surface and core charge, leaving the "bulk" of the semiconductor neutral). In this model, the surface dipole is 3.01 D in the free (oxidized) cluster, and 4.22, 4.26, 4.08, 4.33, 4.47 D with adsorbed molecules (the order of the substituents is the same as in Table 4.4, and the dipole sign is positive according to the convention previously explained). If we consider the free oxidized cluster as a model for the bare semiconductor surface (without molecules attached), the dipoles reported above do not correlate at all with $\Delta\chi$, since they are systematically larger than 3.01 D, while the measured electron affinity change has different sign according to the substituent. Actually, this is due to displacement of the center of charge in the adduct structure with respect to the free cluster: placing the top charge in the same point as in the free cluster, the dipoles with attached dC-X become lower than the free cluster dipole (see Table 4.3). In this case the correlation with $\Delta\chi$ improves ($R^2 = 0.93$), but remaining worse than that obtained with isolated molecule dipoles: recall that this last fitting has been obtained omitting the "zero" point, i. e. the result for the free cluster.

In order to model the molecular effects from a more chemical viewpoint, we computed the LUMO energies for the free oxidized cluster and for the adducts, since this is the quantity most directly related to the electron affinity at this theoretical level. It is worth noting that in the free cluster the LUMO is located on the oxide layer, while in all the adducts the LUMO and most low-lying unoccupied orbitals concentrate on the molecular moiety, so that their energy is affected by the chemical nature of the organic substituents significantly. On the contrary, the highest occupied orbital always lies in the inorganic moiety: see Figure 4.13 for an illustration of the HOMO and LUMO orbitals in the bare cluster and in the dC-H adduct. The LUMO energies are reported in Figure 4.14, along with the corresponding HOMO energies, for comparison: as expected, the HOMO levels are much less dependent on the organic substituents, and in all the adducts their energies are slightly less negative than in the bare cluster. The LUMO energies, on the other hand, depend on the adsorbed molecule markedly, and they show the expected trend with the substituent electronegativity, being more negative with electron withdrawing substituents which leave the rest of the molecule less rich in electron density and thus more eager to accept the incoming charge. As illustrated in Figure 4.15, the correlation of the measured $\Delta\chi$ with the adduct LUMO energies (referred to the bare cluster LUMO level) is quite good ($R^2 = 0.96$)

(a)

(b)
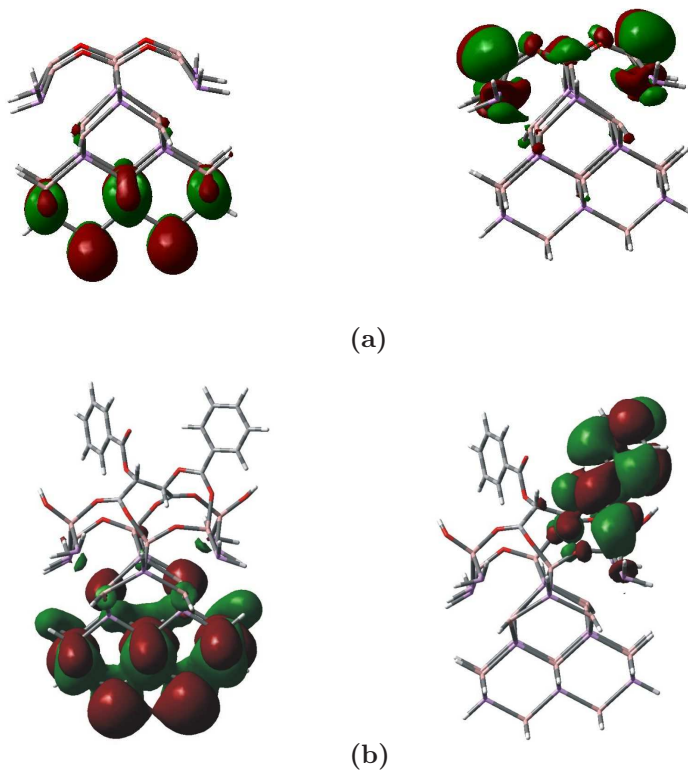
Figure 4.13: HOMO and LUMO orbitals for (a) the bare cluster, and (b) the dC-H/GaAs adduct.

In conclusion, a good correlation is found between the electric dipole moments of isolated dC-X and the measured $\Delta\chi$ of the modified surfaces. Besides, due to the geometry distortion experienced by the adsorbed molecules, it seems unlikely that the isolated system dipoles are directly related to the adduct properties. After the adsorption, it is possible to model the electric double layer at the molecule/semiconductor interface by means of localization techniques (in our case, Hirshfeld's charges were used): the results are not completely satisfactory, since in all the adducts the double layer is found to be smaller than in the free (oxidized) surface, while the observed $\Delta\chi$ has different signs for different substituents. However, the *relative* trend of dC-X/GaAs surface charge separation correlates quite well with the electron affinity changes.
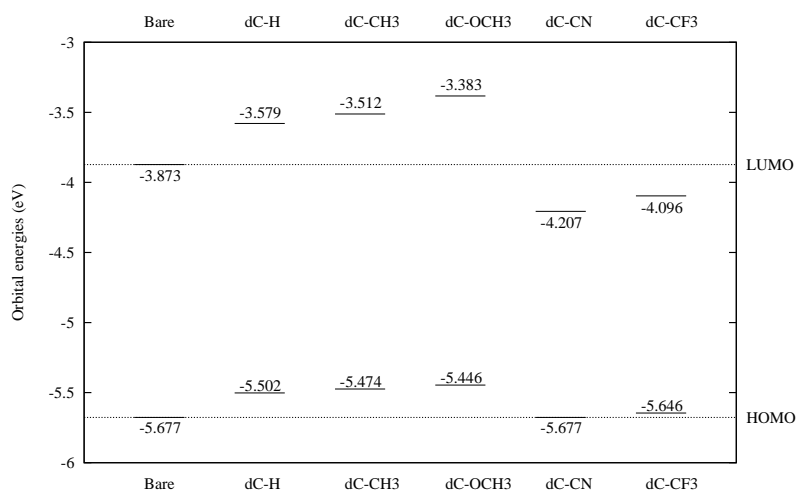
Figure 4.14: HOMO and LUMO levels for the bare oxidized GaAs cluster and the adducts.
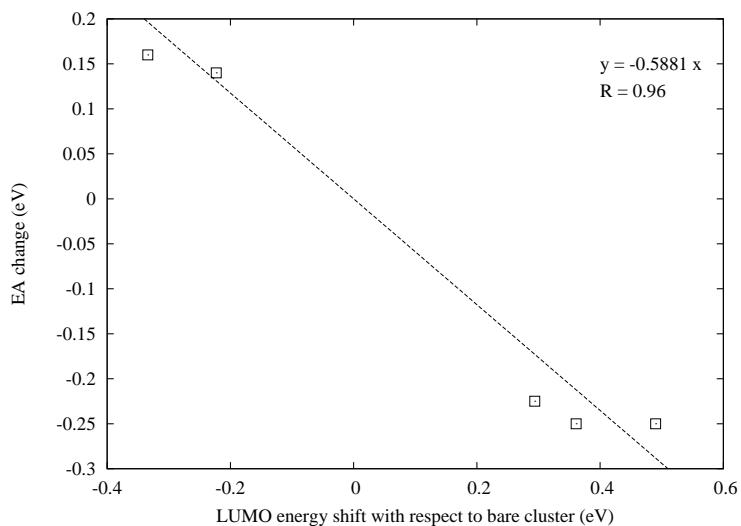
Figure 4.15: Observed changes in modified GaAs surface electron affinity vs. the GaAs/dC-X adduct LUMO energy (referred to the bare cluster LUMO).

A better correlation is found by computing the molecular orbital energies of the adducts: the LUMO orbital concentrates on the oxide layer in the free cluster, and on the molecular arms in the adducts (while the HOMO is always located in the cluster core), and the relative energies follow the same trend of the experimental EA's, with a linear coefficient $R^2 = 0.96$. From this viewpoint, the good trend of isolated dipole moments with $\Delta\chi$ can be better explained with the strong correlation between the dipole and the LUMO energy, being these quantities both strongly dependent on the electronegativity of the acid substituents.

Organic molecules on TiO$_2$

The remarkably steep increase in the number of papers dealing with titanium dioxide in the last ten years[143] can be mainly ascribed to its wide range of technological applications in heterogeneous photocatalysis[144,145], photoelectrochemistry[63,146] and nanophotonics[147,148], based on peculiar effects/phenomena occurring at the surface of this material when targeted molecules are adsorbed. In particular, the adsorption of carboxylic acids on its surfaces has been the subject of intense experimental and theoretical research related to the investigation of the mechanism of photodegradation of organic pollutants[149,150], fluorination[151], and, more recently, to the use of organic dyes as light collectors in dye-sensitized solar cells[63,146,152].

Since the research work lead by Prof. Schiavello in 1988 on the photodecomposition of CH$_3$COOH on semiconductor and insulator oxides[153−155], significant effort has been devoted in the field of heterogeneous photocatalysis to the characterization of the interaction of different classes of carboxylic acids with TiO$_2$ surfaces[156−160].

In dye sensitized solar cells, on the other hand, it has been shown that the organic dye is usually anchored to the TiO$_2$ surface by means of carboxylic groups and the investigation of the nature of such interaction could be relevant also for improvements in this type of technology. In this respect, for both photocatalytic applications and solar cell engineering, it is of interest to gather all the relevant

informations in order to design novel modified TiO$_2$ materials.

5.1   Adsorption of Acetic Acid on Anatase (010)

Among the three main TiO$_2$ polymorphs, i.e. brookite, rutile and anatase, the latter two are the most relevant from a technological and scientific point of view. Adsorption of carboxylic acids on rutile polymorph, the most stable one, was extensively characterized by means of different experimental techniques[161 − 167] and ab-initio calculations[168,169]; recently increasing attention has been devoted to anatase both from experimental[170,171] and theoretical[169,172] point of view, due to the significantly higher activity as photocatalyst. A quite accurate description of anatase surfaces and adsorption of different carboxylic acids was achieved by means of single crystal experiments[149,170,171,173]. Coupled electron microscopy and infrared spectroscopy studies on the TiO$_2$ single crystal[174,175] revealed that the anatase (010) and (001) surfaces are mainly exposed: actually the most abundant and extended faces of the hexagonal crystals have been identified as (010), while the lateral ones can be ascribed to (001) and, to a minor extent, (101) surfaces. Differently, among all the lattice planes exposed in nanostructured anatase, the predominant one consists of (101) surface.
We have thus decided to start modeling the adsorption of acetic acid, intended as a model carboxylic adsorbate, on the (010) surface, aiming to provide some insight into different possible types and structures of adsorbed species.
The first theoretical calculations of the energetics of different configurations for adsorbed carboxylic species have been performed by Selloni and coworkers[172] for formic acid on (101) surface and they indicate a larger stability of molecular hydrogen bonded species. In this respect, assuming a similar behavior of formic and acetic acid, it can be interesting to compare such results with our calculations on (010) surface. Other theoretical calculations of small molecules on the same (010) surface have been performed by Bredow and coworkers[176] within the MSINDO approach.
On the experimental side, FTIR studies of acetic acid adsorption on TiO$_2$[177] suggest that acetic acid is adsorbed in bidentate chelating way, with both Oxygen atoms coordinated to the same Ti cation. More recent experiments has pictured a more complicate situation, because of the presence of broad and multicomponent bands which are probably due to different adsorption configurations.

In the following Section, we model the anatase single crystal surface by mean of opportunely terminated cluster. The CH$_3$COOH/TiO$_2$ interface is investigated

by comparing the measured IR spectra with the vibrational frequencies computed on a series of assumed adduct geometries.
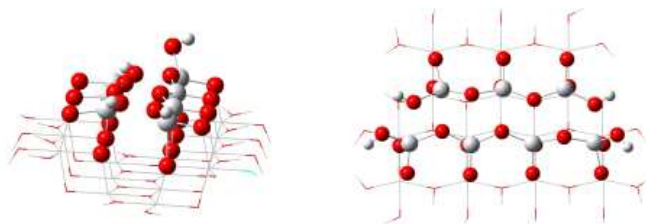
Figure 5.1: $Ti_{21}O_{55}H_{26}$ cluster (left: side view, right: top view) used to model the (010) surface of anatase single crystal.

5.1.1 The Cluster Model

The anatase single crystal surface was modeled with a $Ti_{21}O_{55}H_{26}$ saturated cluster (Figure 5.1), made of three atomic layers: the upper layer (the surface) corresponds to the (010) arrangement and is large enough to allow all possible linkages of acetic acid or acetate without involving edge atoms; the dangling bonds were saturated by H atoms and OH groups to obtain a stoichiometric cluster.

The isolated cluster was optimized both at MSINDO and at PBE1PBE levels: in the PBE1PBE calculation the LANL2MB basis set (along with the corresponding effective core potentials) was used for the Ti atoms, and the 6-31G for O and H atoms. Only the atoms belonging to the top layer were allowed to move during geometry optimizations; to minimize the border effects due to the cluster finite size, the distances between the surface edge oxygens and the underlying Ti atoms were also kept fixed to the bulk values.

For most of the geometric surface features the differences between the stable MSINDO and PBE1PBE structures resulted negligible. Furthermore, the agreement with periodic calculations performed within a CPMD scheme (Atte Sillanpaa, private communication) is quite satisfactory: for instance, the minimum Ti-Ti distance is 3.33 Å in our model and 3.19 Å in the periodic system, while the minimum Ti-O distance across the central rows is 2.13 Å and 2.17 Å, respectively, confirming the assumption that the border effects can be neglected and

that our cluster provides a quite satisfactory representation of the (010) surface.
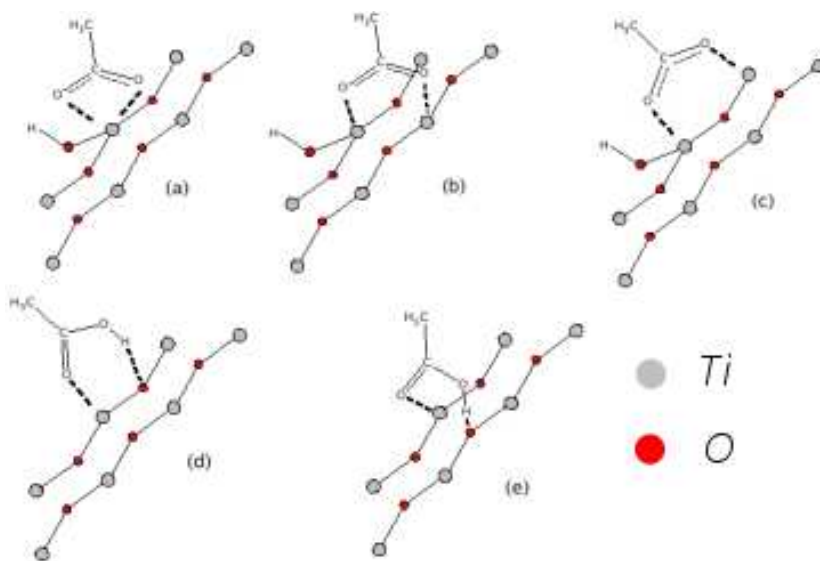
Figure 5.2: Five possible configurations for the adduct of dissociated(*a-c*) and undissociated(*d-e*) acetic acid on TiO$_2$ (010) surface.

5.1.2   The Adsorption Modes and IR Spectra.

In Figure 5.2 the different adduct geometries resulting from both a dissociative and un-dissociative adsorption process are sketched: from (*a*) to (*c*) the ionic species adsorbed as bidentate chelating (*a*) or bridging, with both Ti atoms on different rows (*b*) or on the same row (*c*) are shown; (*d*) and (*e*) correspond to undissociatively adsorbed adducts, with the C=O group anchored on a Ti atom and the hydroxyl group H-bonded to a proximal O atom on the same (*d*) or on a different row (*e*). Each of these adducts gives rise to a specific vibrational pattern, and from the comparison of the computed and experimental frequencies we can provide a reasonable interpretation of the experimental spectra.

The geometry optimizations for the CH$_3$COOH/cluster adducts, and the calcula-

tion of the vibrational frequencies were performed within the ONIOM scheme, to keep the computational costs manageable: a small portion of the cluster surface (shown with balls and sticks in Figure 5.1), together with the organic adsorbate, was taken as high level region. In the PBE1PBE calculations, the basis set was 6-31G for C, O and H atoms, and LANL2MB (along with the corresponding effective core potentials) for Ti atoms.

In order to validate our computational approach providing a rough estimate of the associated error, the vibrational frequencies for CH_3COOH and CH_3COONa were computed with the same functional and basis set (PBE1PBE/6-31G) used for the adducts, and compared with the experimental ones.

From Tables 5.1 and 5.2 we see that the agreement is good for most of the frequencies considered, especially for those involving the greatest contribution of the carbonyl and carboxyl groups. The only significant discrepancy can be found in the assignment of the symmetric O-C-O stretching of CH_3COONa (Table 5.2): in our work it corresponds to a frequency of $1457 cm^{-1}$ and in Ref. [178] to a lower frequency ($1424 cm^{-1}$), while the opposite is true for the CH_3 bending. To check the validity of our assignment of the symmetric O-C-O stretching, calculations with deuterated sodium acetate were performed, whose frequency results only slightly shifted, while the CH_3 bending is remarkably shifted to the expected lower frequency values.

PBE1PBE/6-31G	Assignment[†]	exp.[††]
1198	νC-O($+\omega CH_3+\delta$C-O-H)	1185
1388	νC-O($+\omega CH_3+\delta$C-O-H)	1296
1456	$\delta CH_3(+\nu$C-C)	1429
1513	σCH_3	
1518	τCH_3	1517
1794	ν C=O($+\delta$C-O-H$+\sigma CH_3+\delta$C-C-O)	1795

(†) Symbols: ν stretching, δ bending, ω wagging, τ twisting, σ scissoring. The frequencies characterized by the stretching modes of the carboxylic group as dominant components are indicated in bold. (††) Capecchi *et al.* (in press.)

Table 5.1: Comparison between computed and measured CH_3COOH IR frequencies (cm^{-1}).

In Table 5.3 the computed frequencies for the different adduct configurations are summarized. The assignment of the individual frequencies is complicated by the

PBE1PBE/6-31G	Assignment†	exp.††	Assignment
1422	δCH$_3$($+\nu_{sym}$O-C-O)	1424	ν_{sym}O-C-O
1457	ν_{sym}O-C-O(νC-C $+ \delta$CH$_3$)	1447	δC
1500	τCH$_3$($+ \nu_{asym}$O-C-O)		
1524	σCH$_3$($+ \nu_{asym}$O-C-O)		
1578	ν_{asym}O-C-O(τCH$_3 + \delta$C-C-O)	1584	ν_{asym}O-C-O

($\dagger$) See Table 5.1 for labeling.
($\dagger\dagger$) Kakihana *et al.* (Ref. [178])

Table 5.2: Comparison between computed (PBE1PBE/6-31G) and measured CH3COONa IR frequencies (cm^{-1}).

strong coupling between the vibrational modes corresponding to the deformation of several bonds: therefore we indicate the dominant component, reporting the others between parentheses. Furthermore, because of the slightly asymmetric nature of the COO- group, which appears quite evident from the values of the C-O distances in the chelating (1.28 and 1.31Å) and bridging (1.28 and 1.30 Å) configurations, we do not see a clear symmetric O-C-O stretching, while we distinguish individual C-O stretching, as if they were somehow decoupled. On the other hand, almost-symmetric stretching can be located in the computed spectra, close to the frequency of 1457 cm^{-1} assigned to the symmetric mode in the calculation of CH$_3$COONa vibrations.

Under this assumption, the symmetric/asymmetric frequency difference can be estimated for each adduct. The splittings for the chelating (Figure 5.2,*a*) and the bridging structure involving Ti atoms on different rows (Figure 5.2,*b*) turn out to be very similar to each other, while the splitting is larger for the bridge with Ti atoms on the same row (Figure 5.2,*c*). This can be explained examining carefully the C-O and Ti-O distances of the two bridging species: when the Ti atoms are on different rows, such distances are very similar (the C-O bonds differ by 0.02 and the Ti-O by 0.05 Å) indicating a higher degree of symmetry than in the previous case, where these values are quite different (the C-O bonds differ by 0.06 Å and the Ti-O by 0.13 Å).

For one of the molecular H-bonded species (Figure 5.2,*d*) the C-O distances differ by about 0.04 Å and the splitting is of 174 cm^{-1}, while for the other (Figure 5.2,*e*) the difference is lower (0.02 Å) and the splitting decreases accordingly to a value of 158 cm^{-1}. In the H-bonded molecular adducts, we have then a higher frequency mode corresponding to a C=O stretching, which is only weakly coupled with the C-O one but strongly coupled with a C-O-H bending. The frequency associated to such a combination of vibrational modes is higher for the structure

Exp.[†]	CH3COO-			CH3COOH	
	(a)	(b)	(c)	(d)	(e)
1364				**1382**	**1375**
1416	1437	1431	**1402**		
1454	**1464**	**1450**	1453	1453	1450
1492	1505	1499	1495	1483	1489
1525	1513	1518	1512	1510	1513
1530					**1533**
1593	**1570**	**1552**	**1622**	**1554**	**1583**
1680				**1673**	

(†) Capecchi *et al.*, *in press*

Table 5.3: Comparison between computed and measured IR frequencies (cm^{-1}) for the dissociated and undissociated adducts (the letters in parenthesis identify the adduct as in Figure 5.2). The frequencies characterized by the stretching modes of the carboxylic group as dominant components are indicated in bold.

(d), i.e. 1673 cm^{-1}, while for specie (e) it is only 1583 cm^{-1}. Such a frequency difference could be explained considering that the first adduct is less symmetric and the C=O frequency is therefore closer to that of an isolated CH3COOH while the second structure is more similar to a partially ionized acetic acid. This hypothesis is further confirmed by the observation that O-H distance in the molecule and H$\cdots$O distance between the proton and the surface Oxygen are more similar (1.09 and 1.36 Å) for the latter structure (e) than in the other H-bonded adduct (1.03 and 1.56 Å), indicating a larger propensity to a possible protonation of the adjacent surface Oxygen for specie (e).

Since the computed frequencies of all possible adducts are compatible with the vibrational broad bands characterizing the IR spectra, an intrinsic complexity of the adsorption on the (010) surface arises, even though in our calculations we do not account for the presence of minority surfaces and peculiar surface features, such as defects, edges or steps.

The experimental splitting between the symmetric and antisymmetric carboxylate modes is known to be indicative of the degree of coordination bonding between the adsorbed carboxylate and the substrate atoms: if such a splitting is less than the one observed for the free carboxylate, the bonding is covalent. By comparing the computed frequencies with the IR experiment, we can associate the lowest experimental splitting (70-80 cm^{-1}), to the bidentate chelating and

bridging ionic species, even though their computed splittings appear to be over-
estimated with respect to the experiment. The experimental larger splitting is
difficult to identify, due to the complexity and broadness of the experimental
bands.

In conclusion, from this combined theoretical and IR investigation we can state
that already taking into account just the (010) surface, namely the more abundant
one, a number of different species are compatible with the observed vibrational
pattern. In particular, the observed lowering of the splitting between almost-
symmetric and asymmetric O-C-O stretching, is consistent with the postulated
presence of both bidentate chelating (Figure 5.2,a) and bridging (Figure 5.2,b)
adsorbates.

5.2   Ru-based Dye Sensitizer on Anatase(101)

Nanostructured anatase particles have attracted widespread attention due to
their use in photoelectrochemical systems, such as Graetzel cell[63,146,152]. Light
absorption by bare TiO$_2$ is, however, low in the visible region, being the funda-
mental band gap of about 3.2 eV. This limitation has been overcome by attaching
organic or organometallic compounds that absorb in the visible region and pass
the excitation to the conduction band of the supporting metal-oxide[63,179].
Nanostructured TiO_2 sensitized by so-called N3 dyes (Ru(4,4'-dicarboxy-2,2'-
bipyridine)$_2$(NCS)$_2$), is probably the most well-known example of a dye-sensitized
nanocrystalline metal oxide semiconductor[179−182]. More recently, a novel se-
ries of Ruthenium-based dyes (cis-bis(4,7-dicarboxy-1,10-phenanthroline) dithio-
cyanato ruthenium(II), referred to as Ru(Ph)) were studied experimentally[183].

The photophysical properties of the Ru-based dye sensitized solar cells strongly
depend on the nature of the sensitizer-substrate interaction. In this context, the
computational study of such complex systems can provide useful insight into the
structural and electronic properties of the interface. A reliable interface model
must include a portion of substrate suitably shaped to allow large dyes adsorp-
tion and correctly terminated to avoid unphysical finite size effects. Moreover
the model should be computationally feasible, the computational burdens in-
creasing when the solvent effect has to be accounted. This intrinsic complexity
has severely restricted the possibility of quantum chemical calculations on real-
istic model systems.

Small[172,176,184,185] and aromatic molecules, such as benzoic acid, catechol[68,186], bi-isonicotinic acid[187−190] and perylene chromophores[70,191], adsorbed on TiO_2 have been studied at semiempirical and ab-initio level. Persson *et al.* have studied the interface properties of N3 adsorbed on nanostructured TiO_2[70,192] at DFT level. De Angelis *et al.*[69] have investigated the photophysical properties of a TiO_2 nanoparticles sensitized with $[Fe(CN)_6]^{4-}$ complex, highlighting the importance of including the solvent effect for a realistic modeling. In this case the computational expense increases with the dimension of the sensitizer, quickly reaching the computational limit.

The question of what is the anchoring geometry of Ruthenium-based dyes is still under debate. Besides IR structural analysis, very little informations can be obtained from direct experimental observations. From a computational point of view, the high computational costs limit the use of suitably sized nanocluster models: the $Ti_{36}O_{72}$ cluster, adopted by Persson *et al.* allows the quantum description of the interface structure when the molecule is adsorbed via a single anchoring group, discarding more complex binding modes. So far, ab initio calculations on larger cluster are not feasible[70].
Furthermore, the post-SCF computational tools for studying photophysical properties are even more computationally demanding: the electronic structure and photophysical properties have been investigated in vacuum, with the aid of TD-DFT methods, in this case restricting the calculation to the very first absorptions in the far IR region, or by using semiempirical CI-type procedures[68].

In the present work, the structural and electronic properties of the $Ru(Ph)/TiO_2$ interface have been studied. First, the adsorption mode of the Ru(Ph) (Figure 5.3) has been investigated. The use of the computationally less demanding ONIOM-Ti$_5$4 approach (see Section 3.1.2) allows for the first time, to consider different interface geometries. Aiming to perform a Time-Dependent DFT investigation of the photophysical properties of the combined dye/semiconductor system in solution, a small interface model has been drawn out from the stable adduct structure. The simulated and experimental absorption spectra were found in good agreement, that is despite of its minimal size, the interface model reproduces well the photophysical properties of the real dye/TiO_2 system. Finally, the comparison between the computed and experimental absorptions provides useful insight into the mechanism of the charge injection process occurring at the interface.
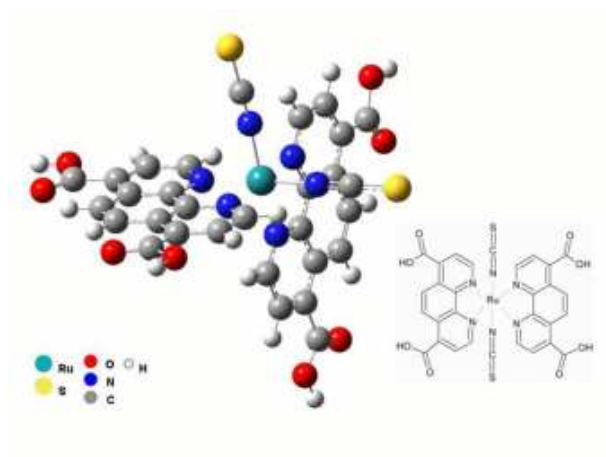
Figure 5.3: Molecular structure of the *cis*-bis (4,7-dicarboxylate-1,10-phenanthroline) dithiocyanato-Ru(II).

5.2.1   The Binding Mode

It is well known that smaller organic acids undergo a strong dissociative adsorption on TiO$_2$, resulting, in most cases, in a bidentate bridging rather than chelating anchoring mode[165,172,185,193]. The same mechanism was assumed in the case of N3. In particular, by combining the experimental data of the dye crystal structure, along with the features of the mainly exposed lattice planes in the anatase nanocrystal, Shklover *et al.*[180] have postulated a possible adsorption mechanism. In their modeling, a carboxylate group anchors one of the surface Ti atoms. Due to high rotational freedom of the so formed combined system, the adsorption process proceeds by anchoring the neighbor Ti atom, leading to a bidentate bridging coordination bond (see Figure 5.4). Alternatively both carboxylate groups of the same ligand might anchor in a monodentate configuration (namely D-TYPE structure in Figure 5.5). The volume occupied by the N3 dye is large enough to postulate the anchoring via two carboxylic groups, coming from two different bypyrimidine ligands, (see E-Type and F-Type in Figure 5.6). In the E-Type binding mode, both carboxyl groups bind in a bridging configuration, while one of them is anchored via a monodentate bond in the F-Type structure. In the latter case the structure might be stabilized by an H-bond interaction with one surface hydroxyl group. In both cases, the remaining two carboxyl groups stay in a protonated form. Nazeeruddin *et al.*[181] have investigated the N3/TiO$_2$

interface with the aid of the ATR-FTIR analysis. According to their results, the N3 adsorbs using two out of four carboxyl groups, the IR data being consistent with a large excess of E-Type and F-type complexes. Similar considerations can be applied to the $Ru(Ph)/TiO_2$ interface, since the two sensitizers have similar structures, and the carboxyl groups display similar acidity.
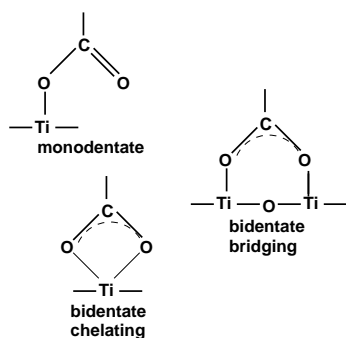
Figure 5.4: The binding modes of a single carboxylate moiety.
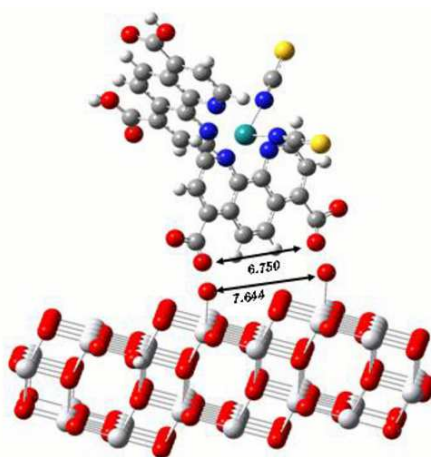
Figure 5.5: The D-Type adsorption mode.

We focus on the E-Type and F-Type geometries. To reduce the computational burden, a step-wise optimization strategy was adopted. First a small molecular cluster, made by the dye and only four (TiO_2) units was considered (see Figure 5.7): the substrate portion was cut out and saturated as described in the Section 3.1.2. This molecular model will be referred to as $Ti_4O_8:Ru(Ph)$.

The E-Type and F-Type molecular models were optimized at B3LYP level, using a basis set constructed as follow: the 6-31g(d,p) basis set was used for all atom types of the first and second period but Sulfur. For the other atom types a LANL2MB basis with the corresponding pseudopotential was used. Moreover an extra set of polarized d functions were added to the Ruthenium and Sulfur. The obtained relaxed models are shown in Figure 5.7.

The main geometrical features of the two stable structures are reported in Table 5.4, and compared with the corresponding average values from a data base of crystal structures of similarly bonded molecular systems[180]. Clearly, the computed values agree with the experimental data.

In the E-Type structure, the two anchoring moieties bind in a bridging configuration even if one of them (namely the $Bridg^2$, see Table 5.4) keeps a partial
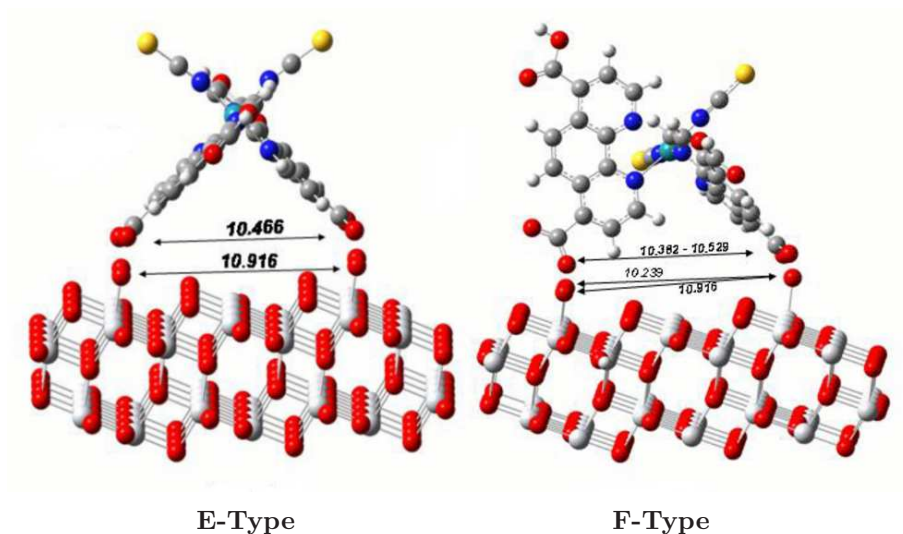
Figure 5.6: The E-Type (left) and the F-Type (right) adsorption modes.

monodentate character: the two C-O bonds are indeed slightly asymmetric (1.30 and 1.27 Åfor the C-O^1 and C-O^2, respectively), at the expense of the corresponding Ti-O^2 bond, which are found to be looser (2.67 Åfor the Bridg^2 to be compared with 2.19 Åin Bridg^1).

A stabilizing H-bond occurring between the non-bonding oxygen of the monodentate carboxylate and the proton on the substrate (see right hand side of Figure 5.7), justifies the found higher stability (0.42 eV) of the F-type stable structure with respect to the E-Type. On the other hand, the adsorbate in the F-Type geometry is strongly tilted. Clearly, in modeling the real system, the eventual interaction between the bent SCN ligand and the surface must be considered.

The relaxed E-Type and F-Type models were then settled onto the Ti$_{54}$O$_{108}$ cluster by superimposing the TiO$_2$ units of the Ti$_4$O$_8$:Ru(Ph) model with the corresponding units on the cluster surface. The obtained adduct cluster was then optimized according to the ONIOM scheme: the Ti$_4$O$_8$:Ru(Ph) portion was treated at B3LYP level (with the same basis set previously used for the optimization) and the remaining portion of the cluster at MSINDO level. We refer to this combined system as Ti$_{54}$O$_{108}$:Ru(Ph).

E-Type   F-Type
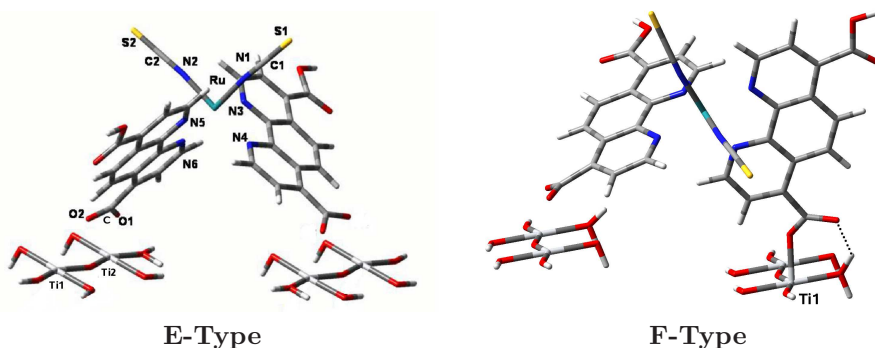
Figure 5.7: The two Ti_4O_8:Ru(Ph) models.

Interestingly no minima in the potential surface was found corresponding to the F-Type bonding mode, the organic adsorbate being characterized by an high degree of rotational freedom: this is actually in agreement with what postulated by Shklover *et al.*[180] on the basis of IR analysis.

A net minima was instead found for the E-Type bonding coordination. It is worth noticing how the structural features of this interface geometry do not change by enlarging the substrate portion: comparing the two optimized E-type geometries (Ti_4O_8:Ru(Ph) and $Ti_{54}O_{108}$:Ru(Ph)) no large structural differences were found.

The calculations suggest that the two adsorbing mechanisms are thermodynamically (but not kinetically) equivalent. This substantial equivalence justifies what was assumed on the basis of experimental IR evidences: the binding coordination depends markedly on preparation of the semiconductor film and on the adsorption conditions[194]. The comparison between the computed and experimental spectra can be useful for the characterization of the adsorbed species obtained from a given experimental procedure.

In Table 5.5 the C-O stretchings for the adsorbed and isolated dye in ethanol are reported. The experimental values, obtained according to the procedure followed by Hara et al.[194], are here compared with the B3LYP values computed on the E-Type and F-Type Ti_4O_8:Ru(Ph) stable geometries, still using the same basis set adopted for the optimizations.

The asymmetric and symmetric C-O stretchings (ν_{asym}^{C-O} and ν_{sym}^{C-O}) indicate the presence of either a free carboxylate moiety or an bidentate anchored carboxylate (in chelating or bridging binding mode). The C=O stretching ($\nu^{C=O}$) suggests the presence of either a carboxylic moiety or a monodentate ester type anchoring.

Geometrical	E-Type		F-Type		
Feature	Bridg.[1]	Bridg.[2]	Bridg.	Mono.	Exp[†]
Ti^1-O^1	2.047	2.097	2.135	1.940	2.03
Ti^2-O^2	2.190	2.670	2.192	- - -	
C -O^1	1.275	1.300	1.292	1.300	1.26
C -O^2	1.261	1.268	1.259	1.243	
Ti^1-C-O^1	118.1	128.7	126.0	127.3	135
Ti^2-C-O^2	128.0	132.7	123.7	- - -	

(†) Reported experimental values are taken as average of 71 fragments Ti-O-C-O-Ti containing octahedral Ti atoms[180]. Fragments crystal structures from the *Cambridge Structural Database*, Release 1997.

Table 5.4: The main geometrical features of the E-Type and F-Type optimized Ti$_4$O$_8$:Ru(Ph) models. For atomic labeling see Figure 5.7

Hara *et al.* have observed that the splitting of 220cm^{-1} between the asymmetric and symmetric C-O stretching (1380 and 1600 cm^{-1}, respectively) suggests the prevalence of the E-Type binding geometry.

The computed $\nu^{C=O}$ stretchings, for the isolated dye, are slightly shifted with

	Experimental		Calculated		
Mode	Isol.^{a}	Ads.^{b}	Isol.	Ads.(E-Type)	Ads.(F-Type)
$\nu^{C=O}$	1713-1715	–	1771-1778	1809-1811[†]	**1678**; 1809-1812[†]
ν^{C-O}_{sym}	–	1380	–	1329-1348	1327-1340
ν^{C-O}_{asym}	–	1600	–	1525,1579,1612	1545-1558,1600

(a) From Ref. [183]; (b) from Ref. [194] (†) C=O stretching of the two not-anchoring carboxyl groups

Table 5.5: IR spectra of the isolated and adsorbed dye, in ethanol. Comparison between the experimental and computed values.

respect to the experimental values, but the band width (of around 7 cm^{-1}) is well reproduced. The $\nu^{C=O}$ of the two not-anchoring carboxyl groups (1809-1811 cm^{-1}) in the E-Type and F-Type geometry are equally shifted towards higher wavelengths, if compared with the same stretching in the free dye.

In the adduct structure, the anchoring groups have a strong carboxylate character, highlighted by the characteristic splitting between the asymmetric and

symmetric C-O stretchings. [1] The computed splittings slightly over-estimate the experimental value, expecially in the case of E-Type geometry. Nevertheless the general agreement between the computed and the experimental splittings indicates that both adducts are compatible with the observed vibrational pattern.
The monodentate carboxylic anchoring group in the F-Type structure displays an ester type bonding, i.e. characterized by a vibration mode (at 1678 cm^{-1}) mainly due to the C=O stretching. This is in good agreement with the corresponding experimental value of 1700 cm^{-1} [194]. Interestingly, no other absorptions are found in this region, in the E-Type computed spectra.

In conclusion, due to the complex anchoring structure, the observed symmetric/asymmetric stretching splitting of the C-O bond is compatible with both adsorption modes (namely, E-Type and F-Type). On the other hand the absence of the characteristic adsorption at $\sim 1700 \text{cm}^{-1}$, satisfactory reproduced by the calculation, might indicate a large excess of E-Type binding species.

5.2.2 The Electronic Structure of the Dye/TiO$_2$ interface

The electronic structure of the combined $Ti_{54}O_{108}$:Ru(Ph) system (from here on we will consider the E-type structure) was calculated at B3LYP:MSINDO level, by using the same basis set used for the optimization, for all the atom types but the Ti atoms, whose chosen basis set was LANL2DZ, with the corresponding pseudo-potential.
An effective Density of States (ONIOM-DOS) was constructed by integrating within the ONIOM fashion the DOS plots of the model and real system, both constructed from the orbital levels lined up with respect to an arbitrary zero-point energy. For the sake of simplicity the HOMO level of the combined system was set to zero. The sensitizer contribution to this DOS (PDOS) have also been extracted using the appropriate orbital coefficients. The upper graph of Figure 5.8 shows the resulting plot, compared with the effective DOS plot of the bare $Ti_{54}O_{108}$ cluster, also computed at B3LYP:MSINDO level. The band structure of the nanoparticle model does not change significantly upon adsorption of the sensitizer.
 The sensitizer contribution (PDOS) to the electronic structure of the sensitized nanoparticle in the region of interest for the photoexcitation processes, is reported

---

[1] As in the case of acetic acid on anatase, the assignement of the symmetric stretching is straightforward while the identification of the asymmetric vibrational frequencies is controvertial.
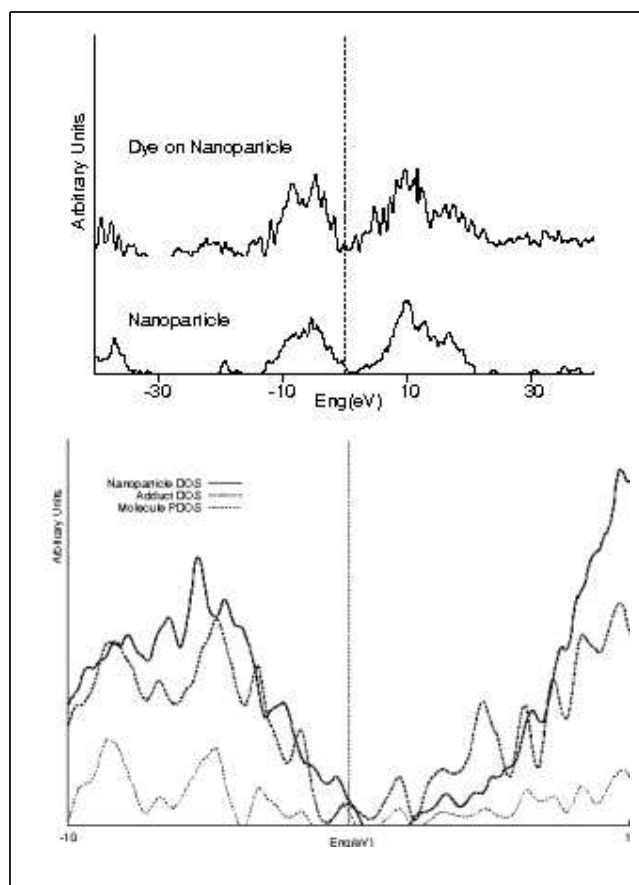
Figure 5.8: Effective Density of State (ONIOM-DOS) of the Ti$_{54}$O$_{108}$ and Ti$_{54}$O$_{108}$:Ru(Ph) systems. Upper graph: The valence and conduction bands. Lower graph: focus on the band-gap states.

in the lower graph of Figure 5.8, together with the DOS of the bare nanoparticle. The single pick localized within the nanoparticle band gap is mainly a sensitizer contribution, while a number of mixed molecular-semiconductor states are located shortly above the edge of the nanoparticle conduction band. This is consistent with the idea that the photoexcitation processes involve states strongly localized at the sensitizer-oxide interface.

Recent theoretical studies[195,196] have proved that the solvent significantly stabilizes the ground state of Ruthenium dyes. In our computational approach the solvent effects were accounted by mean of the PCM model. In this case we have adopted the minimal interface model (Ti$_4$O$_8$:Ru(Ph)). Figure 5.9 reports the
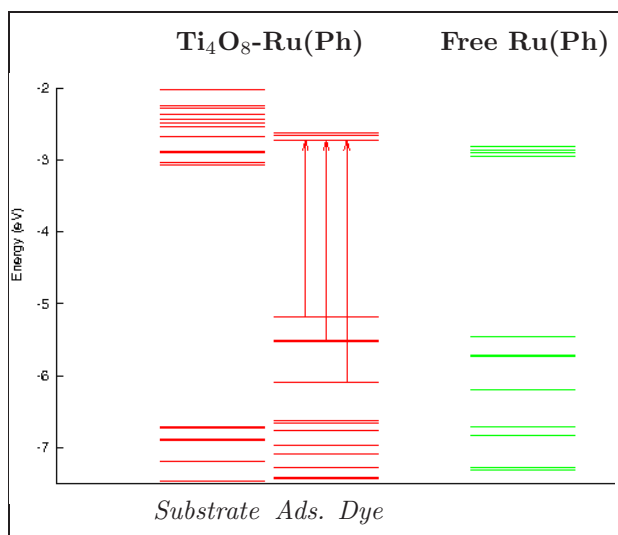
Figure 5.9: The energy level scheme of the free dye (green color) and the combined system (red color), in ethanol, computed at PCM/B3LYP level.

orbital energy scheme of the combined system and the isolated dye, computed at PCM/B3LYP level in ethanol. The interface levels are divided into two groups according to the origin of their major contributions: those orbitals mainly (over 50%) localized on the dye were referred to as "adsorbate", the remaining being referred to as "substrate" levels. Informations pertaining the occupied and unoccupied orbitals of interest are summarized in Table 5.6, including orbital energies, their location and main character. Some of the selected orbitals are plotted in Figure 5.10.

The adsorbate orbital structure is in many ways similar to that of the free dye. In the combined system, the few highest occupied orbitals are located near the middle of the substrate band gap and are mostly due to the dye contribution. For example, the highest occupied molecular orbital (HOMO) is a Ru 4d orbital that is delocalized onto the NCS ligands (see Figure 5.10). This characteristic delocalization is consistent with HOMO computed on the free Ruthenium dye (results not shown): Ru(II) dyes typically have six electrons occupying three nearly degenerate t_{2g} Ru 4d orbitals. For NCS containing complexes, the NCS groups contribute additional occupied orbitals in the same energy range as the t_{2g} Ru 4d orbitals, so that the HOMOs of the free dye are mixed with Ru-NCS orbitals. The HOMOs of the free dye are thus well preserved upon interaction with the TiO$_2$ substrate, indicating poor energy matching with the substrate bands. The HOMO-1 and HOMO-2 are still due to a mixing between the metal d orbitals and the π-NCS, while the HOMO-3 is mainly an NCS orbital.

The lowest unoccupied molecular orbitals (LUMO $\div$ LUMO+3) are largely lo-

cated on the substrate atoms, with a relevant contribution located at the anchoring -COO moieties. The first unoccupied molecular orbitals located on the sensitizer (LUMO+4 and LUMO+5) have a strong phenanthroline-π^* character, with a small contribution from the anchoring groups.
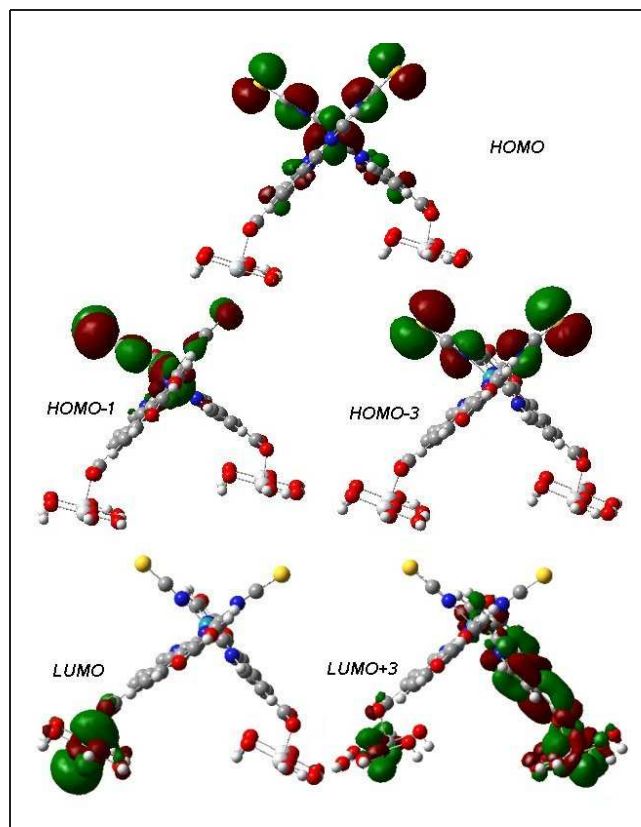
Figure 5.10: Molecular orbital plots of the combined system, $Ti_4O_8:Ru(Ph)$, in ethanol.

5.2.3 The Photophysical Properties of the Interface

The crucial photoinduced charge separation in the dye-sensitized solar cells is accomplished at the dye-semiconductor interface[63,146]. Once the sensitizer has been excited in the visible region, one excited electron is transferred to the nanoparticle conduction band. Due to a strong electronic coupling between the substrate and the adsorbate, the electron injection process proceeds faster then the nuclear

MO	Eng(eV)	main character
HOMO,-1,-2	-5.18±-5.52	$Ru_{4d} \cdots NCS$
HOMO-3	-6.09	NCS
HOMO-4,-5	-6.63,-6.67	π-Ph
HOMO-6,-7	-6.71,-6.74	anchoring-COO
HOMO-8	-6.76	Ru_{4d} (π NCS)
HOMO-11,-12	-6.97,7.10	π-Ph
HOMO-13,-14	-7.20	TiO_2
HOMO-15,-17	-7.28,7.42	π-Ph
LUMO	-2.96	TiO_2
LUMO+2,+3	-2.83,-2.81	$TiO_2 \cdots COO \cdots Ph$
LUMO+4,+5	-2.71,-2.65	π-Ph
LUMO+6,+7	-2.60,-2.57	$TiO_2 \cdots COO \cdots Ph$
LUMO+11,+12	-2.30,-2.19	$TiO_2 \cdots Ph$

Table 5.6: Energy and main character of relevant occupied (HOMOs) and unoccupied (LUMOs) molecular orbitals of the combined Ti_4O_8:Ru(Ph) system in ethanol.

relaxation of the sensitizer. The mechanism of the ultrafast electron transfer is still under debate. In particular the role played by the intermediate excited states, coupled with the substrate conduction band states, is still controversial. Two electron injection mechanisms have been postulated[197], as shown in Figure 5.11. A mechanism involving a direct photoexcitation from the dye to an empty state (Figure 5.11 right scheme) of the nanoparticle is believed to occur for the $[Fe(CN)_6]^{4-}$ on TiO_2[69]. Similar mechanism was postulated by Persson et al. in the case of Catechol sensitizer[68]. For the Ru(II)-polypyridyl dyes a generally accepted injection mechanism involves photoexcitation to a dye excited state, from which an electron is transferred to the titania conduction band (Figure 5.11 left scheme).

Typically , Ruthenium dyes absorbs light by well understood metal to ligand charge transfer (MLCT) excitations from the highest occupied Ru 4d orbitals to the unoccupied π^* orbitals on the phenanthroline ligands (poly-pyridine ligands in N3)[198]. According to the ground state B3LYP molecular orbitals on the combined system (see Figure 5.9), the occupied HOMO÷HOMO-2 display significant Ru 4d character, while the unoccupied LUMO+2÷ LUMO+8, can be seen as the coupling between phenanthroline π^* and the substrate unoccupied states.
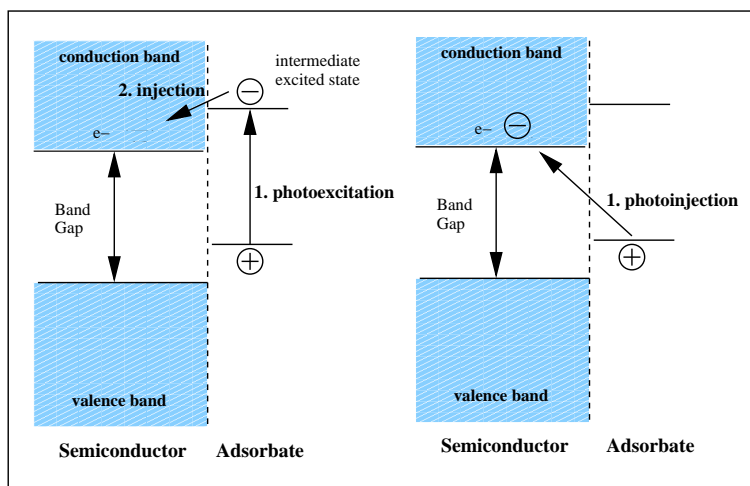
Figure 5.11: The two postulated mechanisms (see Ref. [197]) for the charge transfer at the dye/semiconductor interface. Left: photoexcitation followed by electron injection. Right: direct photoinjection.

The comparison between the simulated and experimental adsorption spectra of the interacting system, can be helpful in understanding the charge transfer process. In this context, the Time-Dependent DFT procedure is a powerful but computationally expensive tool for the calculation of the excitation spectra: so far, the adsorption spectra of the adsorbed sensitizer has been never resolved computationally[69,70]. Moreover, the dimension of the problem to be solved in the TD-DFT procedure increases by introducing the solvent effect. In the present work, the adsorption spectra of the combined Ti_4O_8:Ru(Ph) system in the ground state geometry was fully resolved at PCM/TD-B3LYP, by selecting an active subspace of the molecular orbitals[6] to be used in the POST-DFT calculation of the excitation poles. This subspace obviously includes those HOMOs and LUMOs orbitals (discussed before) which are expected to be involved in the MLCT transitions, according to the *hole-particle/particle-hole* formalism.

The first 60 singlet-to-singlet vertical excitations for the free dye and the combined Ti_4O_8:Ru(Ph) system in ethanol. The obtained excitations in the region between 400 and 600 nm for the combined system are reported in Figure 5.13. In Figure 5.12 the experimental (top graph) and simulated (lower graph) absorption spectra of free (dashed line) and adsorbed (solid line) Ru(Ph) in ethanol are
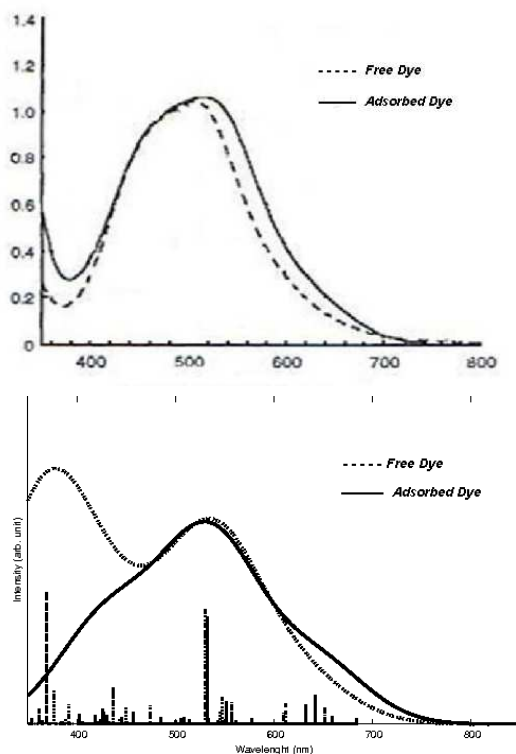
Figure 5.12: The adsorption spectra of the free (dashed lines) and adsorbed dyes (solid lines): experimental spectra (top graph); computed spectra (lower graph).

reported. The simulated spectra were obtained as Gaussians broadening of each computed excitations by an arbitrary factor of 30 nm.

The MLCT transition in the experimental spectra appears as a broad band characterized by at least two strong absorptions: the maximum at ∼530 nm and a little shoulder at ∼450 nm. A good agreement was found between the experimental and computed spectra. The main absorption picks are indeed well reproduced, together with the red shift undergone by these bands upon adsorption.

The computed spectra (in the region between 400 and 600 nm) is composed by three bands (Figure 5.13), whose main features are summarized in Table 5.7. According to the principal MO contributions, the three main vertical excitations are MLCT transitions in the dye, each one being dominated by one-electron transition from the HOMO, HOMO-1(-2) and HOMO-3 orbitals, respectively. In particular, the absorptions at 642 nm are dominated(%88) by the HOMO → LUMO+2(+3) transitions. The absorption at 532 nm is due to HOMO-1(-2) → LUMO+6(+4) transitions, with transitions from HOMO-1 and HOMO-2 orbitals

Figure 5.13: The computed TD-DFT singlet-to-singlet vertical excitations on the combined Ti$_4$O$_8$:Ru(Ph) system in ethanol.
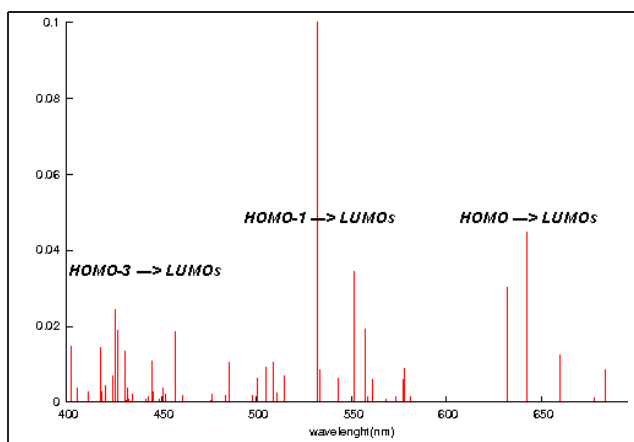
state	E(nm)	f	dominant contribution	character
S5	642	0.0448	88% HOMO →LUMO+2,LUMO+3	MLCT
S20	532	0.1646	42% HOMO-2 → LUMO+4 42% HOMO-1 → LUMO+6	MLCT
S50	425	0.0243	95% HOMO-3 → LUMO+2,LUMO+3	MLCT

Table 5.7: Excitation energy (nm), oscillator strength (f), dominant contribution and character of the main singlet-to-singlet TD-DFT excitations.

contributing by 42%, each. Finally the third absorption is mainly a HOMO-3 → LUMO+2(+3), with a contribution above 95%. The unoccupied molecular orbitals of these single-electron transitions display mainly π^*-phenanthroline character. It worths to notice however that the highest contributions come from those single-electron transitions involving LUMOs having a significant electron density located at the anchoring/TiO$_2$ interface, i.e. LUMO+2 and LUMO+3 (see Figure 5.10).

In conclusion, the MLCT transitions result into a sensitizer excited states strongly coupled to the surface quasi-continuum states of the TiO$_2$. Thus the calculations indicate that a direct charge transfer might occur at the interface with little or no contribution from the dye excited state. In contrast to what was previously assumed, these results are consistent with the direct photoinjection mechanism.

H-Si(100) surface functionalized with Ferrocene derivatives

Self-assembled, redox-active organic monolayers on Si electrodes constitute a promising step toward molecule-based hybrid devices compatible with the crystalline silicon platforms like FLASH and DRAM memories[199] or chemical/biological sensors[200−202].

Due to the attractive electrochemical properties of ferrocenes (fast e-transfer rates and favorable redox potentials), their introduction in organic monolayers bound to gold has been widely described in the literature[203−208]. So far, however, the anchoring of ferrocene (Fc) derivatives on Si has been seldom attempted, maybe due to the difficulty of establishing robust Si-C or Si-O bonds without oxidation of the Si substrate. Fc substituted by short linkers anchored directly on Si(100)[199,209−213] or coupled to preassembled, acid-terminated alkyl monolayers on Si(111) have recently been reported.[214] Although a meaningful comparison of the former with the latter approach is difficult, due to the inherently different reactivities of the (100) and (111) surfaces, it was found that the short-chain redox hybrids on Si-(100) have higher e-transfer rates but shorter lifetimes than the mixed Fc-alkyl layers on Si(111).[209]

The most used chemical route to establish a carbosilane bond between Si and the redox organometallic molecules has been the reaction of unsaturated molecular linkers with the H-terminated Si(100) or (111) surfaces, activated by visible or UV radiation.[215] The proposed mechanisms are different: the UV-induced hydrosilylation involves photolytic homolysis of a surface Si-H bond, giving rise to a radical chain reaction;[210] visible-light activation is believed to proceed via a surface exciton, in photoluminescent nanocrystalline silicon,[216,217] while for flat Si the role of the exciton has been tentatively rephrased in terms of surface plasmons.[218]

The hybrids obtained with visible-light activation bear an unknown degree of unsaturation in the C-C tethering arm, which is assumed to be reduced (from triple to double and from double to single C-C bond) upon the reaction. The anchoring on Si of a fully saturated C-C chain with a redox head, although desirable, has not been shown so far. Conversely, reaction routes allowing a controlled unsaturation in the molecules in the selfassembled monolayer (SAM) to be maintained have not been explored to a large extent.

The characterization of the hybrids can be strongly helped by a comparison between the computational results and the experimental observations. In this Chapter, the hybrids obtained by light-induced adsorption of a series of alkyl-Fc molecules (namely the ethyl-Fc, vinyl-Fc and ethynyl-Fc, referred to as R-Fc) have been studied, with the aid of a fruitful synergy between the theoretical modeling and the experimental investigation. First a suitable computational strategy to compute redox potentials was defined, and tested on the R-Fc molecules in acetonitrile. Different hybrid structures were then postulated and modeled by using a suitable sized cluster. Experimentally, a suitable grafting procedures has been defined to yield the corresponding series of redox molecular hybrids on Si: the hybrid redox potentials were measured by cyclic voltammetry and computed with accurate quantum mechanical procedures. The very satisfactory match of theoretical and experimental results shows that this procedure can be confidently used to test for the presence of unsaturated bonds in the grafted redox monolayers.

6.1 The Isolated Molecules

6.1.1 The Optimized Structures

The isolated ferrocene [Fc(II)] was initially optimized at different levels of theory. A crucial aspect in the computational treatment of transition-metal compounds
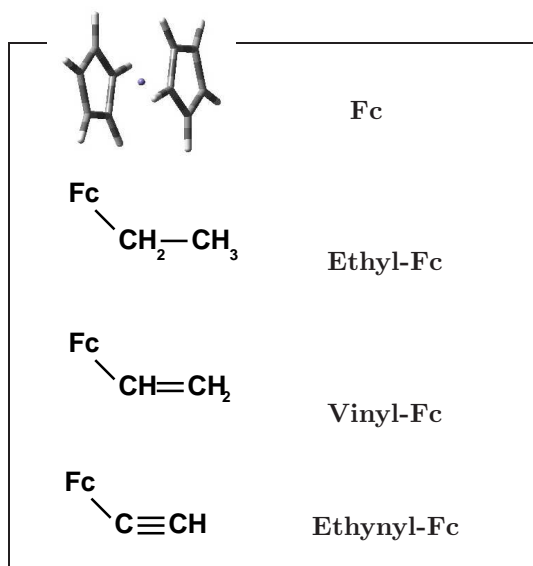
Figure 6.1: The alkyl-ferrocene (R-Fc) derivatives.

is the correct description of the metal-ligand interaction, i.e. the metal-ligand equilibrium geometry. The Hatree-Fock approach is unreliable due to the neglect of correlation effects, and provides structures with the Fe$\cdots$X distance clearly overestimated (1.872 Å [219]), with respect to the experimental one (1.66 Å [220]). For this reason we have decided to proceed at DFT level, mostly using PBE1PBE and B3LYP hybrid functionals, both providing a good description of metal-ligand interaction (see following).

Obviously the correct description of the metal-ligand interaction strongly depends on the chosen basis sets for Carbon and Iron atoms. The optimized Fe$\cdots$X distances calculated at PBE1PBE level by using different basis sets are reported in Table 6.1. For comparison, the benchmark value, computed by Koch et al.[221] at CCSD(T) level is also reported. Clearly the use of an effective core potential (LANL2DZ) on both the Fe and C atoms results in a Fe$\cdots$X larger (1.695 Å) that the one provided by the CCSD(T) calculation, meaning that the correlation is again poorly described. The quantum treatment of each Carbon electron is then mandatory: the use of complete basis sets, such as *6-31g* provides better results, expecially when one uses the polarized (*d*- and *p*-functions) and the diffuse functions. Concerning the Iron atom, the description of the metal-ligand interaction is improved by enriching the LANL2DZ core potential basis set with and extra set of polarized functions (*3df*). Interestingly, the use of complete basis set for Iron at PBE1PBE level overestimates the metal-ligand electron correlation, the

	Base/PBE1PBE	Fe···X
C,H	Fe	Distance (Å)
LANL2DZ	LANL2DZ(3df)(+ pseudo)	1.695
6-31g(d,p)	LANL2DZ(3df)(+ pseudo)	1.645
6-31+g(d,p)	LANL2DZ(3df)(+ pseudo)	1.652
6-31g(d,p)	6-31g(3df)	1.620
	TZV2P+f/CCSD(T)[221]	1.660†

Table 6.1: The Fe···X optimized distances (Å) computed at PBE1PBE level with different basis sets. Comparison with the benchmark CCSD(T)[221] value.

obtained Fe···X distance (1.620 Å) poorly agreeing with the benchmark value (1.660 Å). In conclusion, at PBE1PBE level, the best Fe···X distance is obtained using a *6-31g+(d,p)* for Carbon atoms and a LANL2DZ(*3df*) core potential basis set for Iron. This is true also for the B3LYP method.

Dist(Å)	MSINDO	B3LYP	PBE1PBE	CCSD(T)[221]	Exp.[220]
Fe···X	1.658	1.695	1.652	1.660	1.66
Fe-C	2.063	2.085	2.049		2.06
C-C	1.442	1.428	1.425		1.44
C-H	1.081	1.081	1.082		1.10

Table 6.2: The Fc(II) structure in gas phase computed with different methods. The experimental[220] and the CCSD(T) benchmark[221] values are also reported for comparison.

At equilibrium, the point-group symmetry of a gas-phase ferrocene molecule is D_{5h}, corresponding to an eclipsed relative orientation of the cyclopentadienyl rings. Nevertheless, at room temperature an appreciable fraction of ferrocene molecules is found in a staggered (D_{5d}) orientation, suggesting that the energy difference between the D_{5h} and D_{5d} is very small[220]. This was confirmed by the B3LYP and PBE1PBE optimizations: the eclipsed structure is more stable than the staggered one, the barrier between the two orientations being less than 1 kcal/mol.

The reliability of the two hybrid DFT approaches (B3LYP and PBE1PBE) in reproducing the Fc geometrical features has been checked in Table 6.2: here the computed gas-phase stable structures were compared with the experimental

gas-phase electron diffraction structure[220]. Both the B3LYP and the PBE1PBE geometries agree with the experimental one. In table 6.2 we have also reported the geometrical parameters of the MSINDO optimized structure: surprisingly this semiempirical approach describes well the metal-ligand interaction, providing a stable structure close to both the DFT-calculated and the experimental structures.

Distance(Å)	PBE1PBE	PCM:PBE1PBE
Fe$\cdots$X	1.652	1.652
Fe-C	2.049	2.050
C-C	1.425	1.426
C-H	1.082	1.085

Table 6.3: Comparison between the Fc(II) structures optimized at PBE1PBE level in gas phase and in acetonitrile (PCM:PBE1PBE)

Since the computed redox potential is expected to depend on the compound structure, the ferrocene stable geometry in solution (acetonitrile) was computed at PCM/PBE1PBE level. The obtained structure was then compared with the gas-phase stable one (Table 6.3): according to our calculations, the ferrocene does not undergo strong structural changes due to the interaction with the solvent. This observation allows the use of gas-phase structures to compute redox potentials.

Ethyl   **Vinyl**   **Ethynyl**
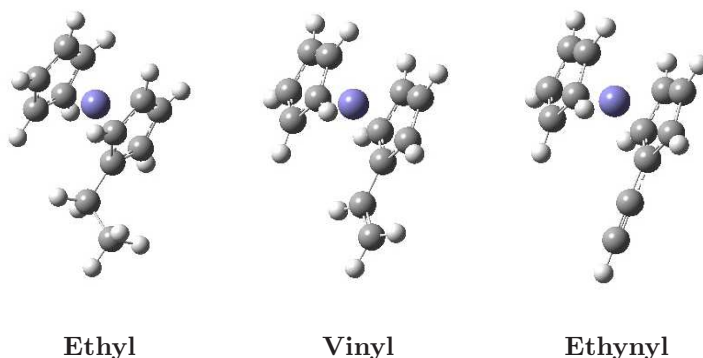
Figure 6.2: The PBE1PBE optimized structure of the R-Fc derivatives.

The alkyl-ferrocenes have been optimized at PBE1PBE level, using the same basis set adopted for the Fc optimization. In the stable structures, shown in Figure 6.2, the geometrical features of the ferrocene head do not change significantly. Interestingly a number of local minima were found corresponding to different values of the C_{alkyl}-C_{alkyl}-C_{ring}-C_{ring} dihedral angle, for the Ethyl-Fc and Vinyl-Fc structures.

Thanks to the high degree of rotational freedom around the C_{alkyl}-C_{ring} bond, one can suppose that two neighboring adsorbed ferrocene derivatives might arrange themselves in order to reach an optimal stacking distance. This point will be discussed in the next Section.

6.1.2   The redox potential of ferrocenes

Moiety	Radius
C	2.840
CH	3.140
CH2	3.440
CH3	3.740
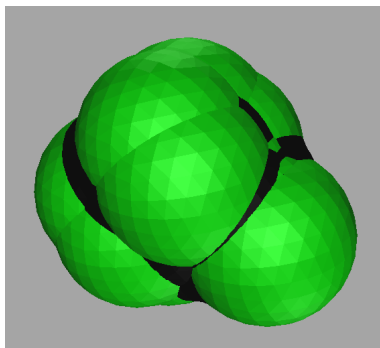
Figure 6.3: The PCM cavity for the alkyl-ferrocenes.

Table 6.4: The radius of the spheres used to built the PCM-cavity for the alkyl-ferrocenes.

We consider the redox potential associated with the Fe(II)/Fe(III) redox couple. Redox potentials (in volts) are theoretically evaluated by computing the molecular energies for the oxidized and reduced forms in the solvent (acetonitrile):[222][223]

$$V = -[(E_{red} - E_{ox}) + (\Delta G_{red}^{CH_3CN} - \Delta G_{ox}^{CH_3CN})] - V^0$$

where the energies (E_x) (conventionally more negative for stabler species) and the solvation free energies ($\Delta G_x^{CH_3CN}$) are computed in electronvolt at the PCM:B3LYP with the same basis set used for the optimization. V^0 is the absolute potential of the reference electrode: for instance, the normal hydrogen electrode (NHE), to which the following calculations are referred, has $V^0 = 4.43$ V.[224] The computed potentials can be directly compared to the experimental ones, provided the

latter are referred to the same standard electrode. We did not include thermal (vibrational and rotational) contributions, whose variations among the substituted ferrocenes series were found to be negligible (results not shown): this was furthermore confirmed *a fortiori* by the very good agreement with the experimental potentials of the ferrocene derivatives in solution (see below).

The solute-solvent interactions were included at PCM level: in this method (see Section 2.2.4 and related literature for more details), the solute is accommodated in a cavity (see Figure 6.3), formed by spheres centered on the solute atoms, and the solvent reaction field is described in terms of apparent charges on the cavity walls. Starting from a widely used compilation of atomic radii, optimized for aqueous solutions, we adjusted the radii for the present solvent, that is, acetonitrile. The cavity for the isolated Fc was scaled, in order to reproduce the experimental redox potential in acetonitrile through Eq. 6.1.2: in particular the radius of the cyclopentadienyl CH-centered sphere was enlarged with respect to the standard sphere.

Then computed the redox potentials of the ethyl-Fc, vinyl-Fc and ethynyl-Fc were computed at PCM:B3LYP level. The same scaling factor was applied to each standard spheres associated with the alkyl CH_x moieties (see Table 6.4) present in the R-Fc molecules, without any further adjustment. The computed
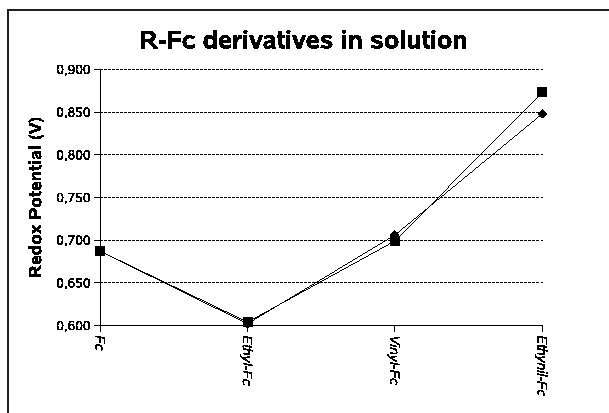
Figure 6.4: Computed (squares) and experimental (diamonds) redox potential (volts, referred to NHE) for Fc derivatives in acetonitrile.

and experimental potentials for Fc and R-Fc in acetonitrile are shown in Figure 6.4: it is worth to notice that though the PCM cavity was optimized only for Fc, excellent agreement is found for all the species.

6.2 The Adsorbed Compounds

6.2.1 The adduct structures
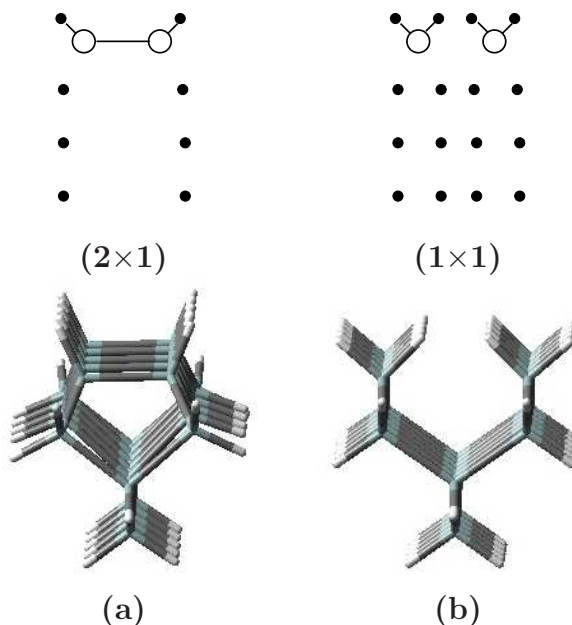
Figure 6.5: **Top**: Schematic plot of the side and top view of the (a) (2×1) mono-hydrogenated and (b) (1×1) di-hydrogenated Si(100). Empty and filled circles represent Si and H atoms, respectively; **Bottom**: $Si_{33}H_{38}$ (a) and $Si_{33}H_{48}$ (b) clusters modeling the Si-(2×1) and the Si-(1×1) surfaces, respectively.

The clean Si(100) surface forms a (2×1) reconstruction consisting of parallel rows of dimers. Each surface Si atom has one dangling bond: the saturation of these dangling bonds with Hydrogen leads to a (2×1) mono-hydrogenated surface (schematically depicted on top of Figure 6.5-*a*). Further H adsorption might break the dimer bond, forming the fully (1×1) di-hydrogenated surface, shown on top of in Figure 6.5-*b*. According to experimental STM observations and theoretical studies, the mono and di-hydrogenated forms coexist on the H-saturated Si(100) surface, along with other forms, which are intermediate between the two shown. For the R-Fc:silicon adducts, the inorganic substrate was modeled with $Si_{33}H_{38}$ and $Si_{33}H_{48}$ clusters reproducing a portion of the (2×1) and (1×1) hydrogenated surface, respectively (see bottom of Figure 6.5-*a,b*).

Considering the possible products of the R-Fc adsorption on the H-Si(100), five different adsorption geometries were assumed for each surface, schematically depicted in Figure 6.6 (mono-hydrogenated silicon) and Figure 6.7 (di-hydrogenated silicon). The *(a)-(c)* species have a σ C_{alkyl}-C_{alkyl} bond, and might result either
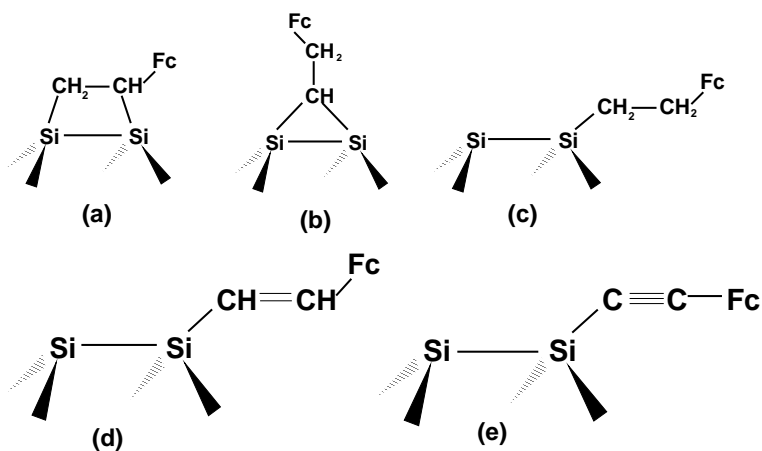
Figure 6.6: The five postulated structures of ethyl-, vinyl-, and ethynyl-Fc adsorbed on mono-hydrogenated silicon surface: **(a)** SiH-CH$_2$CH-Fc; **(b)** SiH-CHCH$_2$-Fc; **(c)** SiH-CH$_2$CH$_2$-Fc; **(d)** SiH-CHCH-Fc; **(e)** SiH-CC-Fc.

from the direct adsorption of the Ethyl-Fc or from the addiction of the Vinyl-Fc, with loss of unsaturation; *(d)* might derive from the addiction of either Vinyl-Fc (without loss of unsaturation) or Ethynyl-Fc (with consequent loss of one unsaturation); finally *(e)* might result from the direct adsorption of Ethynyl-Fc, i.e. by keeping the unsaturation.

The adduct clusters have been optimized at PBE1PBE:MSINDO level: the organic adsorbate together with the bounded Si atom(s) were selected as the high level region in the ONIOM scheme, using hydrogen as link atom. The substrate atoms were kept frozen in their surface reconstructed position, while the adsorbate was fully relaxed. The same basis set used to optimize the free molecules has been applied to the atoms in the high level calculations. A LANL2DZ basis set, with the corresponding core potential, was used for the bounded Si atom(s). The obtained structure for the SiH-CH$_2$CH$_2$-Fc adduct is shown in Figure 6.8: here the single C$_{alkyl}$-C$_{alkyl}$ bond and the Si-Si surface dimer are almost parallel and lie in the same plane. For all the species *((a)-(e))*, the ferrocene geometrical features do not change significantly upon adsorption.

In all the optimized adduct structures, the organic moiety points out by the side of adduct cluster: due to the finite lateral size of the substrate in the adduct clusters (see Figure 6.8 for the *(c)* species), the possible adsorbate/substrate non-bonding interactions might not be accounted. In order to investigate this point, the geometry of the *(a)* species adsorbed on a larger SiH(100) cluster (Si$_{121}$H$_{113}$) has
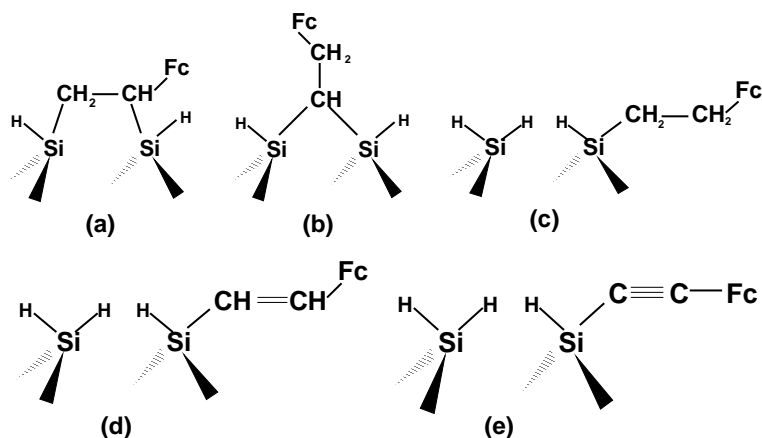
Figure 6.7: The five postulated structures of ethyl-, vinyl-, and ethynyl-Fc adsorbed on di-hydrogenated silicon surface: **(a)** SiH$_2$-CH$_2$CH-Fc; **(b)** SiH$_2$-CHCH$_2$-Fc; **(c)** SiH$_2$-CH$_2$CH$_2$-Fc; **(d)** SiH$_2$-CHCH-Fc; **(e)** SiH$_2$-CC-Fc.

been optimized, and compared with the one adsorbed on the Si$_{33}$H$_{38}$ cluster: in this case the two structures have been optimized at MSINDO level to reduce the computational burden (recall that the MSINDO-optimized molecular structures agree fairly well with the ones obtained at PBE1PBE level, as shown in Section 6.1.1). The adsorbate geometry optimized on the Si$_{121}$H$_{113}$ cluster seems to be only slightly influenced by the presence of a larger substrate: the ferrocene head rotates rigidly upwards around the C$_{ring}$-C$_{alkyl}$ bond, without any further deformation. According to our calculations, the non-bonding adsorbate/substrate interactions are negligible.

Thanks to the high degree of rotational freedom around the C$_{alkyl}$-C$_{ring}$ bond (see Section 6.1.1), the incoming ferrocene derivatives are expected to arrange themselves to meet the optimal stacking distance. In order to investigate this point we have considered three arrangements of the Ethyl-Fc dimer (see Figure 6.9): *(i)* the two un-substituted cyclopentadienyl rings lie on parallel planes, so that a π-π interaction occurs between the two ferrocene heads ("face-to-face"); *(ii)* the two cyclopentadienyl rings lie onto the same plane ("side-by-side"); *(iii)* the planes containing the two cyclopentadienyl rings are orthogonal, so that one ring-hydrogen can interact with the aromatic system of the other ferrocene head ("face-to-side"). The energy of the dimer has been determined at PBE1PBE level and reported in Figure 6.10 as a function of the Fe· · ·Fe distance. The energy of two non-interacting Ethyl-Fc molecules is also reported. Taking the energy of
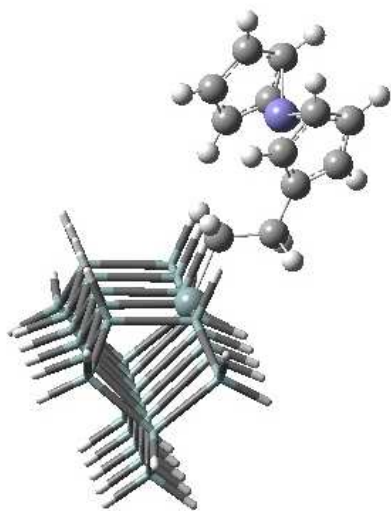
Figure 6.8: The SiH-CH$_2$CH$_2$-Fc adduct cluster optimized at PBE1PBE:MSINDO level.

the two separate molecules as reference state, the "face-to-side" arrangement is favored with respect to the other two, and the optimal distance is 6.8Å. The less stabilizing "face-to-face" interaction corresponds to an optimal distance of 7.5Å while no net energy minimum is found due to a "side-by-side" interaction.

These optimal distances need to be compared with the 3.85Å lattice spacing in Si(100): assuming an ideal coverage on H-Si(100) surface, each molecule might bind on every single Si-dimer on alternating sides, in this case assuming a "face-to-side" arrangement (see Figure 6.11). Other ways, the incoming molecules might anchor every second Si-dimers along the same side (top of Figure 6.12) or on alternating sides (bottom of Figure 6.12), in both cases arranging themselves in a "face-to-face" configuration. As expected, among the three adduct clusters (shown in Figures 6.11 and 6.12) optimized at MSINDO level, the "face-to-side" arrangement is found to be slightly more stable.

A more detailed investigation of the attractive/repulsive interactions occurring upon ferrocene derivatives adsorption and leading to a non-ideal coverage is beyond the goal of the present study. The distance between neighbor ferrocene heads is in any case large enough to assume that the adsorbate geometrical and electronic structure is slightly influenced by the occurring adsorbate-adsorbate interactions. We therefore believe that the adduct clusters previously shown (see Figure 6.8) are suitable interface models for the redox potential study of the species formed upon adsorption.
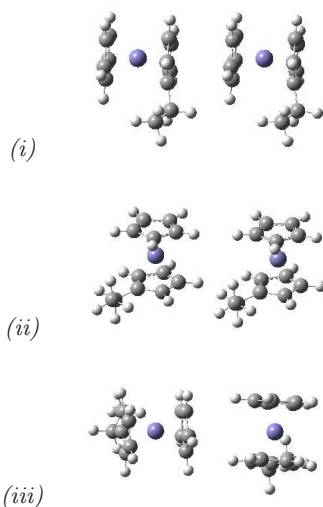
Figure 6.9: Possible arrangements of two Ethyl-Fc molecules: *(i)*: "face-to-face"; *(ii)*: "side-by-side"; *(iii)*: "face-to-side".
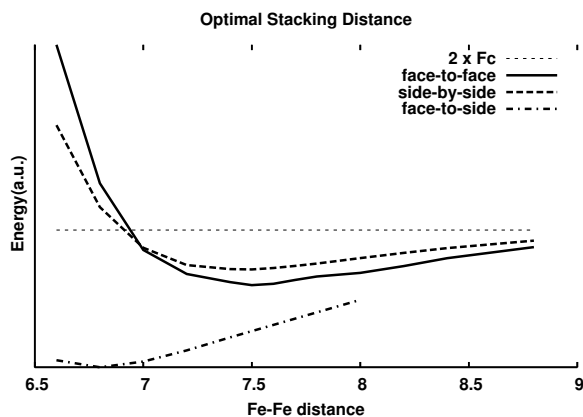
Figure 6.10: The optimal stacking distance (Å) for the three possible arrangements (see Figure 6.9 for labeling).

6.2.2   The adsorbate redox potential

On the optimized adduct clusters corresponding to the *(a)-(e)* species shown in Figures 6.6 and 6.7, the redox potentials were computed at the B3LYP level, i.e. extending the quantum treatment also to the substrate atoms. The used basis set was the same adopted for the high level calculations in the ONIOM optimization. The solvent effects were again introduced at PCM level: the whole adduct was embedded in the solute cavity, and the same PCM parameters used for the free molecules (see Table 6.4) were applied to the organic moieties of the adducts, leaving the default spheres for silicon (2.148 Å) and capping hydrogens (1.443 Å).

The computed potentials for the adducts on Si-(2×1) and Si-(1×1) are reported in Figure 6.13. The horizontal lines in Figure 6.13 indicate the experimental values, i.e. the measured redox potentials of species obtained by light-induced adsorption of the ethyl-Fc (bottom line), vinyl-Fc, and ethynyl-Fc (top line). The experimental adsorption conditions, the same in the three cases, are reported in Ref. [225]: for the first time the authors have attempted the adsorption of a saturated alkyl-Fc derivative, namely the ethyl-Fc, obtaining the product
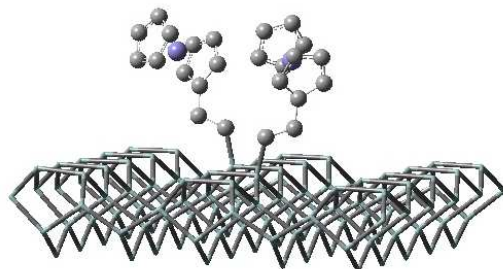
Figure 6.11: The "face-to-side" arrangement. Two *(c)* species (see Figure 6.9 for labeling) adsorbed on the large ($Si_{121}H_{113}$) H-Si(100) cluster model. Structure optimized at MSINDO level.

(i)

(ii)
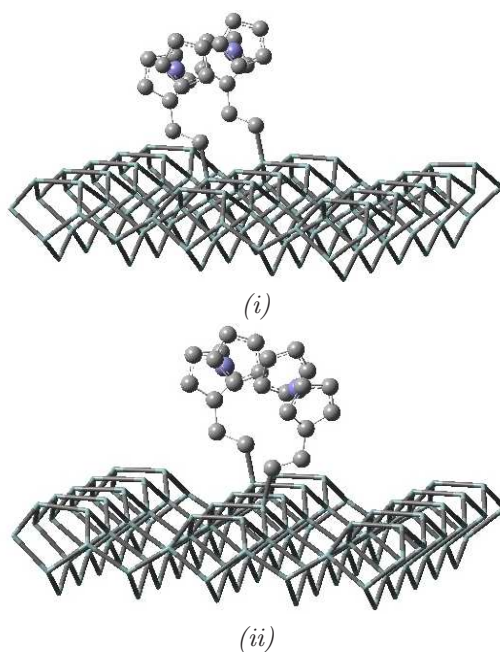
Figure 6.12: The "face-to-face" arrangement: the two adsorbates are *(i)* on the same side of the dimer line or *(ii)* on opposite sides. Structures optimized at MSINDO level.

Figure 6.13: Computed redox potential (volts, referred to NHE) for different alkyl-ferrocene adducts ((a)-(e)) see Figures 6.6 and 6.7 for labeling) on mono-(diamonds) and di-hydrogenated (squares) silicon surfaces. The experimental values for the adducts obtained with ethyl-Fc (solid horizontal line), vinyl-Fc (fine dashed horizontal line), and ethynyl-Fc (large dashed horizontal line) are also reported for comparison.
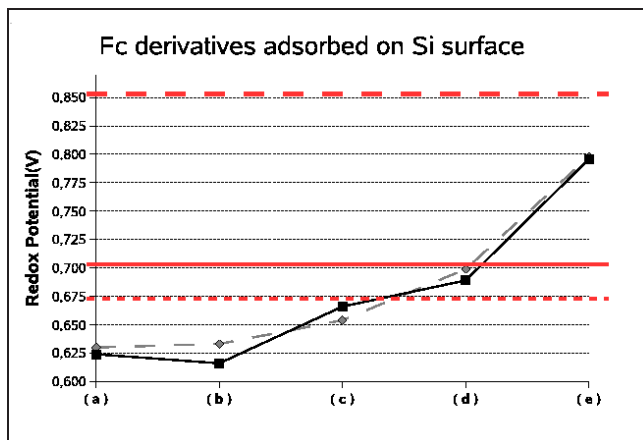
characterized by the lowest redox potential reported (6.13). The structure and stoichiometry of the species obtained by light induced adsorption of each R-Fc molecules are unknown: in the case of vinyl-Fc and ethynyl-Fc adsorption, the obtained products might in principle consist of an hybrid mixture of saturate and unsaturated adsorbed moiety.

The computed redox potentials for the Si-(2×1) and Si-(1×1) adduct clusters are very similar. Since the standard Si sphere was used for the PCM cavity, any agreement between the computed and the experimental values for the adsorbed species is expected to be less satisfactory than that for isolated R-Fc molecules. In any case, the measured potential for the adduct obtained from Ethyl-FC is clearly more compatible with structure *(c)*.

Even within the systematic theoretical error, the comparison of calculated (for *(d)* and *(e)* adducts) and measured potentials seems to indicate that the carbon chain unsaturations are preserved upon adsorption, in contrast with the common interpretation of the addition mechanism. This conclusion is reinforced by considering the differences among the measured potentials and among the computed values for structures *(c)*, *(d)*, and *(e)* (i.e., by assuming that the systematic error is the same for saturated and unsaturated adducts).

In conclusion, the comparison between the experimentally measured and accurately computed redox potentials is an useful procedure to characterized the obtained compounds. This is particularly important in the case of adsorption of
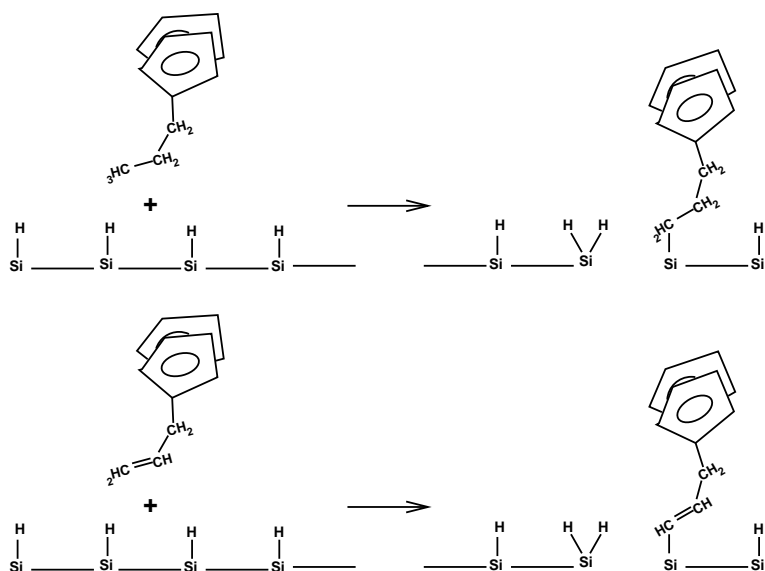
Figure 6.14: The adsorption, without loss of unsaturation, of differently (un)saturated alkyl-ferrocenes on SiH(100).

unsaturated molecules, i.e. whenever differently unsaturated adsorbed products can be obtained. Comparing the computed and measured potentials we could discriminate between different isomers of the saturated adduct.

According to our calculations, the adsorption process seems to follow a different mechanism from the one previously postulated, in which only unsaturated moieties were expected to anchor the surface, with consequent loss of unsaturation(s). We have indeed found strong indications that the unsaturations are preserved during the addition (Figure 6.14), thus suggesting that the hydrosilylation activated by visible light proceeds through a mechanism not yet described.

CHAPTER 7

Conclusions

The aim of this thesis was to develop computational strategies and models suitable for the study of adsorption processes and interface atomic structures. Due to their important technological applications, the interest was mostly focused on the modified surfaces, i.e. made by organic molecules on semiconductor surfaces.

Our approach was based on molecular (semiempirical and ab-initio) methods and cluster models. Besides the standard strategies adopted to correct the finite size effect of the cluster approach (i.e. saturators and charge embedding), two new embedding strategies have been tested: in one case the environment, regarded as a macroscopic dielectric media (fully characterized by its dielectric constant) was introduced in the quantum description as a perturbing potential. This approach follows the well known Polarizable Continuum Model formalism (PCM) but it allows the use of a non-constant macroscopic dielectric function to account for large discontinuities in the environment of the cluster model (namely non-homogeneous PCM).

Otherwise, the environment is described with a cluster geometry: the embedded and embedding clusters are treated at different levels of accuracy, the two methods being integrated in the well known ONIOM scheme. Here, we have developed and tested the DFT:MSINDO approach, which represents a further improvement

with respect to the widely used QM/MM approaches, since it consists of a combination of two quantum methods. Moreover the MSINDO semiempirical method has been parameterized for a number of solid materials. This integrated approach was tested on free surfaces and interfaces, providing reliable results in modeling geometrical and electronic structures.

Three solid materials have been studied: the anatase, which is a semi-ionic material mostly used in single crystal or nanoparticle form; the H-Si(100) and the GaAs(001) surfaces, which are covalent semiconductors. Due to their different chemical nature, different cutting strategies were adopted for designing cluster models suitable for adsorption studies.

The unoxidized and oxidized GaAs (001) surfaces have been modeled by hydrogen saturated clusters of different size, at the DFT level and using the hybrid DFT:MSINDO approach. The performances of the mixed approach resulted satisfactory, when compared to the full quantum mechanical calculations.
These clusters have been used to investigate the preferred arrangements of adducts formed by one or more benzoic acid molecules adsorbed on the oxidized surface, providing very useful insights about the structure of "perfect" organic layers.
Eight possible arrangements of a single benzoic acid molecule on one of the "platforms" existing on the GaAs surface were examined, both computing their relative energy and comparing their vibrational frequencies to experimental spectra, to select the two most likely structures. Using these structures on a larger cluster (containing several platforms arranged in two parallel lines), we found the only relative orientation displaying a favorable intermolecular interaction, leading to the most likely arrangement for a perfect layer.
Taking the anchoring mode of the benzoic acid as the prototype of the organic/GaAs interface, the anchoring structure of a series of substituted dicarboxylic acids (dC-X) adsorbed on GaAs(001) has been studied using the same clusters as substrate models. The aim is to clarify the microscopic interactions responsible for the electric behavior of the modified surfaces. In particular, we concentrated on the measured change in electron affinity ($\Delta\chi$), due to the molecule adsorption.
A good correlation is found between the electric dipole moments of isolated dC-X and the measured $\Delta\chi$ of the modified surfaces, confirming previous results obtained at lower computational levels. Nevertheless, due to the geometry distortion experienced by the adsorbed molecules, it seems unlikely that the isolated system dipoles are directly related to the adduct properties.
A better correlation is found by computing the molecular orbital energies of the

adducts. The LUMO orbital concentrates on the oxide layer in the free cluster, and on the molecular arms in the adducts (while the HOMO is always located in the cluster core), and the relative energies follow the same trend of the experimental $\Delta\chi$. From this viewpoint, the good trend of isolated dipole moments with $\Delta\chi$ can be better explained with the strong correlation between the dipole and the LUMO energy, being both these quantities strongly dependent on the electronegativity of the acid substituents.

The adsorption modes of acetic acid on the anatase(010) single crystal were studied with the DFT:MSINDO approach. The substrate was modeled with a hydrogen-saturated cluster: due to the variety of different available adsorption sites, many adduct compounds were assumed and their vibrational absorption pattern was calculated with the same mixed scheme. From the comparison between theoretical and IR investigation, a number of different species are compatible with the observed vibrational pattern: both bidentate bridging and bidentate chelating anchoring occur at the surface, thus suggesting that the obtained modified surface is characterized by a certain degree of disorder and explaining the observed complexity of the IR spectra.

Thanks to the reduced computational costs of the DFT:MSINDO approach (compared to the full ab initio calculations), the anchoring modes of a large Ruthenium-based dye on anatase(101) nanoparticles was for the first time investigated at quantum level. The sensitizer structure adsorbed on a large (1 nm size) unsaturated nanocluster was determined at DFT:MSINDO level: the two considered anchoring structures are found to be equally accessible from the energetic point of view, while they differ in the occupied volume and in the ligands rotational freedom. Hence, our calculations suggest that the steric/kinetic effects rather than thermodynamic effects might discriminate between the two adsorption modes, in agreement with what assumed on the basis of IR experimental investigations.

The local interface electronic properties were computed on a minimal model, excised out from the stable large adduct structure and opportunely saturated. An excellent agreement was found between the simulated absorption spectra, computed at PCM/TD-DFT level, and the experimental one: we found that the band of interest in the photophysical processes is composed by three main electronic transitions, each one involving frontier orbitals located at the interface. This suggests that a direct photoinjection mechanism rather than a photoexcitation-photoinjection process occurs upon excitation of the sensitizer.

The possible adduct species resulting from the adsorption of a series of alkyl-substituted ferrocenes (differing only in the unsaturation degree of the anchoring

arm) on the H-Si(100) surface were modeled with the aid of a hydrogen-saturated cluster and optimized at DFT:MSINDO level.

The redox potentials of the free ferrocenes, calculated at DFT level with the inclusion of the solvent effects, are in excellent agreement with the experimental ones. The computed potential of the adduct species were compared with the redox potentials measured on the hybrid compounds resulting from the newly performed, visible-light activated hydrosilylation: we found strong indications that the unsaturations are preserved during the addition, thus suggesting that this novel preparation proceeds through a mechanism not yet described.

The theoretical study of interfaces (of nanometer size) can strongly profit from the use of mixed methods. The integrated DFT:MSINDO approach has provided reliable results in modeling interface properties of rather different systems, proving to be a good compromise between accuracy and computational feasibility. The surface features of the IV-period materials are satisfactorily reproduced, being the MSINDO suitably parameterized, while the bonding structure of the adsorbed species is correctly treated at DFT level. Reliable energies and vibrational frequencies are obtained within this integrated approach. Moreover this approach is found to be useful as pre-screening tool in adsorption studies, when many different anchoring modes have to be considered, and the ab initio treatment of the whole adduct clusters is computational prohibitive.

Once the interface structure has been determined using a suitably large cluster model, the interface model can be reduced to a minimal size and treated at ab initio level. Along with the standard saturating and embedding strategies, the use of a non-homogenous PCM embedding potential might be a valuable aid in correcting the fictitious effects due to the finite size of the adduct model, and a further improvement in the description of those long range environmental effects affecting the interface properties.

A different embedding strategy, commonly refers to as "embedding DFT", was successfully developed and implemented by Wesolowsky[226,227]: the electron density of the embedding cluster is introduced as a perturbing potential into the DFT treatment of the embedded cluster. We believe that this approach might be a valuable tool to be integrated in a protocol of mixed methods specifically designed for the study of complex adsorbate/substrate systems. Nevertheless, this procedure has been developed for non-covalent systems: the extension of its applicability to a larger domains of solid systems will be the goal of our future work.

Bibliography

[1] Levine I.N. *Quantum Chemistry (fifth edition)*. Prentice Hall, 2000.

[2] Becke A.D. *Phys. Rev. B.*, 38:3098, 1998.

[3] C. Adamo and V. Barone. *J. Chem. Phys.*, 110:6158, 1999.

[4] Casida E.M. *Recent Developments and Application of Modern Density Functional Theory*. Elsevier Science, 1996.

[5] Casida E.M. *Advances in Density Functional Theory*, volume 3. World Scientific, 1999.

[6] A. J. Austin, M.J. Frisch, J. Montgomery, and G.A. Petersson. *Theor. Chem. Acc.*, 107:180, 2002.

[7] M. J. Frisch, G. W. Trucks, H. B. Schlegel, G. E. Scuseria, M. A. Robb, J. R. Cheeseman, J. A. Montgomery, Jr., T. Vreven, K. N. Kudin, J. C. Burant, J. M. Millam, S. S. Iyengar, J. Tomasi, V. Barone, B. Mennucci, M. Cossi, G. Scalmani, N. Rega, G. A. Petersson, H. Nakatsuji, M. Hada, M. Ehara, K. Toyota, R. Fukuda, J. Hasegawa, M. Ishida, T. Nakajima, Y. Honda, O. Kitao, H. Nakai, M. Klene, X. Li, J. E. Knox, H. P. Hratchian, J. B. Cross, V. Bakken, C. Adamo, J. Jaramillo, R. Gomperts, R. E. Stratmann, O. Yazyev, A. J. Austin, R. Cammi, C. Pomelli, J. W. Ochterski, P. Y. Ayala, K. Morokuma, G. A. Voth, P. Salvador, J. J. Dannenberg, V. G. Zakrzewski, S. Dapprich, A. D. Daniels, M. C. Strain, O. Farkas, D. K. Malick, A. D. Rabuck, K. Raghavachari, J. B. Foresman, J. V. Ortiz, Q. Cui, A. G. Baboul, S. Clifford, J. Cioslowski, B. B. Stefanov, G. Liu,

A. Liashenko, P. Piskorz, I. Komaromi, R. L. Martin, D. J. Fox, T. Keith, M. A. Al-Laham, C. Y. Peng, A. Nanayakkara, M. Challacombe, P. M. W. Gill, B. Johnson, W. Chen, M. W. Wong, C. Gonzalez, and J. A. Pople. Gaussian 03, Revision C.02. Gaussian, Inc., Wallingford, CT, 2004.

[8] T.H. Dunning and P.J. Hay. *Modern Theoretical Chemistry*, volume 3. Plenum: New York, 1977.

[9] R. Ahlrichs and P.R. Taylor. *J. Chim. Phys. Phys. Chim. Biol.*, 78:315, 1981.

[10] S. Huzinaga. *Comp. Phys. Rep.*, 2:279, 1985.

[11] E.R. Davidson and D. Feller. *Chem. Rev.*, 86:681, 1986.

[12] J. Koutecky and P. Fantacci. *Chem. Rev.*, 86:539, 1986.

[13] J.A. Pople and D.L. Beveridge. *Approximate Molecular Orbital Theory*. McGraw-Hill:New York, 1970.

[14] J.A. Pople, D.L. Beveridge, and P.A. Dobosh. *J. Chem. Phys.*, 47:2026, 1967.

[15] N.C. Baird and M.J.S. Dewar. *J. Chem. Phys.*, 50:1262, 1969.

[16] D.N. Nanda and K. Jug. *Theor. Chim. Acta*, 57:95, 1980.

[17] B. Ahlswede and K. Jug. *J. Comput. Chem.*, 20:563, 1999.

[18] B. Ahlswede and K. Jug. *J. Comput. Chem.*, 20:572, 1999.

[19] K. Jug, G. Geudtner, and T. Homann. *J. Comput. Chem.*, 21:974, 2000.

[20] T. Bredow, G. Geudtner, and K. Jug. *J. Comput. Chem.*, 22:861, 2001.

[21] F. Maseras and K. Morokuma. *J. Comput. Chem.*, 16:1170, 1995.

[22] S. Humbel, S. Sieber, and K. Morokuma. *J. Chem. Phys.*, 105:1959, 1996.

[23] T. Matsubara, S. Sieber, and K. Morokuma. *Int. J. Quant. Chem.*, 60:1101, 1996.

[24] M. Svensson, S. Humbel, R.D.J. Froese, T. Matsubara, S. Sieber, and K. Morokuma. *J. Phys. Chem.*, 100:19357, 1996.

[25] M. Svensson, S. Humbel, and K. Morokuma. *J. Chem. Phys.*, 105:3654, 1996.

[26] S. Drappich, I. Komaromi, K.S. Byun, K. Morokuma, and Frisch. M.J. *J. Mol. Struct. (Theochem)*, 462:1, 1999.

[27] T. Vreven and K. Morokuma. *J. Comput. Chem.*, 21:1419, 2000.

[28] I. Antes and W. Thiel. *J. Phys. Chem. A*, 103:9290, 1999.

[29] T. Krüger and A. F. Sax. *J. Comp. Chem.*, 23:371, 2002.

[30] G.A. DiLabio, R.A. Wolkow, and E.R. Johnson. *J. Chem. Phys.*, 122:44708, 2005.

[31] J. Sauer. *Chem. Rev.*, 89:199–255, 1989.

[32] K. Jug. *Int J Quantum Chem.*, 58:283, 1996.

[33] P. Deak. *Phys. Stat. Sol.(b)*, 217:9, 2000.

[34] C. Kittel. *Quantum Theory of Solids; 2nd revised printing.* Wiley, 1987.

[35] W. A. Harrison. *Solid State Theory.* Dover, 1980.

[36] W. A. Harrison. *Electronic Structure and the Properties of Solids, The Physics of the Chemical Bonds.* Dover, 1989.

[37] C. Pisani, R. Dovesi, and C. Roetti. *Hartree-Fock Ab Initio Treatment of Crystalline Systems, Lecture Notes in Chemistry.* Springer:, 1988.

[38] A. J. Bennett, B. McCarroll, and R. P. Messmer. *Phys Rev B*, 3:1397, 1971.

[39] M. McCarroll and R. P. Messmer. *Surf Sci*, 27:451, 1971.

[40] T. Bredow, G. Geudtner, and K. Jug. *J. Comp. Chem.*, 22:89, 2000.

[41] R.A. Evarestov, T. Bredow, and K. Jug. *Phys. Sol. State*, 43:1774, 2001.

[42] k. Jug and t. Bredow. *j. comput. chem*, 25:1551–1567, 2004.

[43] I. Laszlo. *Int J Quantum Chem*, 21:813, 1982.

[44] M. Krack, T. Bredow, and K. Jug. *Chem Phys Lett*, 237:250, 1995.

[45] M. Pöhlchen and V. Staemmler. *J Chem Phys*, 97:2583, 1992.

[46] G. Pacchioni, G. Cogliandro, and P. S. Bagus. *Int J Quantum Chem*, 42:1115, 1992.

[47] H. Nakatsuji and Y. Fukunishi. *Int J Quantum Chem*, 42:1001, 1992.

[48] T. Bredow, G. Geudtner, and K. Jug. *J Chem Phys*, 105:6395, 1996.

[49] S. Huzinaga, L. Seijo, Z. Barandiaran, and M. Klobukowski. *J Chem Phys*, 86:2132, 1987.

[50] Z. Barandiaran and L. Seijo. *J Chem Phys*, 89:5739, 1988.

[51] V. A. Nasluzov, V. V. Rivanenkov, A. B. Gordienko, K. Neyman, U. Birken-heuer, and N. Rsch. *J Chem Phys*, 115:8157, 2001.

[52] S. Miertus, E. Scrocco, and J. Tomasi. *Chem Phys*, 55:117, 1981.

[53] C. Amovilli, V. Barone, R. Cammi, E. Cances, M. Cossi, B. Mennucci, C.S. Pomelli, and J. Tomasi. *Adv. Quantum. Chem.*, 32:227, 1998.

[54] V. Barone, M. Cossi, and J. Tomasi. *J. Chem. Phys.*, 107:3210, 1997.

[55] J.L. Pascual-Ahuir, E. Silla, and I. Tuñon. *J. Comput. Chem.*, 15:1127, 1994.

[56] G. Scalmani, N. Rega, M. Cossi, and V. Barone. *J. Comput. Meth. Sci. Eng.*, 2:469, 2002.

[57] M. Cossi, N. Rega, G. Scalmani, and V. Barone. *J. Chem. Phys.*, 117:43, 2002.

[58] L. Frediani, C. S. Pomelli, and J. Tomasi. *Phys. Chem. Chem. Phys.*, 2:4876, 2000.

[59] L. Frediani, R. Cammi, S. Corni, and J. Tomasi. *J. Chem. Phys.*, 120:3893, 2004.

[60] M.F. Iozzi, M. Cossi, R. Improta, N. Rega, and V. Barone. *J. Chem. Phys.*, 124:184103, 2006.

[61] V. Barone. *Recent Advaces in Density Functional Methods - Part I-*. D.P.Chong (World Scientific Publ.), 1996.

[62] A.P. Alivisatos. *J. Phys. Chem.*, 100:13226, 1996.

[63] A. Hagfeldt and M. Graetzel. *Chem. Rev.*, 95:49, 1995.

[64] E. Lucas, S. Decker, A. Khaleel, A. Seitz, S. Fultz, A. Ponce, W. Li, C. Carnes, and K. J. Klabunde. *Chem. Eur. J.*, 7:2505, 2001.

[65] P. Persson, R. Bergström, L. Ojamäe, and S. Lunnel. *Adv. Quantum Chem.*, 41:203, 2002.

[66] P. Persson, J.C.M. Gebhardt, and S. Lunell. *J. Phys. Chem. B*, 107:3336, 2003.

[67] M.A. Barteau. *Chem. Rev.*, 96:1413, 1996.

[68] P. Persson, R. Bergstrom, and S. Lunell. *J. Phys. Chem. B*, 104:10348, 2000.

[69] F. De Angelis, A. Tilocca, and A. Selloni. *J. Am. Chem. Soc.*, 126:15024, 2004.

[70] P. Persson and M. Lundqvist. *J. Phys. Chem. B*, 109:11918, 2005.

[71] J. S. Binkley, J. A. Pople, and W. J. Hehre. *J. Am. Chem. Soc.*, 102:939, 1980.

[72] J. Muscat, A. Wander, and N.M. Harrison. *Chem. Phys. Lett.*, 342:397, 2001.

[73] R. Sanjines, H. Tang, H. Berger, F. Gozzo, G. Margaritondo, and F. Levy. *J. Appl. Phys.*, 75:2945, 1994.

[74] R. Asahi, Y. Taga, W. Mannstadt, and A.J. Freeman. *Phys. Rev. B*, 61:7459, 2000.

[75] K. Jug and G. Geudtner. *Chem. Phys. Lett.*, 208:537, 1993.

[76] B. Ahlswede and K. Jug. *J. Comput. Chem.*, 20:572, 1999.

[77] T. Bredow and K. Jug. *Chem. Phys. Lett.*, 223:89, 1994.

[78] C. B. Duke. *Chem. Rev.*, 96:1237, 2000.

[79] G.A.D. Briggs and A.J. Fisher. *Surface Science Report*, 33:1, 1999.

[80] J. E. Northrup and S. Froyen. *Phys. Rev. B.*, 50:2015, 1994.

[81] T. Ohno. *Phys. Rev. Lett.*, 70(5):631, 1993.

[82] J. E. Northrup and S. Froyen. *Phys. Rev. B.*, 71:2276, 1993.

[83] V.P. Labella, H. Yang, D.W. Bullock, P.M. Thimbado, P. Kratzer, and M. Scheffler. *Phys. Rev. Lett.*, 83(15):2989, 1999.

[84] W.G. Schmidt and F. Bechstedt. *Phys. Rev. B.*, 54(23):16742–16748, 1996.

[85] G.P. Srivastava and S.J. Jenkins. *Phys. Rev. B.*, 53:12589, 1996.

[86] C. Xu, K.P. Caffey, J.S. Burnham, S.H. Goss, and N. Garrison, B.J.and Winograd. *Phys. Rev. B.*, 45:6776, 1992.

[87] J. Cerda, F.J. Palomares, and F. Soria. *Phys. Rev. Lett.*, 75:665, 1995.

[88] J.G. McLean, P. Kruse, and A.C. Kummel. *Surface Science*, 424:206, 1999.

[89] J.P. Perdew, M. Ernzerhof, and K. Burke. *J. Chem. Phys.*, 105:9982, 1996.

[90] P. C. Hariharan and J. A. Pople. *Theor. Chim. Acta*, 28:213, 1973.

[91] Jr. Dunning, T. H. *J. Chem. Phys.*, 90:1007, 1989.

[92] G. A. Petersson and M. A. Al-Laham. *J. Chem. Phys.*, 94:6081, 1991.

[93] P. J. Hay and W. R. Wadt. *J. Chem. Phys.*, 82:270, 1985.

[94] W. R. Wadt and P. J. Hay. *J. Chem. Phys.*, 82:284, 1985.

[95] P. J. Hay and W. R. Wadt. *J. Chem. Phys.*, 82:299, 1985.

[96] S.A. Chambers. *Surface Science*, 261:48, 1992.

[97] H. Li and S.Y. Tong. *Surface Science*, 282:380, 1993.

[98] L.D. Broekman, R.C.G. Leckey, J.D. Riley, L.E. Stampfl, B.F. Usher, and B.A. Sexton. *Phys. Rev. B*, 51:17795, 1995.

[99] N.N. Greenwood and A. Earnshaw. *Chemistry of the Elements*. Pergamon, New York, 1984.

[100] K. Sriraishi and T. Ito. *J. Cryst. Growth*, 150:158, 1995.

[101] J.G. McLean, P. Kruse, and A.C. Kummel. *Appl. Phys. Lett.*, 82:1691, 2003.

[102] S.I. Yi, P. Kruse, M. Hale, and A.C. Kummel. *J. Chem. Phys.*, 114:3215, 2001.

[103] J.Z. Sexton, S.I. Yi, M. Hale, P. Kruse, A.A. Demkov, and A.C. Kummel. *J. Chem. Phys.*, 119:9191, 2003.

[104] C.D. Thurmond, G.P. Schwartz, G.W. Kammlotot, and B. Schwartz. *J. Electrochem. Soc.*, 127:1366, 1980.

[105] W.E. Spicer, P.W. Chye, P.R. Skeath, C.Y. Su, and I. Lindau. *J. Vac. Sci. Technol. B*, 16:1422, 1979.

[106] P. Kruse, M. Hale, and A.C. Kummel. *J. Chem. Phys.*, 114:3215, 2000.

[107] J. Gou-Ping and H.E. Ruda. *J. Appl. Phys.*, 83:5880, 1998.

[108] F. Seker, K. Meeker, T.F. Kuech, and A.B. Ellis. *Chem. Rev.*, 100:2505, 2000.

[109] C. Joachim, J. K. Gimzewski, and A. Aviram. *Nature*, 408:541, 2000.

[110] L. Kronik and Y. Shapira. *Surf. Sci. Rep.*, 37:1, 1999.

[111] R. A. Wolkow. *Ann. Rev. Phys. Chem.*, 50:413, 1999.

[112] R. J. Hamers. *Nature*, 412:489, 2001.

[113] G. Ashkenasy, D. Cahen, R. Cohen, A. Shanzer, and A. Vilan. *Acc. Chem. Res.*, 35:121, 2002.

[114] A. Vilan and D. Cahen. *Trends in Biotech.*, 20:22, 2002.

[115] D. Cahen and G. Hodes. *Adv. Mater.*, 14:789, 2002.

[116] M. Bruening, R. Cohen, J.F. Guillemoles, T. Moav, J. Libman, A. Shanzer, and D. Cahen. *J. Am. Chem. Soc.*, 119:5720, 1997.

[117] Y. Selzer and D. Cahen. *Adv. Mater.*, 13:508, 2001.

[118] A. Vilan, A. Shanzer, and D. Cahen. *Nature*, 404:166, 2000.

[119] D. Guo Wu, J. Ghabboun, J.M.L. Martin, and D. Cahen. *J. Phys. Chem. B*, 105:12011, 2001.

[120] Dm. Shvarts, A. Haran, R. Benshafrut, D. Cahen, and R. Naaman. *Chem. Phys. Lett.*, 354:349, 2002.

[121] S. Lodha and D. B. Janes. *Appl. Phys. Lett.*, 85:2809, 2004.

[122] R. J. Hamers, S. K. Coulter, M. D. Ellison, J. S. Hovis, D. F. Padowitz, M. P. Schwartz, M. C. Greenlief, and Jr. Russell, J. N. *Acc. Chem. Res.*, 33:617, 2000.

[123] N.P. Guisinger, M.E. Greene, R. Basu, A.S. Baluch, and M.C. Hersam. *Nano Letters*, 4:55, 2004.

[124] O. Gershewitz, M. Grinstein, C. Sukenik, K. Regev, J. Ghabboun, and D. Cahen. *J. Phys. Chem. B*, 108:664, 2004.

[125] D.W. Guo, G. Ashkenasy, D. Shvarts, R. Ussyshkin, R. Naaman, Y. Selzer, and D. Cahen. *Angew. Chem., Int. Ed. Engl.*, 39:4496, 2000.

[126] Y. Selzer, A. Salomon, J. Ghabboun, and D. Cahen. *Angew. Chem., Int. Ed. Engl.*, 41:827, 2002.

[127] I.H. Campbell, J.D. Kress, R.L. Martin, D.L. Smith, N.N. Barashkov, and J.P. Ferraris. *Appl. Phys. Lett.*, 71:3528, 1997.

[128] L. Zuppiroli, L. Si-Ahmed, K. Kamaras, F. Nuesch, M.N. Bussac, D. Ades, A. Siove, E. Moons, and M. Gratzel. *Eur. Phys. J. B*, 11:505, 1999.

[129] I. Visoly-Fisher, A. Sitt, M. Wahab, and D. Cahen. *ChemPhysChem*, 6:277, 2005.

[130] J. Martz, L. Zuppiruli, and F. Nuesch. *Langmuir*, 20:11428, 2004.

[131] H. Haick, M. Ambrico, T. Ligonzo, and D. Cahen. *Adv. Mater.*, 16:2145, 2004.

[132] A. Vilan, J. Ghabboun, and D. Cahen. *J. Phys. Chem. B*, 107:6360, 2003.

[133] R. Cohen, L. Kronik, A. Vilan, A. Shanzer, and D. Cah en. *Adv. Mater.*, 12:33, 2000.

[134] M. Bruening, E. Moons, D. Yaron-Marcovich, D. Cahen, J. Libman, and A. Shanzer. *J. Am. Chem. Soc.*, 116:2972, 1994.

[135] R. Cohen, S. Bastide, D. Cahen, J. Libman, A. Shanzer, and Y. Rosenwaks. *Adv. Mater.*, 9:746, 1997.

[136] S. Bastide, R. Butruille, D. Cahen, A. Dutta, J. Libman, A. Shanzer, L. Sun, and A. Vilan. *J. Phys. Chem. B*, 101:2678, 1997.

[137] H. Haick, J. Ghabboun, and D. Cahen. *App. Phys. Lett.*, 86:42113, 2005.

[138] A. Vilan and D. Cahen. *Adv. Funct. Mater.*, 12:795, 2002.

[139] D. Cahen and A. Kahn. *Adv. Mater.*, 15:271, 2003.

[140] A. Vilan, R. Ussyshkin, K. Gartsman, D. Cahen, R. Naaman, and A. Shanzer. *J. Phys. Chem. B*, 102:3307, 1998.

[141] F.L. Hirshfeld. *Theor. Chim. Acta*, 44:129, 1977.

[142] R. F. W. Bader. *Atoms in Molecules, a Quantum Theory.* Clarenton Press: Oxford, U.K., 1990.

[143] U. Diebold. *Surface Science Reports*, 48:53, 2003.

[144] K.I. Hadjiivanov and D.G. Klissurski. *Chemical Society Reviews*, 25:61, 1996.

[145] A.L. Linsebigler, G. Q. Lu, and J.T. Yates. *Chemical Reviews*, 95:735, 1995.

[146] B. O'Regan and M.A. Gräetzel. *Nature*, 353:737, 1991.

[147] T. Rajh, Z. Saponjic, J. Q. Liu, N. M. Dimitrijevic, N. F. Scherer, M. Vega-Arroyo, P. Zapol, L. A. Curtiss, and M. C. Thurnauer. *Nano Letters*, 4:1017, 2004.

[148] P. C. Redfern, P. Zapol, L. A. Curtiss, T. Rajh, and M. C. Thurnauer. *Journal of Physical Chemistry B*, 107:11419, 2003.

[149] K. S. Kim and M. A. Barteau. *Langmuir*, 6:1485, 1990.

[150] K. S. Kim and M. A. Barteau. *Journal of Catalysis*, 125:353, 1990.

[151] C. Lai, Y. I. Kim, C. M. Wang, , and T. E. Mallouk. *J. Org. Chem.*, 58:1393, 1993.

[152] M. K. Nazeeruddin, S. M. Zakeeruddin, J. J. Lagref, P. Liska, P. Comte, C. Barolo, G. Viscardi, K. Schenk, and M. Graetzel. *Coordination Chemistry Reviews*, 248:1317, 2004.

[153] A. Sclafani, L. Palmisano, M. Schiavello, V. Augugliaro, S. Coluccia, and L. Marchese. *New J. Chem.*, 12:129, 1988.

[154] L. Palmisano, A. Sclafani, M. Schiavello, V. Augugliaro, S. Coluccia, , and L. Marchese. *New J. Chem.*, 12:137, 1988.

[155] L. Palmisano, M. Schiavello, A. Sclafani, S. Coluccia, and L. Marchese. *New J. Chem.*, 12:847, 1988.

[156] A. Assabane, Y. A. Ichou, H. Tahiri, C. Guillard, and J. M. Herrmann. *Applied Catalysis B-Environmental*, 24:71, 2000.

[157] J. M. Herrmann, H. Tahiri, C. Guillard, and P. Pichat. *Catalysis Today*, 54:131, 1999.

[158] H. Tahiri, Y. A. Ichou, and J. M. Herrmann. *Journal of Photochemistry and Photobiology A-Chemistry*, 114:219, 1998.

[159] J. M. Herrmann, J. Disdier, P. Pichat, S. Malato, and J. Blanco. *Applied Catalysis B-Environmental*, 17:15, 1998.

[160] J. C. Doliveira, W. D. W. Jayatilake, K. Tennakone, J. M. Herrmann, and P. Pichat. *Studies in Surface Science and Catalysis*, 75:2167, 1993.

[161] H. Uetsuka, M. A. Henderson, A. Sasahara, and H. Onishi. *Journal of Physical Chemistry B*, 108:13706, 2004.

[162] H. Onishi, T. Aruga, and Y. Iwasawa. *Journal of Catalysis*, 146:557, 1994.

[163] S. Thevuthasan, G. S. Herman, Y. J. Kim, S. A. Chambers, C. H. F. Peden, Z. Wang, R. X. Ynzunza, E. D. Tober, J. Morais, and C. S. Fadley. *Surface Science*, 401:261–268, 1998.

[164] S. A. Chambers, M. A. Henderson, Y. J. Kim, and S. Thevuthasan. *Surface Review and Letters*, 5:381–385, 1998.

[165] Q. Guo, I. Cocks, and E. M. Williams. *Surface Science*, 393:1–11, 1997.

[166] I. D. Cocks, Q. Guo, R. Patel, E. M. Williams, E. Roman, and J. L. De Segovia. *Surface Science*, 377:135–139, 1997.

[167] Q. Guo, I. Cocks, and E. M. Williams. *Journal of Chemical Physics*, 106:2924–2931, 1997.

[168] J. Ahdjoudj and C. Minot. *Catalysis Letters*, 46:83–91, 1997.

[169] F. P. Rotzinger, J. M. Kesselman-Truttmann, S. J. Hug, V. Shklover, and M. Gratzel. *Journal of Physical Chemistry B*, 108:5004–5017, 2004.

[170] R. E. Tanner, A. Sasahara, Y. Liang, E. I. Altman, and H. Onishi. *Journal of Physical Chemistry B*, 106:8211–8222, 2002.

[171] R. E. Tanner, Y. Liang, and E. I. Altman. *Surface Science*, 506:251–271, 2002.

[172] A. Vittadini, A. Selloni, F. P. Rotzinger, and M. Gratzel. *Journal of Physical Chemistry B*, 104:1300–1306, 2000.

[173] N. Ruzycki, G. S. Herman, L. A. Boatner, and U. Diebold. *Surface ScienceLetters*, 529:L239–L244, 2003.

[174] G. Spoto, C. Morterra, L. Marchese, L. Orio, and A. Zecchina. *Vacuum*, 41:37–39, 1990.

[175] G. Martra. *Applied Catalysis A-General*, 200:275–285, 2000.

[176] T. Bredow T. Homann and K. Jug. *Surface Science*, 555:135–144, 2004.

[177] L. F. Liao, C. F. Lien, and J. L. Lin. *Physical Chemistry Chemical Physics*, 3:3831–3837, 2001.

[178] M. Kotaka M. Kakihana and M. Okamoto. *J. Phys. Chem.*, 87:2526–2535, 1983.

[179] A. Hagfeldt and M. Gratzel. *Acc. Chem. Res.*, 33:269, 2000.

[180] Shklover V., Ovchinnikov Yu.E., Braginsky L.S., S.M. Zakeeruddin, and M. Grätzel. *Chem. Mater.*, 10:2533, 1998.

[181] M. K. Nazeeruddin, S. M. Zakeeruddin, R. Humphry-Baker, M. Jirousek, P. Liska, N. Vlachopoulos, V. Shklover, C.H. Fischer, and M. Graetzel. *Inorg. Chem.*, 38:6298, 1999.

[182] M. K. Nazeeruddin, R. Humphry-Baker, P. Liska, and M. Graetzel. *J. Phys. Chem. B*, 107:8981, 2003.

[183] M. Yanagida, L.P. Singh, K. Sayama, Hara K., R. Katoh, A. Islam, H. Sugihara, H. Arakawa, M.K. Nazeeruddin, and M. Grätzel. *J. Chem. Soc., Dalton Trans.*, page 2817, 2000.

[184] A. Vittadini, A. Selloni, F. P. Rotzinger, and M. Gratzel. *Phys. Rev. Lett.*, 81:2954, 1998.

[185] X-Q. Gong, A. Selloni, and A. Vittadini. *J. Phys. Chem. B*, 110:2804, 2006.

[186] L.G.C. Rego and V.S. Batista. *J. Am. Chem. Soc.*, 125:7989, 2003.

[187] P. Persson, A. Stashans, R. Bergstrom, and S. Lunell. *Int. J. Quan. Chem.*, 70:1055, 1998.

[188] M. Odelius, P. Persson, and S. Lunell. *Surf. Sci.*, 529:47, 2003.

[189] P. Persson and S. Lunell. *Solar Energy Materials Solar Cells*, 63:147, 2000.

[190] P. Persson, S. Lunell, and L. Ojamae. *Chem. Phys. Lett.*, 364:469, 2002.

[191] P. Persson, M.J. Lundqvist, R. Ermstorfer, W.A. Goddard, and F. Willig. *J. Chem. Theo. and Comp.*, 2:441, 2006.

[192] M. Haukka and P. Hirva. *Surf. Sci.*, 511:373, 2002.

[193] M.L. Sushko, A.Y. Gal, and A.L. Shluger. *J. Phys. Chem. B*, 110:4853, 2006.

[194] Hara K., Sugihara H., Tachibana Y., A. Islam, M. Yanagida, K. Sayama, and H. Arakawa. *Langmuir*, 17:5992, 2001.

[195] Fantacci S., De Angelis F., and Selloni A. *JACS*, 125:4381, 2003.

[196] Guillemoles J.F., Barone V., Joubert L., and Adamo C. *J. Phys. Chem. A*, 106:11354, 2002.

[197] Y. Liu, J.I. Dadap, D. Zimdars, and K.B. Eisenthal. *J. Phys. Chem. B*, 103:2480, 1999.

[198] A.Jr. Vlcek. *Coord. Chem. Rev.*, 933:200, 2000.

[199] K. R. Roth, A. A. Yasseri, Z. Liu, R. B. Dabke, V. Malinovskii, K. H. Schweikart, L. Yu, H. Tiznado, F. Zaera, J. S. Lindsey, W. G. Kuhr, and D. F. Bocian. *J. Am. Chem. Soc.*, 125:505, 2003.

[200] J. M. Buriak. *Chem. ReV.*, 102:1271, 2002.

[201] D. D. M. Wayner and R. A. Wolkow. *J. Chem. Soc., Perkin Trans.*, 2:23, 2002.

[202] S. F. Bent. *J. Phys. Chem. B*, 106:2830, 2002.

[203] C. E. D. Chidsey, C. R. Bertozzi, T. M. Putvinski, and A.M. Mujsce. *J. Am. Chem. Soc.*, 112:4301, 1990.

[204] C. E. D. Chidsey. *Science*, 251:919, 1991.

[205] J. F. Smalley, S. B. Sachs, C. E. D. Chidsey, S. P. Dudek, D. Sikes, H, S. E. Creager, C. J. Yu, S. W. Feldberg, and M. D. Newton. *J. Am. Chem. Soc.*, 126:14620, 2004.

[206] D. Sikes, H, J. F. Smalley, S. P. Dudek, A. R. Cook, M. D. Newton, C. E. D. Chidsey, and S. W. Feldberg. *Science*, 291:1519, 2001.

[207] S. B. Sachs, S. P. Dudek, R. P. Hsung, L. R. Sita, J. F. Smalley, M. D. Newton, S. W. Feldberg, and C. E. D. Chidsey. *J. Am. Chem. Soc.*, 119:10563, 1997.

[208] S. Creager, C. J. Yu, C. Bambad, S. OConnor, T. MacLean, E. Lam, Y. Chong, G. T. Olsen, J. Luo, M. Gozin, and J. F. Kayyem. *J. Am. Chem. Soc.*, 121:1059, 1999.

[209] E. A. Dalchiele, A. Aurora, G. Bernardini, F. Cattaruzza, A. Flamini, P. Pallavicini, R. Zanoni, and F. Decker. *J. Electroanal. Chem.*, 57:133, 2005.

[210] P. Kruse, E. R. Johnson, G. A. DiLabio, and R. A. Wolkow. *Nano Lett.*, 2:807, 2002.

[211] Q. Li, G. Mathur, S. Gowda, S. Surthi, Q. Zhao, L. Yu, J. S. Lindsey, D. F. Bocian, and V. Misra. *AdV. Mater.*, 16:133, 2004.

[212] A. Balakumar, A. B. Lysenko, C. Carcel, V. L. Malinovskii, D. T. Gryko, K. H. Schweikart, L. S. Loewe, A. A. Yasseri, Z. Liu, D. F. Bocian, and J. S. Lindsey. *J. Org. Chem.*, 69:1435, 2004.

[213] Q. Li, G. Mathur, M. Homsi, S. Surthi, V. Misra, V. Malinovskii, K.-H. Schweikart, L. Yu, J. S. Lindsey, Z. Liu, R. B. Dabke, A. Yasseri, D. F. Bocian, and W. G. Kuhr. *Appl. Phys. Lett.*, 81:1494, 2002.

[214] B. Fabre and F. Hauquier. *J. Phys. Chem. B*, 110:6848, 2006.

[215] J. M. Buriak. *Chem. Commun.*, 99:1051, 1999.

[216] M. P. Stewart and J. M. Buriak. *J. Am. Chem. Soc.*, 123:7821, 2001.

[217] J. M. Schmeltzer, L. A. Porter, M. P. Stewart, and J. M. Buriak. *Langmuir*, 18:2971, 2002.

[218] Q.-Y. Sun, Louis, C. P. M. de Smet, B. van Lagen, A. Wright, H. Zuilhof, and E. J. R. Sudhoelter. *Angew. Chem., Int. Ed.*, 43:1352, 2004.

[219] W. Klopper and H.P. Lüthi. *Chem. Phys. Lett.*, 262:546, 1996.

[220] A. Haaland. *Top. Curr. Chem.*, 53:1, 1975.

[221] H. Koch, P. Jorgensen, and T. Helgaker. *J. Chem. Phys.*, 23:9528, 1996.

[222] P. Winget, E. J. Weber, C. J. Cramer, and D. G. Truhlar. *Phys. Chem. Chem. Phys.*, page 1931, 2000.

[223] Y. Fu, L. Liu, H.-Z. Yu, Y.M. Wang, and Q.X. Guo. *J. Am. Chem. Soc.*, 127:7227, 2005.

[224] H. Reiss and A. Heller. *J. Chem. Phys.*, 89:4207, 1985.

[225] M. Cossi, M.F. Iozzi, A.G. Marrani, T. Lavecchia, P. Galloni, R. Zanoni, and F. Decker. *J. Phys. Chem. B*, 110:22961, 2006.

[226] T.A. Wesolowsky and A. Warshel. *J. Phys. Chem.*, 97:8050, 1993.

[227] M.E. Casida and T.A. Wesolowsky. *Int. J. Quan. Chem.*, 96:577, 2002.